ESTIMATION OF OCEANIC RAINFALL USING PASSIVE AND ACTIVE MEASUREMENTS FROM SEAWINDS SPACEBORNE MICROWAVE SENSOR

by

KHALIL ALI AHMAD

M.S. University of Central Florida, 2004

A dissertation submitted in partial fulfillment of the requirements
for the degree of Doctor of Philosophy
in the School of Electrical Engineering and Computer Science
in the College of Engineering and Computer Science
at the University of Central Florida
Orlando, Florida

Fall Term
2007

Major Professor: W. Linwood Jones

ABSTRACT

The Ku band microwave remote sensor, SeaWinds, was developed at the National Aeronautics and Space Administration (NASA) Jet Propulsion Laboratory (JPL). Two identical SeaWinds instruments were launched into space. The first was flown onboard NASA QuikSCAT satellite which has been orbiting the Earth since June 1999, and the second instrument flew onboard the Japanese Advanced Earth Observing Satellite II (ADEOS-II) from December 2002 till October 2003 when an irrecoverable solar panel failure caused a premature end to the ADEOS-II satellite mission. SeaWinds operates at a frequency of 13.4 GHz, and was originally designed to measure the speed and direction of the ocean surface wind vector by relating the normalized radar backscatter measurements to the near surface wind vector through a geophysical model function (GMF). In addition to the backscatter measurement capability, SeaWinds simultaneously measures the polarized radiometric emission from the surface and atmosphere, utilizing a ground signal processing algorithm known as the QuikSCAT / SeaWinds Radiometer (QRad / SRad). This dissertation presents the development and validation of a mathematical inversion algorithm that combines the simultaneous active radar backscatter and the passive microwave brightness temperatures observed by the SeaWinds sensor to retrieve the oceanic rainfall. The retrieval algorithm is statistically based, and has been developed using collocated measurements from SeaWinds, the Tropical Rainfall Measuring Mission (TRMM) Microwave Imager (TMI) rain rates, and Numerical Weather Prediction (NWP) wind fields from the National Centers for Environmental Prediction (NCEP). The oceanic rain is retrieved on a spacecraft wind

vector cell (WVC) measurement grid that has a spatial resolution of 25 km. To evaluate the accuracy of the retrievals, examples of the passive-only, as well as the combined active / passive rain estimates from SeaWinds are presented, and comparisons are made with the standard TRMM rain data products. Results demonstrate that SeaWinds rain measurements are in good agreement with the independent microwave rain observations obtained from TMI. Further, by applying a threshold on the retrieved rain rates, SeaWinds rain estimates can be utilized as a rain flag. In order to evaluate the performance of the SeaWinds flag, comparisons are made with the Impact based Multidimensional Histogram (IMUDH) rain flag developed by JPL. Results emphasize the powerful rain detection capabilities of the SeaWinds retrieval algorithm. Due to its broad swath coverage, SeaWinds affords additional independent sampling of the oceanic rainfall, which may contribute to the future NASA's Precipitation Measurement Mission (PMM) objectives of improving the global sampling of oceanic rain within 3 hour windows. Also, since SeaWinds is the only sensor onboard QuikSCAT, the SeaWinds rain estimates can be used to improve the flagging of rain-contaminated oceanic wind vector retrievals. The passive-only rainfall retrieval algorithm (QRad / SRad) has been implemented by JPL as part of the level 2B (L2B) science data product, and can be obtained from the Physical Oceanography Distributed Data Archive (PO.DAAC).

Dedication page

I'll fill out later

ACKNOWLEDGMENTS

I'll fill out later

Orlando, FL

September 30, 2007

TABLE OF CONTENTS

LIST OF FIGURES

LIST OF TABLES

LIST OF ACRONYMS/ABBREVIATIONS

ADEOS	Advanced Earth Observing Satellite
AMI	Active Microwave Instrument
AMSR	Advanced Microwave Scanning Radiometer
CMIS	Conical Scanning Microwave Imager/Sounder
DMSP	Defense Meteorological Satellite Program
ERS	European Remote sensing Satellite
ESA	European Space Agency
GMF	Geophysical Model Function
GPM	Global Precipitation Mission
JAXA	Japan Aerospace Exploration Agency
JPL	Jet Propulsion Laboratory
LEO	Low Earth Orbit
NASA	National Aeronautics and Space Administration
NASDA	National Space Development Agency (Japan)
NCEP	National Center for Environmental Prediction
NESDIS	National Environmental Satellite, Data, and Information Service
NRCS	Normalized Radar Cross Section
NRL	Naval Research Laboratory
NSCAT	NASA Scatterometer
QuikSCAT	Quick Scatterometer
SASS	Seasat-A Satellite Scatterometer

SSM/I	Special Sensor Microwave/Imager
SST	Sea Surface Temperature
TRMM	Tropical Rainfall Measuring Mission
TMI	TRMM Microwave Imager
WVC	Wind Vector Cell

CHAPTER ONE: INTRODUCTION

Rainfall is an essential source of fresh water that sustains all forms of life. It plays a significant role in the Earth's hydrological circulation, where vast quantities of water cycle through the Earth's atmosphere, oceans, and land over both short and long time scales. Rainfall keeps the Earth in balance by redistributing water from the oceans and warm tropical areas to the rest of the planet. The condensation of water vapor into rain in the Earth's atmosphere releases heat. This heat is the drive of the Earth's wind systems which move clouds, power tropical storms and violent hurricanes.

During recent years, significant progress has been witnessed in weather forecasting, climate monitoring and extreme event prediction using sophisticated numerical models. These models are fed among other inputs, with rainfall data. Accuracy of these weather prediction models depends on availability of frequent, uniformly sampled rainfall measurements with global coverage. Therefore, an accurate knowledge of the intensity, distribution and variability of rainfall on a global basis is of paramount importance to help scientists and researchers better understand the water and energy cycles, and accurately predict weather and climate patterns.

Over the land, rain measurements are generally available using networks of rain gauges and ground based meteorological radars. On the other hand, rain estimation over the open oceans suffers from a scarcity of in-situ measurements, which is mainly attributed to the rough marine environment and high cost associated with the deployment of in situ observation systems. Since oceans cover about 70% of the Earth surface,

contain nearly 97% of the Earth free water, and because the vast majority of global rainfall and evaporation occurs over the oceans, solving the problem of observational shortage in measuring the rainfall over oceans has received significant attention. Over the past three decades, space-borne remote sensing techniques utilizing specialized sensors, operating at microwave frequencies, and flying onboard artificial satellites in low Earth orbits (LEO) have proven to be efficient in providing unparalleled wide coverage and frequent measurements of oceanic rainfall.

In addition to providing useful rainfall information, satellite microwave sensors have been applied and successfully utilized in monitoring various atmospheric and oceanic environmental parameters. For example, space-borne scatterometers have been used in vegetation and soil moisture mapping, discrimination of ice types, and measuring the global ocean wind speed and direction [1-3]. Further, space-borne multi-frequency microwave radiometer imagers flying on low earth satellites, such as the Special Sensor Microwave/Imagers (SSM/I) series operated on the Defense Meteorological Satellite Program (DMSP), and the Tropical Rainfall Measuring Mission (TRMM) Microwave Imager (TMI) have provided reliable passive microwave data for retrieving various atmospheric and oceanic environmental parameters such as integrated atmospheric water vapor and cloud liquid water, ocean surface wind speed, and sea ice concentration and type [3-5].

One of the most recent microwave sensors developed by NASA is the SeaWinds instrument. SeaWinds is a conical scanning sensor, which operates at a Ku-band frequency of 13.4 GHz. The instrument utilizes a mechanically spun parabolic antenna with a dual polarized pencil beam design to collect measurements over a continuous

swath that covers about 90% of the Earth's surface on a daily basis. A typical global coverage of the instrument during a 24 hour period is presented in Figure 1 below. The SeaWinds instrument was launched onboard two satellite missions: the first was onboard NASA's QuikSCAT satellite which has been in orbit since June 1999. A second identical instrument flew onboard Japan's Advanced Earth Observing Satellite II (ADEOS II) between December 2002 and October 2003, when a malfunction of power generating solar panels caused a premature termination of the ADEOS II satellite mission.

.

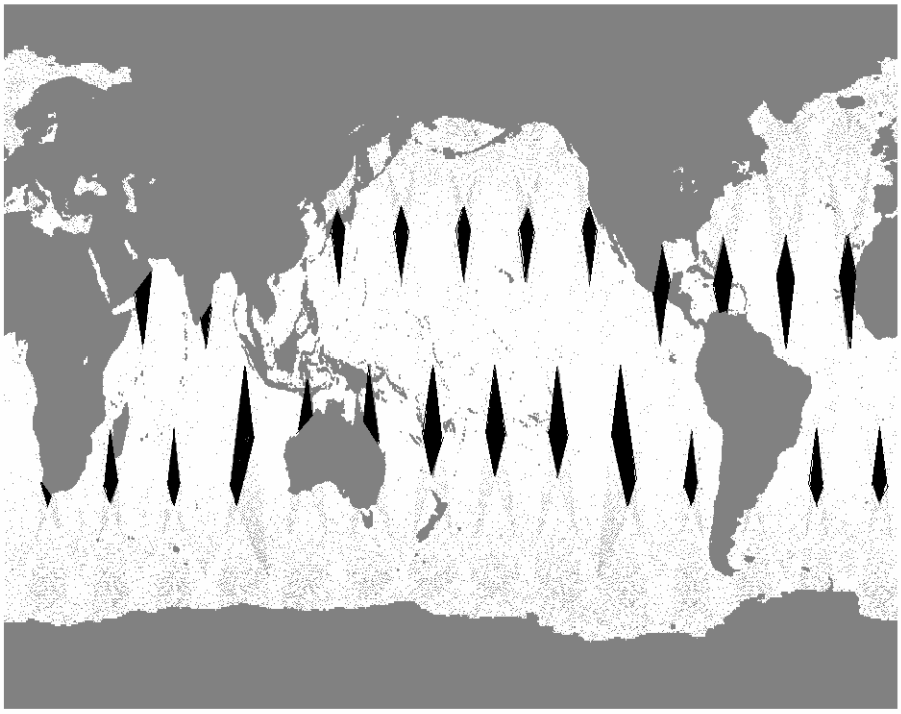

Figure 1: Typical daily coverage of the SeaWinds instrument. Black indicates uncovered oceanic areas.

The primary mission objective of the SeaWinds instrument was to measure the speed and direction of the global ocean wind vector, by measuring the wind dependant normalized radar cross section (σ^0) of the ocean's surface. To obtain the σ^0 measurements, SeaWinds transmits microwave pulses of known power and duration to the surface, and measures the portion of power backscattered toward the antenna through a narrow band 250 KHz echo channel. Because the power measurement is corrupted with noise, SeaWinds utilizes an additional noise channel with a 1 MHz bandwidth to make a separate measurement of the noise-only power, which is subtracted from the signal + noise measured by the echo channel. This provides the measurement of the backscattered power, from which σ^0 measurements can be estimated using the radar equation [2].

In addition to measuring the active normalized radar backscatter, the SeaWinds instrument has the simultaneous capability to measure the linearly polarized passive radiometric emission from the Earth's surface and intervening atmosphere. This capability, known as the QuikSCAT Radiometer (QRad) is made possible by calibrating SeaWinds noise channel to provide measurements of polarized brightness temperatures at 13.4 GHz. The QRad radiometric transfer function was not originally envisioned, rather it was implemented post launch through ground signal processing [6].

Validation studies demonstrate that the SeaWinds instrument is capable of providing highly accurate estimates of the global oceanic wind vector under most rain free weather conditions [7]. However, the presence of rain can alter the wind induced backscatter signature and even corrupt the wind estimation process. While rain can only affect up to ~10% of the SeaWinds measurements on an average basis, the spatial and temporal distribution of rain is not random. The degradation of the retrieved wind vector

accuracy obtained from SeaWinds is manifested as a positive wind speed bias, and an erroneous wind direction solution which is usually pointing perpendicular to the spacecraft nadir track. Thus, in order to maintain the high quality of the wind measurements retrieved from the SeaWinds instrument, it is of primary importance to detect the presence of rain and identify the contaminated wind vector measurements.

In this dissertation, we utilize the SeaWinds simultaneous passive radiometric brightness temperatures, and active radar backscatter measurement capabilities to develop a mathematical inversion algorithm that detects the presence of rain, and further provides quantitative estimates of the global oceanic rainfall. The algorithm is based upon a correlation between the passive / active measurements from SeaWinds and the rain rates derived from TRMM TMI radiometer. Using a statistical inversion technique, oceanic rain rates are retrieved from SeaWinds data on a spacecraft wind vector cell (WVC) measurement grid of 25 km resolution. To evaluate the performance of the SeaWinds retrieval algorithm, comparisons are made with standard rain products from independent rain measuring instruments. Results demonstrate that SeaWinds rain estimates correlate well with those independent rain measurements. Besides providing a powerful rain flag that identifies the rain contaminated wind vector measurements, SeaWinds rain estimates have the additional scientific utility of improving the temporal and spatial coverage of the sparsely sampled oceanic rainfall.

This dissertation is organized into eight chapters. Following this introduction, chapter two summarizes the basic principles of microwave scatterometry and radiometry. The chapter also includes a brief history of various satellite scatterometer and radiometer missions. Further, a detailed discussion of the SeaWinds instrument is given. Chapter

three presents a brief literature review of the techniques used to retrieve oceanic rainfall from space-borne active and passive observations. Theoretical background, of the interaction between rain and electromagnetic radiation, is also presented. Chapters four – seven are the core of this dissertation. In chapter four, a detailed discussion of the development of the passive-only QuikSCAT Radiometer (QRad) rain algorithm is presented. The QRad algorithm utilizes the passive radiometric measurements from SeaWinds to detect and estimate oceanic rainfall. Validation of QRad rain retrievals are presented in chapter five. Chapter six discusses the development of a simple empirical model that characterizes the average effect of rain on the SeaWinds backscatter measurements. In chapter seven, a combined passive / active rain retrieval algorithm is developed to refine the oceanic rain estimation from SeaWinds sensor. The dissertation concludes with a brief summary and conclusions in chapter eight.

CHAPTER TWO: REVIEW OF MICROWAVE SCATTEROMETRY AND RADIOMETRY

Introduction

For more than three decades, space-borne microwave sensors have proven to be indispensable tools in providing useful information on various environmental parameters related to the Earth's surface and atmosphere [2, 3, 5]. These space-borne sensors can provide more frequent mapping and uniform sampling than what is available from the conventional in situ observations. Further, operation at microwave frequencies enables measurements to be acquired under almost all weather, day / night conditions.

According to their mode of operation, microwave sensors can be divided into two major categories. The first is the group of sensors capable of providing their own source of illumination, known as active sensors. They consist of a transmitter and a receiver. This group of sensors includes radars, scatterometers, and altimeters. The second group of microwave sensors is the passive sensors, also known as microwave radiometers. They consist of highly sensitive receivers that measure the electromagnetic radiation originating from the scene observed by the sensor antenna. Data from both active and passive sensors has been effectively used in a variety of Earth science studies, including mapping the rainfall over the ocean.

The SeaWinds microwave sensor considered in this dissertation has the unique capability to operate simultaneously as a scatterometer and a radiometer at a Ku-band

frequency of 13.4 GHz. In order to understand the underlying principles of operation of the SeaWinds instrument, this chapter presents a brief background on the fundamental concepts of microwave radiometry and scatterometry. A brief historical overview of previous and current satellite radiometer and scatterometer missions is given. In the last section, a detailed discussion of the SeaWinds instrument, including its measurement geometry and radiometric transfer function is provided.

Fundamental Concepts of Microwave Scatterometry

When an electromagnetic (EM) wave strikes the boundary surface separating two semi-infinite media, part of the incident energy is scattered, and the rest propagates through the second medium. Depending on the dielectric homogeneity of the second medium, two scattering mechanisms can take place [2]:

If the second medium is homogeneous, the scattering process is limited to the boundary surface, resulting in surface scattering phenomena. The surface scattering is dependant upon the roughness of the surface, a relative property determined by the wavelength of the incident EM wave. According to the degree of roughness, three surface scattering patterns can be observed, as illustrated in Figure 2. For a smooth surface, reflection at the surface is mainly a specular reflection, described by Fresnel laws. For a medium rough surface, the scattering consists of two components, a coherent component in the specular direction, and a non coherent (diffuse) component which radiates power in

all directions. As the roughness of the surface increase, the coherent component becomes negligible, while the diffuse scattering component becomes more dominant, as the case of a very rough (Lambertian) surface.

On the other hand, if the second medium is dielectrically inhomogeneous, or composed of a mixture of materials with different dielectric properties, the scattering process takes place within the volume of the second medium, which is referred to as volume scattering. The mechanism of volume scattering redistributes the transmitted wave energy into other directions and results in a loss, compared to the energy of the original transmitted wave.

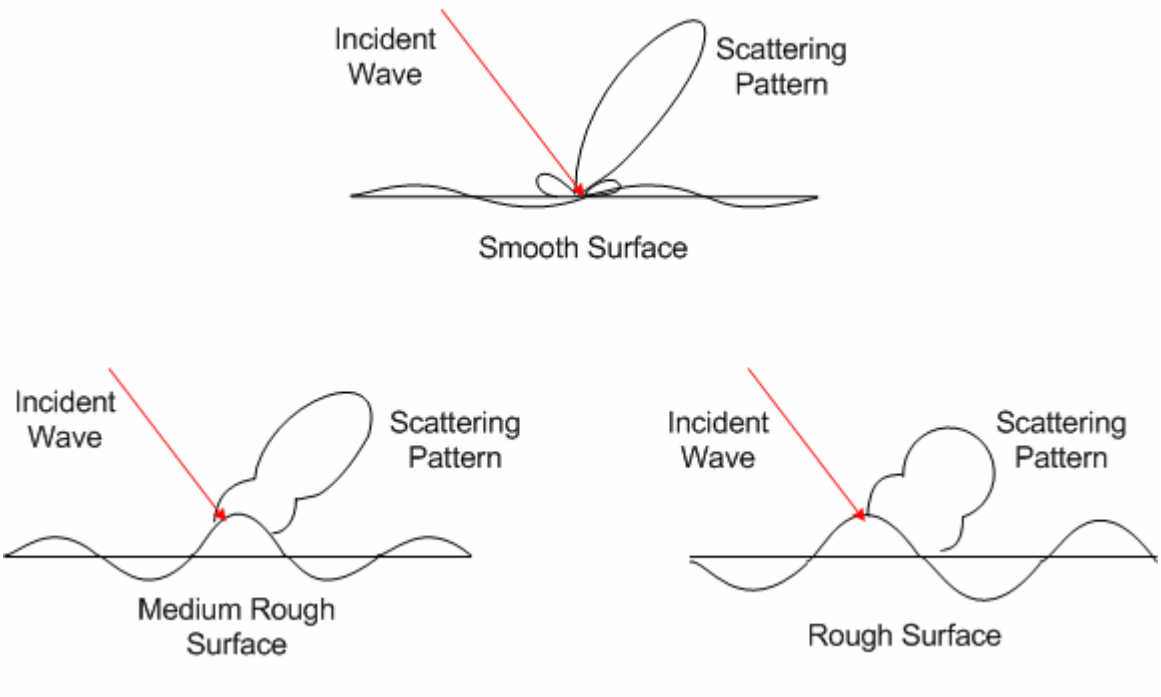

Figure 2: Examples of surface scattering patterns.

In the microwave region, ocean has a large dielectric constant and is treated as a homogeneous medium primarily capable of surface scattering. Radar backscattering from the ocean for angles of incidence beyond 20º is mainly governed by Bragg scattering. This scattering mechanism, usually described by the term Bragg resonance, appears to arise mainly from resonant interaction of incident EM radiation with periodic capillary and short gravity waves of the ocean surface. This phenomenon is illustrated in Figure 3, which shows a periodic component of the ocean surface wave, having a spatial wavelength of L. Also shown on the figure a plan EM wave of wavelength λ, which is incident upon the ocean surface at an angle of θ. At resonance, the displacement ΔR is equal to λ/2, and the phase components of the scattered EM field from successive wave crests will be multiples of 2π, and hence, will add constructively.

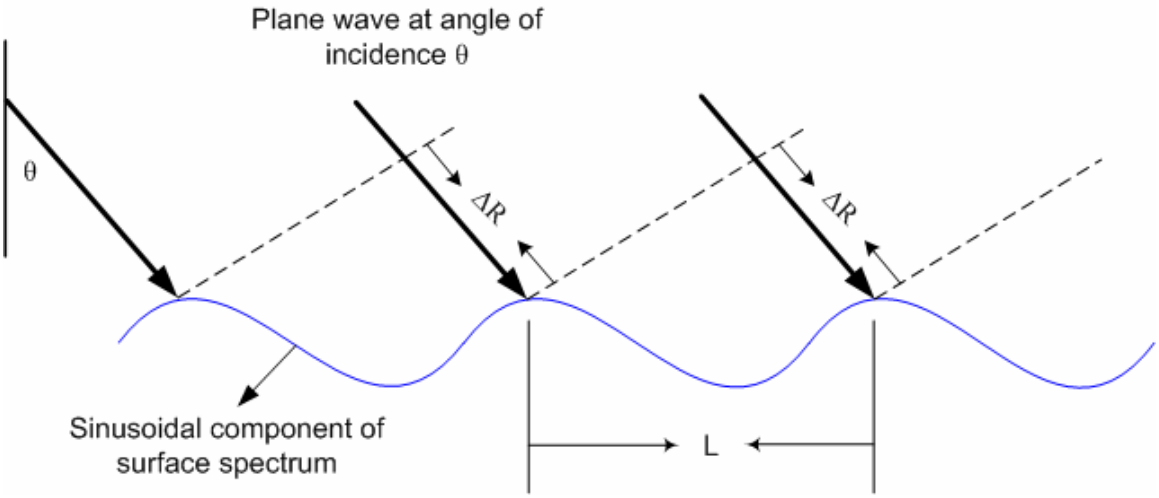

Figure 3: Illustration of in-phase addition of Bragg scattering when ΔR = nλ/2

The Bragg resonance condition can be mathematically described by [2]:

$$k\Delta R = \frac{2\pi}{\lambda}\Delta R = n\pi, \qquad n = 1,2,3,\ldots \tag{2.1}$$

where k is the EM wave number, equal to $2\pi/\lambda$. In terms of incidence angle and radar wavelength, the condition for Bragg resonance can be re-written as:

$$\frac{2L}{\lambda}\sin\theta = n, \qquad n = 1,2,3,\ldots \tag{2.2}$$

The power received from the resonant components is proportional to the square of their number. As the illuminated area increases, the number of resonant scatterers increases, and as a result, more resonant power is received. In the case of space-borne radars, with large footprints, the Bragg resonance effect is very powerful that it can dominate the return signal.

Radars are active remote sensors used to detect the presence, tack the position, or image an observed target. Because they are capable of providing their source of illumination, radars can usually operate under all weather and light independent conditions. Radars can transmit continuous waves or pulses of microwave energy, which upon interaction with the target, will be partially absorbed and partially scattered in all directions. The power back scattered toward the radar is collected by the antenna, and can be related to the transmitted power through the radar equation [8]:

$$P_r = \frac{P_t G_t G_r \lambda^2}{(4\pi)^3 R^4 L} \sigma \tag{2.3}$$

where P_t is the transmitted power in Watts, which is directionally modulated by the transmitting antenna gain G_t. R is the slant range distance to the target, measured in meters. λ is the wavelength of the transmitted radar signal in meters. P_r is received power in Watts, backscattered from the target, and captured by the receiving antenna with gain G_r. For a mono static radar (transmitter and receiver are on the same platform), the gains of the transmitting and receiving antennas are equal. L represents the system and propagation losses encountered during the round trip of the radar signal. The proportionality constant, σ, is the radar cross section measured in squared meters (m^2).

Equation 2.3 is the fundamental radar equation for point targets, whose dimensions are negligible compared to the radar antenna field of view (FOV). In remote sensing applications, targets of interest are usually extended area targets, such as the Earth's ocean or land surfaces. In such applications, the radar return consists of coherent contributions from a large number of point scatterers within the radar's antenna FOV, and as a result, σ is no longer considered a constant. An extended (distributed) target is divided into smaller sub-targets, each of area ΔA_i that contains enough number of point scatterers. The normalized radar cross section, σ^0, is a dimensionless quantity (m^2/ m^2), defined as the average value of the differential σ_i normalized to its area:

$$\sigma^0 = \left\langle \frac{\sigma_i}{\Delta A_i} \right\rangle \tag{2.4}$$

Using this definition of σ^0, equation (2.3) can be expanded to calculate the radar return from a distributed target by integrating the contributions from the differential elements over the area illuminated by the radar antenna:

$$P_r = \int_{\substack{illu\min ated \\ area(A)}} \frac{P_t G_t G_r \lambda^2}{(4\pi)^3 R^4 L} \sigma^0 dA \tag{2.5}$$

The normalized radar cross section, σ^0, is affected by instrument related factors, such as, wavelength, polarization, incidence and azimuth angles. Also, σ^0 is a function of the geometric and dielectric properties of the target, such as, roughness, size, slope, homogeneity, complex permittivity and permeability of the target's material, and it is considered as a unique and accurate signature of the target under observation. The sensitivity of σ^0 measurements to target parameters enables the remote sensing of various geophysical variables over land or ocean surfaces.

A scatterometer is a microwave radar calibrated to make accurate measurements of σ^0. The direct measurement is the received power from the area lit by the antenna. From the power measurement, σ^0 can be estimated by inverting Equation 2.5 [2]:

$$\sigma^0 = \frac{(4\pi)^3 R^4 L}{P_t G^2 \lambda^2 A} P_r \tag{2.6}$$

The primary application of the scatterometer σ^0 measurements is the retrieval of the near surface ocean wind vector (speed and direction), which is made possible due to the existence of a relationship between the σ^0 measurements and the wind roughened ocean surface. Scattering from the surface of the ocean is driven by several factors, among which is the roughness of the ocean surface that is determined by the wind induced waves. As the wind blows over the ocean surface, energy is transferred to the surface, and waves are generated and amplified. The first waves generated are known as the capillary (surface tension) waves. These waves travel in the direction of the wind, usually riding on larger ocean waves. According to Bragg scattering phenomenon, the tiny capillary waves resonate with the radar signal, and scattering from the ocean surface becomes highly dependent on the amplitude of these waves. As the wind speed increases, more energy is transferred to the waves, leading to an increase in their amplitudes, and eventually to more backscattered energy. Also, σ^0 measurements over the ocean surface exhibit an azimuthal modulation with respect to the relative wind direction blowing over the surface. In addition to the wind vector (speed and direction) dependence, σ^0 varies as a function of incidence angle, and the polarization of the incident EM wave, and can be affected by several geophysical parameters such as the sea surface temperature (SST), and foam coverage [2, 3].

Therefore, developing an analytical model to describe the ocean σ^0 is a complicated task due to the large number of factors and geophysical variables involved in the process. This led researchers to embark on empirical relations, known as geophysical model functions (GMFs), to define the dependence of ocean σ^0 measurements on certain parameters of interest. For example, since 1960s considerable amount of research has

been conducted to define accurate GMF relationships correlating the scatterometer σ^0 measurements to the near surface wind vector (speed and direction) over the ocean. These empirical GMFs utilized a large data set of near simultaneous airborne and spaceborne scatterometer σ^0 observations, co-registered with surface truth winds. The σ^0 measurements are binned according to the wind speed, relative wind direction, incidence and azimuth angles to empirically derive GMF relations, which are stored in multidimensional look-up tables. Some research has been conducted to employ neural networks to derive the GMF [9]. The dependence of σ^0 measurements on the wind vector through the GMF is denoted by:

$$\sigma^0 = \mathfrak{M}(\upsilon, \chi, \theta, p, \ldots) \tag{2.7}$$

Here, $\mathfrak{M}$ represents the GMF, υ is the wind speed, θ is the incidence angle, p is the polarization of the EM wave, χ is the relative direction defined as:

$$\chi = \alpha - \varphi \tag{2.8}$$

where α is the azimuth angle, and φ is wind direction. The dots (…) in Equation 2.7 denote the dependence of the GMF on other geophysical variables (sea surface temperature, foam coverage, etc.) whose contribution is considered negligible. An example of a GMF is depicted in Figure 4, which shows the loci of the ocean σ^0 plotted against the relative wind direction for three different wind speeds (3, 7 and 20 m/s). The

measurements are for a horizontally polarized beam, having an incidence angle of θ = 46º. The dependence of σ^0 on the wind speed is evident, moreover, an angular modulation of σ^0 as a function of the relative wind direction is clearly shown, where the upwind signal is stronger than the downwind, and both are much stronger than crosswind. This dependence of σ^0 on the speed and direction makes the retrieval of the ocean wind vector possible. The harmonic nature of the GMF can result in multiple pairs of speed and direction that corresponds to the same σ^0 value, therefore, multiple σ^0 measurements from different azimuth look angles are required to eliminate the ambiguity and find a unique wind vector solution [10].

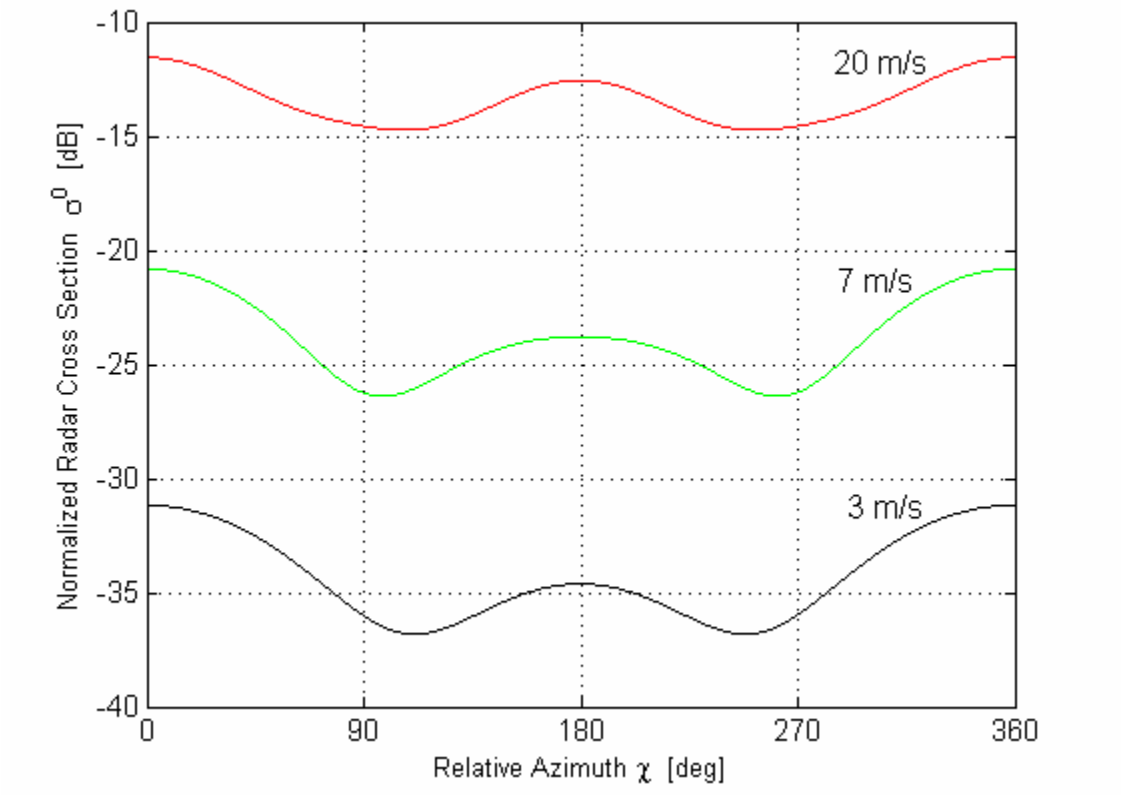

Figure 4: QuikSCAT Geophysical Model Function (GMF).

Satellite Scatterometer Missions

Historically, first measurements of ocean backscatter date to World War II, where it was observed that the presence of winds and waves increased the clutter intensity over the ocean surface [11]. The idea of using space-borne radars to study oceans first appeared in mid-1960s, and is attributed to Moore and Pierson. In early 1970s the concept that the measured backscatter was proportional to wind speed was widely accepted after extensive field experiments and theoretical developments, and as a result space-borne scatterometers were born.

The first space-borne scatterometer SL-193 flew as part of the Skylab mission during 1973 and 1974. The instrument operated at a frequency of 13.9 GHz, and utilized a dual linearly polarized parabolic antenna. The beam was scanned in fixed angles from vertical in the along track and cross track directions, producing single azimuth look measurements of the radar cross section. Although the single look measurement was insufficient to resolve the wind direction ambiguity, the Skylab mission demonstrated the feasibility to measure the ocean surface winds from space. During the early 1970s period, several airborne experiments took place. The most notable was NASA Advanced Applications Flight Experiment (AAFE) which was used in part to validate the performance of the Skylab instrument by under flights in the Gulf of Mexico. In addition to providing high quality ocean backscatter measurements, which formed the basis for the geophysical model function used with future scatterometer missions, the AAFE

measurements significantly contributed in determining the azimuth variations of σ^0 by using the innovative idea of circle flights [11].

The following space mission was the Seasat-A Satellite Scatterometer (SASS) operated for 99 days from June to October 1978 [1]. SASS was the first scatterometer designed specifically to measure the wind vectors on the ocean surface. Because each surface area was only viewed from two directions, it was insufficient to unambiguously retrieve the wind direction. However, the SASS cross section measurements have been used to significantly refine the empirical model relating backscatter to wind velocity, and this mission did prove that accurate wind velocity measurements could be made from space.

The next scatterometer in space was part of the Active Microwave Instrument (AMI) on the European Space Agency's first European Remote Sensing Satellite ERS-1 in 1991. This C-band 5.3 GHz system could measure each ocean location from three directions, thereby improving the ambiguity removal process. It was followed in 1995 by ERS-2 with an identical instrument [12, 13].

In 1996, the NASA scatterometer (NSCAT) instrument was launched as an experiment on Japan's Advanced Earth-Observation Satellite (ADEOS). NSCAT provided Ku-band backscatter and wind data for about 10 months till the demise of the host spacecraft in June 1997. In order to fill the gap created by the unexpected early loss of NSCAT scatterometer, NASA developed a quick recovery mission known as QuikSCAT satellite which has been in operation since June 1999 and houses the SeaWinds scatterometer. After about seven years in orbit, SeaWinds onboard QuikSCAT continues to provide high quality backscatter data that is being used in many scientific

applications. A second identical SeaWinds instrument flew onboard the Japanese Advanced Earth-Observation Satellite II (ADEOS-II) satellite which was launched in December 2002, but unfortunately the instrument was lost after ten months due to an irrecoverable failure in the spacecraft solar panel.

Unlike SASS and NSCAT scatterometers which both utilized the fan beam design, that uses multiple fixed position, sticklike antennas with broad beams to form the measurement swath, the SeaWinds instrument employs a pencil beam design which has several inherent advantages over the fan beam approach including higher signal-to-noise ratio, smaller size, simplicity, greater accuracy, extensive coverage, and easier accommodation on spacecraft. In addition to providing backscatter measurements, SeaWinds has the simultaneous capability of measuring the passive emission from the scene under observation. A detailed discussion of SeaWinds instrument is provided in the last section of this chapter.

Fundamental Concepts of Microwave Radiometry

Radiometry is field of science related to the measurement of incoherent electromagnetic radiation. A microwave radiometer is a passive, receive only sensor that is capable of measuring low levels of radiation in the microwave region of the electromagnetic spectrum. The received radiation is partly due to self emission by the scene, and partly due to reflection of radiation from the surroundings which is collected

by the antenna. Microwave radiometers have been extensively used in astronomical studies, as well as various studies related to the Earth's land, ocean and atmosphere [3, 5]. Data collected by microwave radiometers is being operationally used in weather forecasting and environmental monitoring [14].

Based upon thermodynamic principles, all material media (gases, liquids, solids and plasma) at a finite absolute temperature both emit and absorb incoherent electromagnetic energy. When in thermodynamic equilibrium with its environment, a material absorbs and radiates energy at the same rate. A blackbody is a fundamental concept in thermal emission, which is defined as a perfect absorber and a perfect emitter. According to Planck's radiation law, a blackbody radiates uniformly in all directions with a spectral brightness, B_f, defined by the following equation [5]:

$$B_f = \frac{2hf^3}{c^2}\left(\frac{1}{e^{hf/kT} - 1}\right) \tag{2.9}$$

where: h is Plank's constant (6.63 x 10^{-34} joules), k is Boltzmann's constant (1.38 x 10^{-23} joules K^{-1}), c is the velocity of light (3 x 10^8 m s^{-1}), T is the absolute temperature in Kelvin, f is the frequency of radiation. In the microwave region, Plank's law can be approximated by the Rayleigh-Jeans law given by:

$$B_f = \frac{2kT}{\lambda^2} \tag{2.10}$$

Using the above approximation, the blackbody power detected by a microwave radiometer receiver having a bandwidth Δf is given by:

$$P_{bb} = kT\Delta f \tag{2.11}$$

However, nothing in nature behaves like an ideal blackbody. Real materials, usually referred to as grey bodies, emit less than a blackbody does and do not absorb all the energy incident upon them. In this case, the blackbody equivalent radiometric temperature is called the brightness temperature, T_B, which is related to the physical temperature through emissivity, ε, as:

$$T_B = \varepsilon T \tag{2.12}$$

The emissivity is a function of frequency, polarization and incidence angle, and varies between zero for a perfectly non-emitting material and unity for a perfect emitter (blackbody). Thus, the brightness temperature of the material is always smaller than or equal to its physical temperature.

The Earth's atmosphere and ocean surface are examples of grey bodies that partially absorb and emit electromagnetic radiation. The emissivity of the ocean depends upon several geophysical variables, such as the ocean roughness, salinity, and the ocean surface temperature. Also, ocean emissivity varies with water complex dielectric constant, the presence of foam over the ocean surface, and it is strongly dependent on electromagnetic polarization. On the other hand, the emission from the atmosphere is

dependent upon absorption by oxygen, water vapor and liquid water particles. The atmospheric emission is independent of polarization. In the presence of rain, scattering effects may not be negligible depending on the density and drop size distribution of the water droplets relative to the electromagnetic wave.

Space-borne microwave radiometers are used to collect the brightness temperatures originating from the atmosphere and the ocean surface. A typical scenario is depicted in Figure 5. The total brightness incident upon the radiometer antenna is composed of the following three components: self-emission from the atmosphere which has propagated directly upward, T_{up}. The second component is the emission from the ocean surface that propagated upward through a partially absorptive atmosphere, T_{BS}. The third component is the downward self-emitted radiation from the atmosphere that is reflected by the ocean surface and propagated in the direction of the antenna through a partially absorptive atmosphere, T_{SC}. The following equations summarize the relationship among the aforementioned components:

$$T_{AP}(\theta,\lambda,p) = T_{UP}(\theta,\lambda) + \frac{1}{L_a(\theta,\lambda)}\left(T_{BS}(\theta,\lambda,\rho) + T_{SC}(\theta,\lambda,\rho)\right) \qquad (2.13)$$

where T_{SC} is defined as:

$$T_{SC}(\theta,\lambda,p) = (1-\varepsilon(\theta,\lambda,p)) \times \left(T_{DN}(\theta,\lambda) + \frac{1}{L_a(\theta,\lambda)} T_{EX} \right) \qquad (2.14)$$

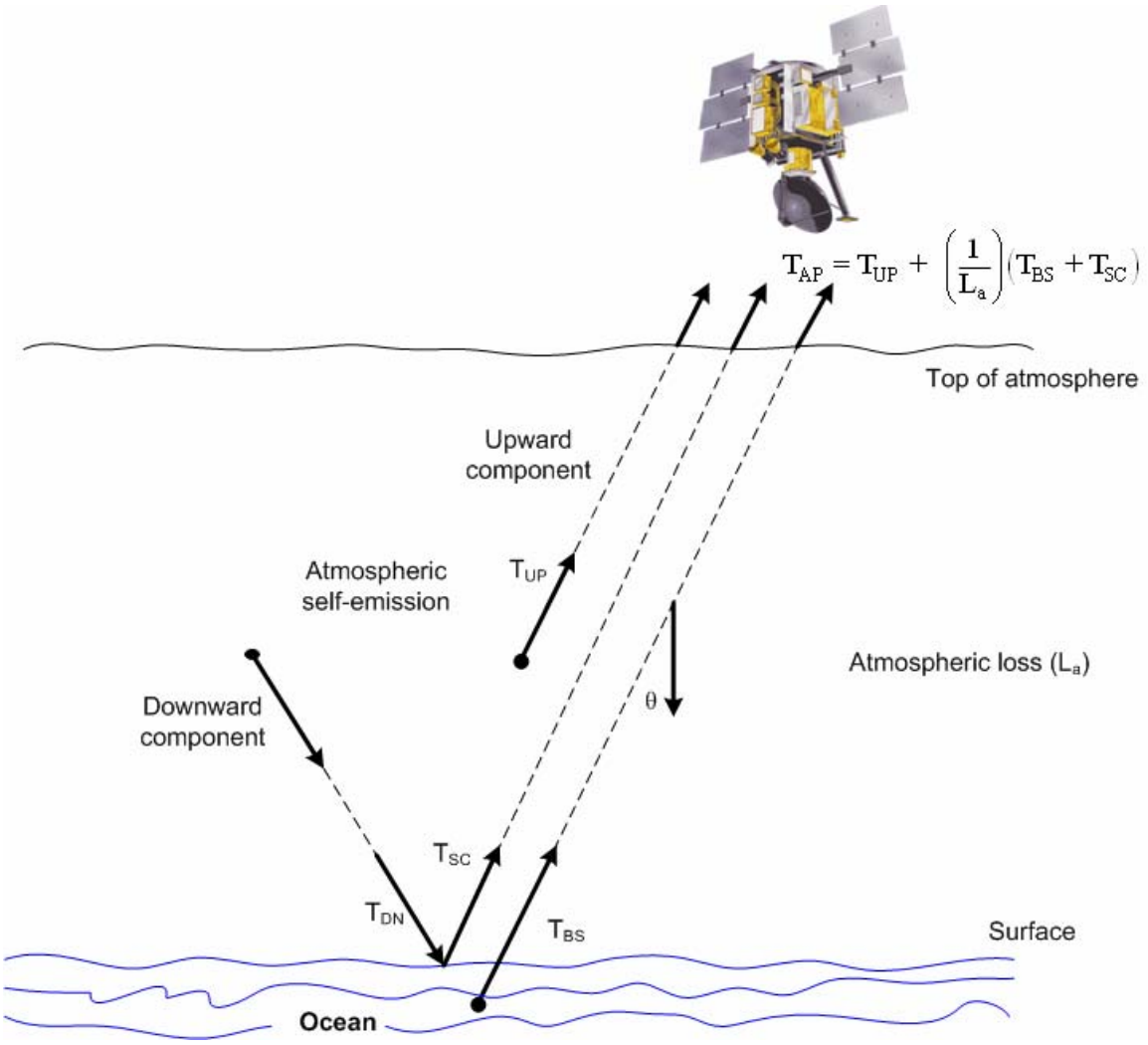

Figure 5: Space-borne radiomter observing the ocean at nadir angle θ

In the above formulation, T_{AP} represents the total radiation incident upon the antenna, which is a function of incidence angle θ, electromagnetic wavelength λ, and the EM polarization, p. L_a represents the atmospheric losses, ε is the ocean emissivity, and T_{EX} is the extraterrestrial radiation (~ about 3 K) incident upon the ocean surface.

By appropriate selection of operating frequencies and taking independent measurements (different frequencies and polarizations), space-borne microwave radiometers are capable of retrieving multiple unknown geophysical parameters, and

predicting the profile of a particular variable of interest. The number of required brightness temperature observations should at least equal or larger than the number of geophysical parameters.

There are three major types of radiometers: the total power radiometer, Dicke Radiometer and noise-injection radiometer. Among them, total power radiometer has the simplest design, which is comprised of an antenna, a microwave receiver with a power detector. An important parameter used to characterize the performance of the radiometer, and assess its measurement accuracy, is known as radiometer sensitivity or radiometric resolution, ΔT, which is defined as the smallest change in measured brightness temperature that can be detected at the radiometer input. The radiometric resolution for the total power radiometer is given by the following expression [5]:

$$\Delta T = T_{sys}\sqrt{\frac{1}{B\tau}+\left(\frac{\Delta G_{sys}}{G_{sys}}\right)^2} \tag{2.15}$$

Where: τ is the integration time, B is the bandwidth of the receiver, T_{SYS} represents the system noise temperature (which is the sum of the antenna and receiver noise temperatures), ΔG_{sys} is the effective value (rms) of power gain variation, and G_{sys} is the average system power gain. In the ideal model, power gain variation is neglected. The sensitivity of the total power radiometer is half the sensitivity of the Dicke and noise injection radiometers.

Satellite Radiometer Missions

Historically, space-borne passive microwave observations of planet Earth were initiated in 1960s by the launch of the Russian Cosmos-234 satellite, which carried four microwave radiometers [5]. Since then, passive microwave radiometry from space has established itself as an essential part in the field of remote sensing the Earth's environment. In early 1970s, several passive microwave radiometers have flown on a number of space-borne platforms.

The Electronically Scanned Microwave Radiometer (ESMR) was launched aboard Nimbus 5 and Nimbus 6 satellites in 1972 and 1976 respectively. The ESMR was a single channel instrument operating at a frequency of 19.35 GHz, and scanning ±45º cross track of nadir, providing global images of microwave emission with a spatial resolution of the order of 25 ~ 50 km [3, 5].

In 1978, the Scanning Multi-channel Microwave Radiometer (SMMR) was launched onboard Seasat and Nimbus-7 satellites. It measured the brightness temperature at five frequencies 6.6, 10.7, 18, 21.3 and 37 GHz for both vertical and horizontal polarizations. Measurements from the SMMR radiometers were used to infer a multiple number of surface and atmospheric parameters including wind speed, sea temperature, soil moisture, snow cover, water vapor, liquid water content and rain rate [3, 5].

A major milestone in space-borne microwave radiometry was achieved after the launch of the Special Sensor Microwave Imager (SSM/I) onboard the Defense Meteorological Satellite Program (DMSP). The first SSM/I was launched in 1987, and since then several additional SSM/I instruments have been launched. The SSM/I is a

conical scanning radiometer that measures the radiation intensity using seven channels: 19.35 H/V, 22.235 V, 37 H/V and 85.5 H/V GHz [15]. The SSM/I radiometers have proved themselves as stable and well calibrated instruments, and have been very useful in measuring several geophysical parameters including rainfall.

In November 1997, the Tropical Rainfall Measuring Mission (TRMM) satellite was launched into space. As the name implies, the primary focus of the TRMM mission is to measure the rainfall over the tropics. One of the primary microwave sensors onboard TRMM is the TRMM Microwave Imager (TMI) [16, 17]. TMI is a conical scanning sensor that consists of nine total power radiometers to measure the emission from the Earth and atmosphere using four dual polarization frequencies (10.7, 19, 37, 85 GHz) and one single polarization (V-pol) channel at 21.3 GHz. TMI has a similar design to the SSM/I instrument, with some exceptions. TMI has two additional channels at 10.7 GHz. Also, the water vapor channel for TMI is moved to 21.3 GHz as compared to 22.235 for the SSM/I instrument

In 2002, two microwave radiometers developed by Japan Aerospace Exploration Agency (JAXA) were launched into space: the first is the Advanced Microwave Scanning Radiometer (AMSR) which flew onboard the Japan's Advanced Earth Observing Satellite-II (ADEOS-II). The second radiometer is AMSR-E launched onboard NASA's Aqua satellite [18]. AMSR is a total-power microwave radiometer, measuring emission at eight-frequencies, with dual polarization at 6.925, 10.65, 18.7, 23.8, 36.5, and 89.0 GHz, and two vertical channels at 50.3, and 52.8 GHz. AMSR employs a 2.0 meter diameter offset-parabolic antenna which is the largest space-borne microwave radiometer antenna of its kind. The AMSR-E radiometer is a modified version of AMSR to accommodate

Aqua platform. Major modifications include the exclusion of the 50 GHz channels and the use of a smaller (1.6 meter) deployable antenna. Measurements from both sensors have been utilized to retrieve several geophysical parameters including rainfall.

The WindSat radiometer was launched in January 2003 onboard the Coriolis satellite. It is the world's first polarmetric radiometer designed to measure the wind vector over the oceans. The WindSat radiometer employs a conical scanning six- foot spinning offset parabolic reflector to collect the polarized microwave emissions using a forward look swath (±60º azimuth), and a aft look (from 120º ~ 180º) in azimuth. The WindSat microwave radiometer consists of twenty-two channels, operating at five frequencies of 6.8, 10.7, 18.7, 23.8 and 37.0 GHz. While the 10.7, 18.7 and 37.0 GHz channels are fully polarimetric (H, V, ± 45° & LHCP/RHCP), the 6.8 and 23.8 GHz channels are only dual (H, V) polarized [19].

SeaWinds Sensor

Instrument Description

The SeaWinds sensor onboard QuikSCAT satellite (and by implication, SeaWinds on ADEOS-II satellite) is a conical scanning long-pulse radar system originally designed to measure the backscatter from the ocean surface to infer surface wind speed and direction [20]. SeaWinds has two receiver channels, which allow the received backscatter

signal (echo) and the black-body microwave emission (noise) from the ocean surface and interviewing atmosphere to be separated. Although, quantitative microwave brightness temperature measurements were not originally envisioned; never the less, the QuikSCAT radiometric function has been implemented post-launch through ground signal processing. This passive radiometric measuring capability is known as QuikSCAT Radiomter (QRad).

SeaWinds measures the linearly polarized microwave active radar backscatter, σ^0, and passive brightness temperature, T_b, at a Ku-band frequency of 13.4 GHz. To collect the measurements, SeaWinds utilizes a 1 meter diameter parabolic dish antenna, which is mechanically at 18 rpm counter clockwise as the spacecraft moves in orbit. The conical scan traces helical patterns on the surface and provides a continuous 1800 km swath, which can cover about 90% of the ocean surface in one day. The SeaWinds measurement geometry is depicted Figure 6 below.

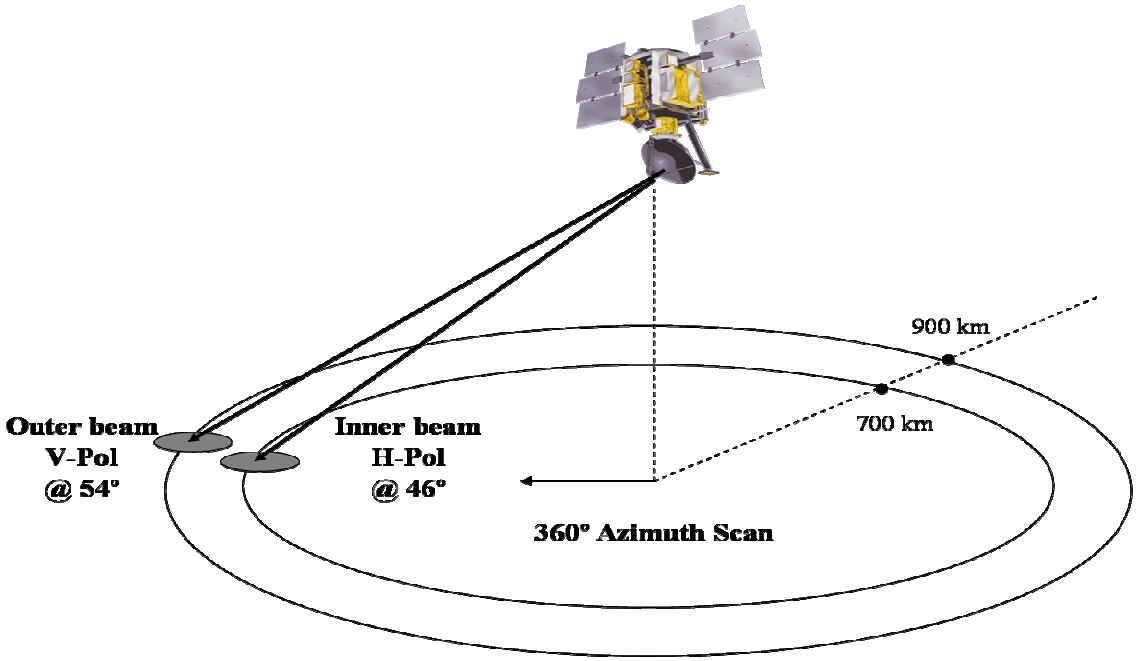

Figure 6 : SeaWinds measurement geometry.

Microwave backscatter and emission measurements are collected over the entire conical scan (forward and aft looking) with separate offset "pencil beams" at 46° incidence (horizontal polarization, H-pol) and 54.1° incidence (vertical polarization, V-pol). Individual σ^0's and Tb's are averaged on a spacecraft measurement grid of wind vector cells at 25 km resolution that results in mean horizontal and vertical T_b's collocated with the normalized backscatter measurements, σ^0's. The pulse repetition frequency and antenna scan rate have been designed to provide approximately 50% overlap of the instantaneous field of view (IFOV) in both the along track and cross track directions. Next, an overview of the QRad instrument and its radiometric calibration are provided [6, 21].

Radiometric Calibration

Designed as a radar, SeaWinds is not an optimum radiometer. Brightness temperatures (T_b's) are calculated for each received pulse with an equivalent integration time of 1.5 ms and a noise bandwidth of only 750 KHz. Because of the limited time-bandwidth product, the radiometric precision is much lower than desired (ΔT = 27 Kelvin/pulse). For QRad rain measurements, this can be partially ameliorated by using spatial and temporal averaging of individual pulses, where both forward-looking and aft-looking azimuth directions are collocated onto a 25 km wind vector cell (WVC) measurement grid. Further, a 3x3 spatial averaging filter is applied on the WVCs to

reduce the unwanted random noise component of the measurement. Each WVC polarized T_b observation is the average of about 54 pulses that results in a $\Delta T \sim 5$ K.

Unfortunately, for QRad there are no provisions for the usual two-point, hot and cold, absolute brightness temperature calibration. However, the QRad radiometric gain calibration is accomplished once per antenna scan using an internal ambient temperature (warm) load in the receiver; and the T_b offset is established one time, in an on-orbit calibration in 2000, using external comparisons with a well-known natural black-body sources (the Amazon rain forest) and with selected rain-free ocean T_b measurement comparisons with TMI.

For the ocean calibration, rain-free QRad polarized T_b's are averaged for 3-days and are spatially collocated with TMI brightness measurements (over ± 40° latitude on a 0.25° latitude x 0.25° longitude grid). Because the polarized ocean T_b's change with frequency and because TMI does not have a 13.4 GHz channel, a translation of TMI brightness temperatures must be performed before direct comparisons are possible with QRad. For TMI, the two lowest frequency channels (10.7 and 19.4 GHz) bracket the QRad frequency at 13.4 GHz; however, the incidence angles do not match. The TMI incidence angle is 52.8° for all channels; whereas, for QRad, the inner (H-pol) beam is 46° and the outer (V-pol) beam is 54.1°. Thus, as described below, TMI T_b's are interpolated over frequency and extrapolated over incidence angle to create QRad equivalent T_b's, which are used to establish the QRad absolute radiometric offset.

Over oceans, a microwave radiative transfer model developed by Wisler and Hollinger [22] is used to calculate the theoretical T_b's for both QRad and TMI channels. At vertical polarization, QRad and TMI measurements are at similar incidence angles;

thus, TMI measurements are mostly frequency interpolated with a small incidence angle correction. For horizontal, the 7° difference in incidence angle requires a significant incidence angle adjustment as well as frequency interpolation. Using the radiative transfer model, theoretical T_b values are used to determine a non-linear interpolation, thus producing the equivalent QRad Tb's from TMI observations at 10.7 and 19 GHz.

$$Tb_{13.4} = Tb_{10.7} + sr(Tb_{19.4} - Tb_{10.7}) \tag{2.16}$$

where sr is a "spectral ratio," defined as:

$$sr = \frac{Tb_{13.4} - Tb_{10.7}}{Tb_{19.4} - Tb_{10.7}} \tag{2.17}$$

Analysis has shown that this spectral ratio yields equivalent QRad T_b's accurate to within a few Kelvin [6, 21]. However, for the given frequencies, this spectral ratio exhibits a nearly exponential dependence on atmospheric columnar water vapor as shown in Figure 7. To derive this spectral ratio, over 72,000 ocean T_b points were simulated at each 10.9, 13.4 and 19.4 GHz using atmospheric and oceanic environmental parameters from SSMI F-13 and NOAA NCEP numerical weather analysis. The spectral ratio was then calculated at each T_b location and binned and averaged in 2 mm water vapor bins

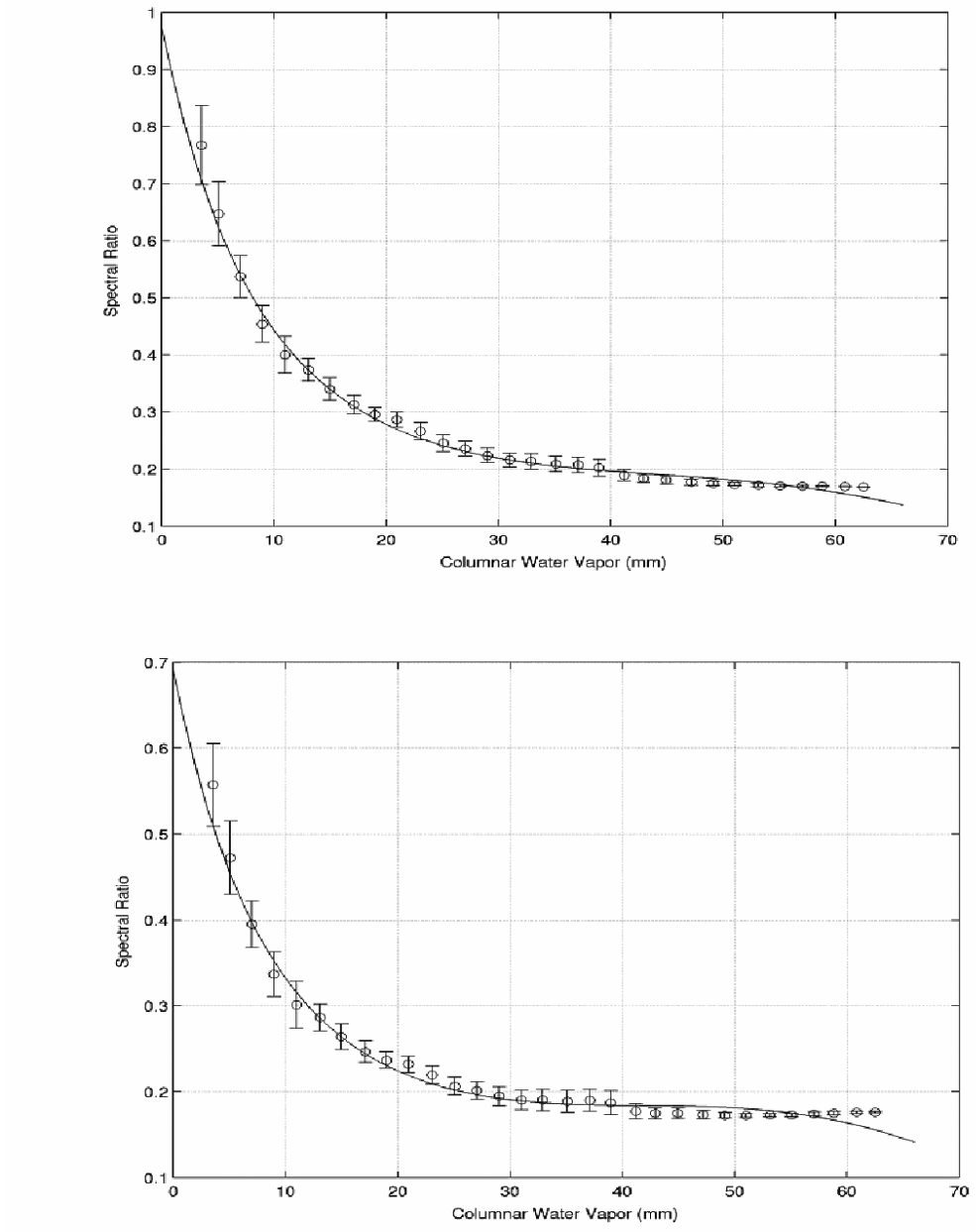

Figure 7: Brightness temperature spectral ratio as a function of columnar water vapor. Top panel is a plot of horizontal polarization, bottom panel is the vertical polarization. Circles denote binned/averaged data and the error bars show ± one standard deviation. The solid line shows the third order polynomial fit.

represented by circles. The error bars denote ± one standard deviation. The natural logarithm of the spectral ratio was then regressed against water vapor using a third order polynomial fit shown by the solid line. Thus, an estimate of the columnar water vapor, derived from collocated TMI retrievals, is used to select the proper value for the spectral ratio.

Further, because the orbital measurement swaths for QRad and TMI are not collocated simultaneously, transient rain events are present in both ocean data sets that can produce significant differences (10's of Kelvin) at a given locations. This error is effectively removed by editing the data using TMI (and QRad) rain flags. If either instrument indicates rain, the location is deleted.

For land, the emissivity is more complex, and the radiation transfer model was not used to produce equivalent QRad T_b's. However, the Amazon rain forest was used because it is a large isotropic and nearly homogeneous target that is an approximate blackbody with a brightness of about 285 K over this range of frequencies. Small diurnal effects of a few Kelvin have been observed in SSM/I measurements during ascending and descending pass times that are separated by approximately 12 hours, but during the 3-day average QRad Amazon comparisons, the TMI measured brightness temperatures at 10.7 and 19.4 GHz were averaged and linearly interpolated to compare with QRad T_b's.

An example of the linear regression scatter diagrams for QRad and TMI equivalent T_b's is given in Figure 8 for both H- and V-pols; and an expanded view of the difference between QRad and TMI measurements is shown in Figure 9. The symbols are binned average data on the TMI T_b; and the error bars denote ± one standard deviation.

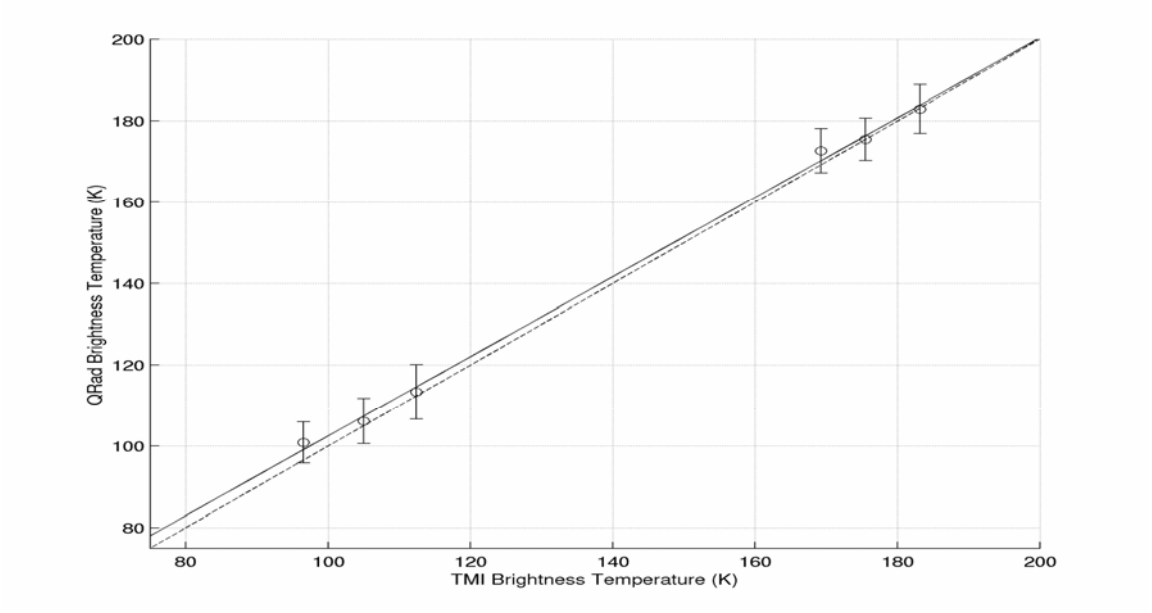

Figure 8: Comparison of QRad and TMI ocean brightness temperatures for rain-free five day averages. Circles are binned / averaged data, and error bars represent ± one standard deviation. Dashed line is perfect agreement and solid line shows least squares regression

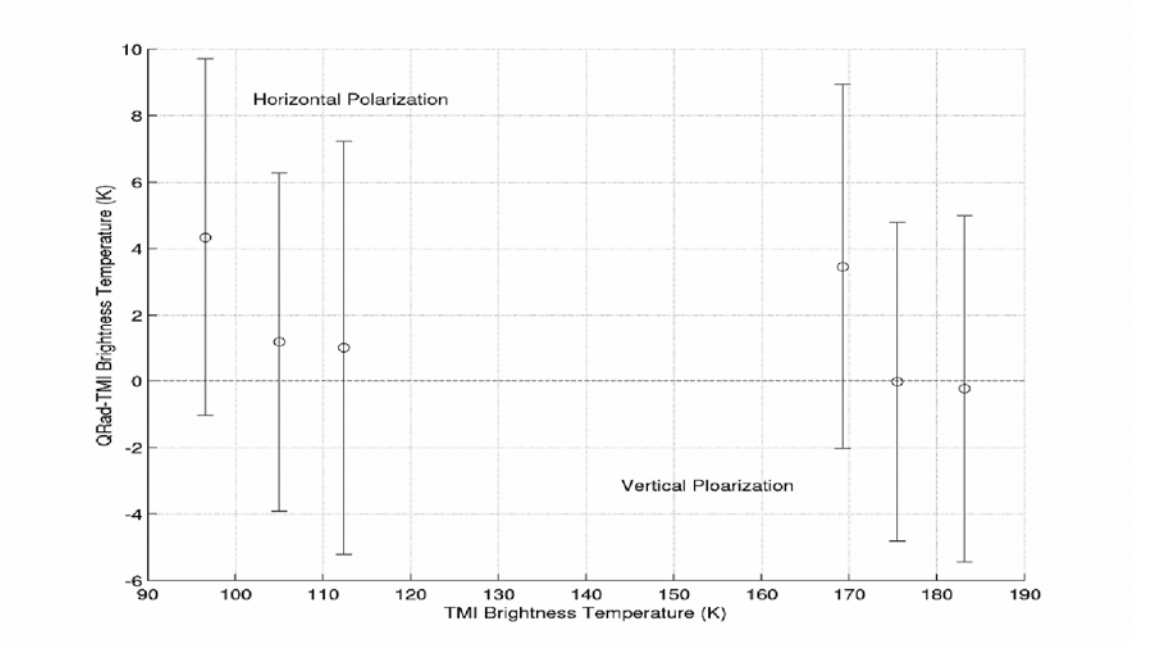

Figure 9: Five-day average oceanic brightness temperature differences (QRad – TMI) for rain-free ocean, April 2003. Circles are binned / averaged in 5 K bins by TMI, and error bars denote ± one standard deviation.

The stability of this external calibration procedure is good as observed from the resulting regression slope and offset for several different calibrations during 2000 that are provided in Table 1 below.

Table 1: Linear fit of QRad to TMI ocean brightness temperatures. Data is rain-free combined horizontal and vertical polarization three-day averaged ocean brightness temperatures. TMI brightness temperatures are interpolated to QRad frequency and extrapolated to QRad incidence angle.

Date	Offset	Slope
Sept. '99	6.55 K	0.977
June '00	6.32 K	0.955
Jan. '01	9.07 K	0.958
Apr. '03	4.67 K	0.978

Another assessment of the calibration stability compares histograms of QRad and TMI equivalent ocean T_b's taken seasonally. Here, three-day sets of average ocean brightness temperatures were produced with rain removed, and a typical set of histograms is shown in Figure 10. For H-pol, the QRad median T_b is within a Kelvin of TMI; but for V-pol, the QRad results are low by a few Kelvin. Also QRad histograms are broader as the result of the increased QRad ΔT. The year 2000 calibration statistics are tabulated in Table 2; and when taken over the year, the median differences show a slight systematic variation, which may be related to the QuikSCAT seasonal thermal environment. Over a period of one year, the global mean of this variation is -0.29 K with a standard deviation of 0.85 for horizontal and correspondingly -2.76 K with a standard deviation of 0.75 for

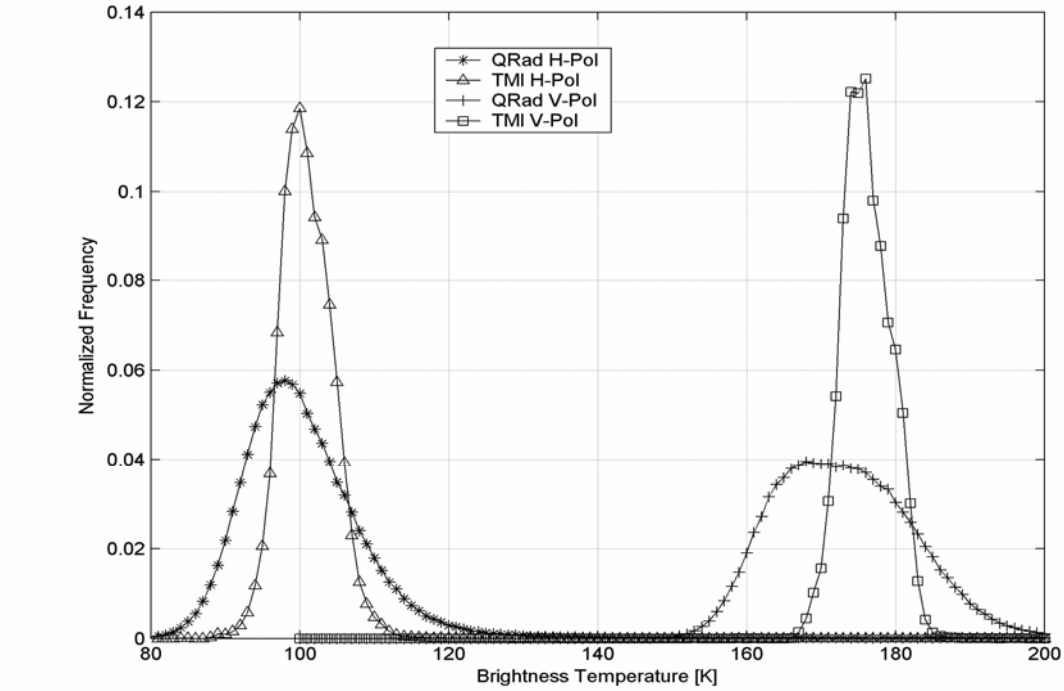

Figure 10: Three-day average, rain-free, ocean brightness temperature probability density function, January 15 – 17, 2000.

Table 2: Median seasonal ocean brightness temperatures for year 2000. Brightness temperatures are rain-free three-day average. TMI brightness temperatures are interpolated to QRad frequency and extrapolated to QRad incidence angle.

Date	Qrad (H-pol)	TMI (H-pol)	Qrad (V-pol)	TMI (V-pol)
January	99.4	100.7	172.6	175.9
March	101.1	101.5	173.1	176.4
April	100.0	101.2	172.7	176.5
July	101.2	101.1	173.7	175.7
September	100.3	100.4	173.7	175.6
October	100.3	100.4	173.7	175.6

vertical. Again these results demonstrate that QRad and TMI derived equivalent T_b agree on average to within a few Kelvin.

The final example of relative T_b stability is shown in the approximately two-year T_b time series given in Figure 11. The object of this comparison is to assess whether or not there are variable T_b biases caused by the seasonal solar heating of the satellite and instrument. This is important because the QRad transfer function uses the physical temperature of the front-end losses to calculate T_b. For this evaluation, the polarized brightness temperatures are averaged over all pixels for a repeating (every 4-day) ground swath in the middle of the Pacific ocean between ± 45° latitude. During this evaluation, it was discovered that this orbit average T_b is very stable even when rain pixels are included. Because both earth hemispheres (± latitudes) are included, the seasonal rain effects appear to cancel and the mean T_b is very stable. In late 1999, a small step in T_b is visible, which corresponds to a change in the QRad range gate width (equivalent to integration time); but since then there have been no changes in the instrument transfer function. In Figure 12, the QRad average polarized T_b deviation from its polarized time series mean is displayed for these repeating ground tracks, and over this two-year period, the rms difference about the mean is 1.4 K for both polarizations. It is encouraging that both polarized brightness temperature deviations overlay and that they are consistent with the previous analysis presented above, which shows a small seasonal variation. These results demonstrate the stability and effectiveness of this external calibration technique used for QRad; and in fact, this external TMI calibration has produced very consistent results over the entire five years that QRad has been in operation.

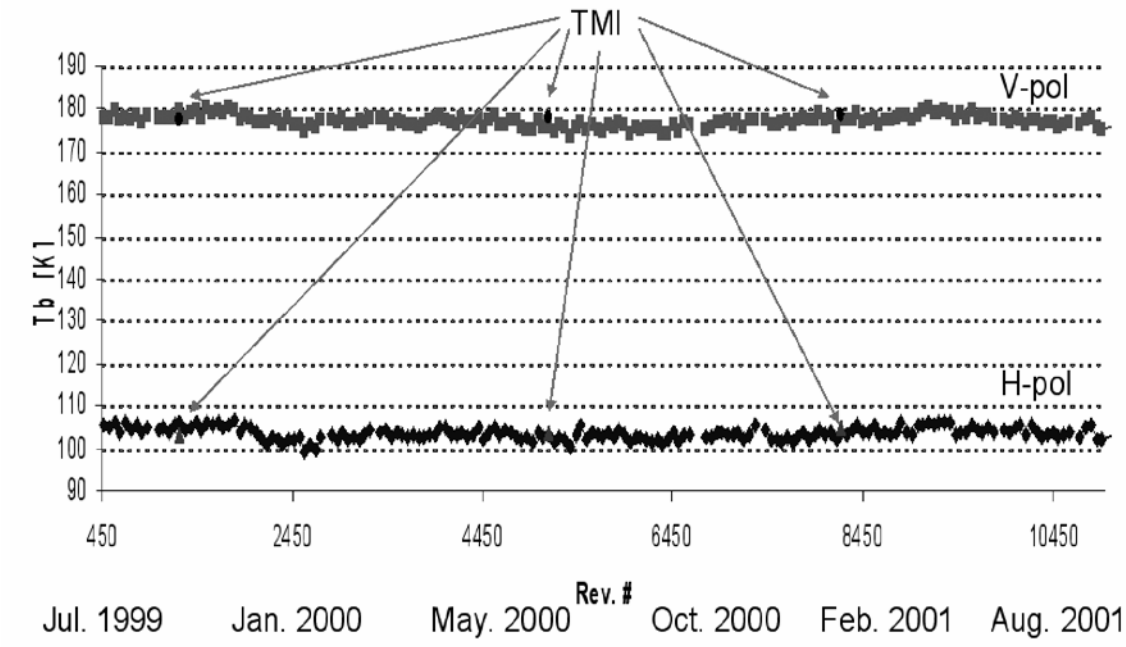

Figure 11: Pacific Ocean brightness temperature time series from QRad for repeating ground swath at approximately four-day sampling.

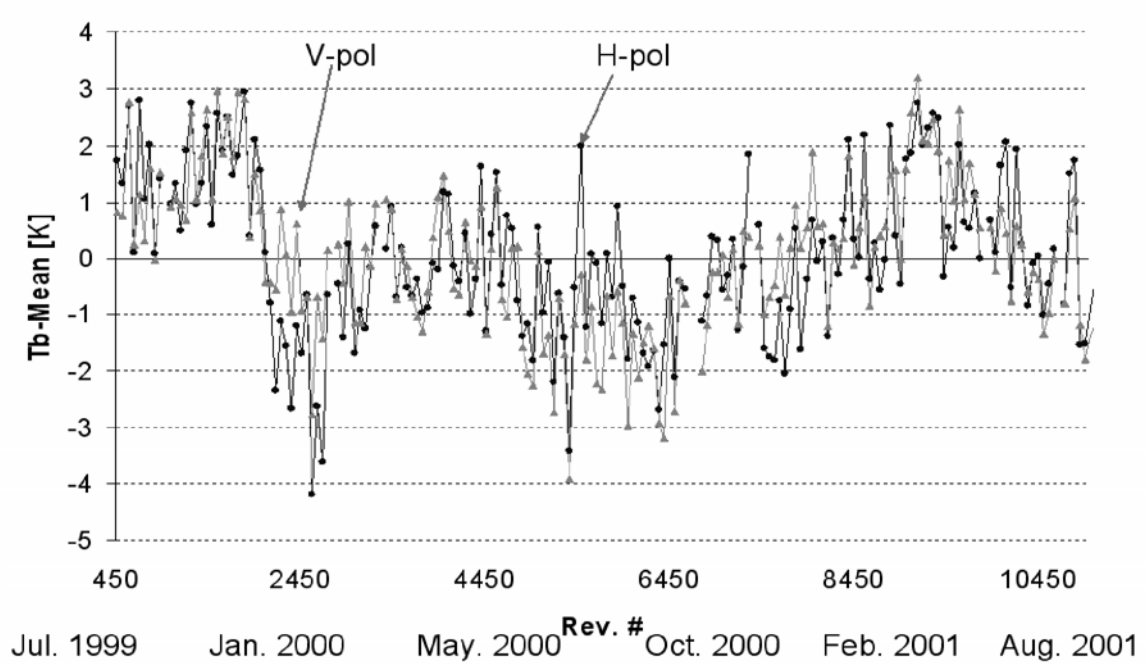

Figure 12: Pacific Ocean brightness temperature deviation from the mean. Measurements are for repeating ground swaths, approximately four days separation.

CHAPTER THREE: REMOTE SENSING OF OCEANIC RAINFALL FROM SATELLITE-BORNE MICROWAVE OBSERVATIONS

Introduction

Rainfall over oceans and its associated latent heat release play an important role in the Earth's hydrological cycle, atmospheric circulation, oceanic thermohaline circulation (circulation driven by salinity density differences), and the world's food as well as fresh water supplies. Additionally, the availability of the oceanic rainfall data is of vital significance for scientists and researchers involved in modeling and predicting the Earth's weather and climate systems.

The harsh marine environment combined with the vast area of the ocean surfaces (~ 70% of the Earth surface), can make a direct in-situ measurement of rainfall over the ocean an extremely problematic process. On the other hand, remote sensing techniques utilizing satellite infrared and microwave observations provide near global mapping and more uniform sampling of the oceanic rainfall than is available from in situ measurements.

Unlike the infrared measurements which are only indirectly related to rain, microwave remote sensing has more direct interaction with the rain volume, and as a result, has evolved as a primary source for estimating the rainfall over the oceans. The estimation of rain rate is made possible due to the absorption/emission and scattering signatures of atmospheric rain volume on microwave radiation.

This chapter presents an overview of the techniques and algorithms used for inferring oceanic rainfall from microwave radiometer and scatterometer observations. After a brief review of the theoretical basis of the interaction between rain volume and microwave radiation, an overview of several types of algorithms used for the retrieval of oceanic rainfall from passive microwave space-borne radiometers is presented. Next, research efforts conducted by science community to estimate rain over the oceans from space-borne scatterometer measurements, with a focus on the SeaWinds instrument will be highlighted.

Interaction of Microwave Radiation with Rain

The interaction between matter and electromagnetic radiation can be generally described by two processes: emission and extinction [2, 3, 5]. When the radiation traversing the medium is reduced in intensity, we have extinction. In contrast, if the medium under consideration adds energy of its own, we have emission. Usually, these two processes occur simultaneously.

The energy lost by extinction maybe absorbed by the material, scattered, or both. The absorption loss, which is governed by the conductivity of the medium, occurs when energy is transformed into other forms, such as heat. On the other hand, scattering loss is caused by energy traveling in directions other than the direction of incident radiation and is governed by the degree of inhomogeneity of the dielectric properties of the medium.

Absorption and scattering are linear processes, and they are characterized by the absorption coefficient (κ_a) and the scattering coefficient (κ_s) respectively. The extinction coefficient (κ_e) is defined as the linear sum:

$$\kappa_e = \kappa_a + \kappa_s \tag{3.1}$$

In a medium that absorbs and/or scatters radiation (e.g. the Earth's atmosphere), the solution of the radiative transfer equation (RTE) in the microwave region of the electromagnetic spectrum is given by [3, 5]:

$$T_{AP}(r) = T_{AP}(0) \cdot e^{-\tau(0,r)} + \int_0^r \kappa_e(r') \cdot \left[(1-a) \cdot T(r') + a \cdot T_{SC}(r') \right] \cdot e^{-\tau(r',r)} dr' \tag{3.2}$$

The above equation states that the apparent temperature at any observation point r, in a certain direction is defined as the sum of two terms. The first term is the apparent temperature at the boundary $T_{AP}(0)$, which is reduced in magnitude by an exponential factor due to the extinction by the medium between 0 and r. The second term represents the emission and scattering along the propagation direction within the medium. The single scattering albedo, a, is defined as the ratio:

$$a = \frac{\kappa_s}{\kappa_e} \tag{3.3}$$

T(r) is the physical temperature of the medium at point r. The optical thickness along a range from r_1 to r_2 is given by:

$$\tau(r_1, r_2) = \int_{r_1}^{r_2} \kappa_e \, dr \tag{3.4}$$

The scattered temperature $T_{SC}(r)$ accounts for apparent temperature scattered in the r direction in terms of incident radiation from all directions, and can be expressed as:

$$T_{SC}(r) = \frac{1}{4 \cdot \pi} \cdot \iint_{4\pi} \psi(r, r_i) \cdot T_{AP}(r_i) \, d\Omega_i \tag{3.5}$$

where $\psi(r, r_i)$ is known as the phase function that accounts for the portion of radiation scattered from incidence direction r_i into r direction. It should be noted that when both scattering and absorption are present, the general solution of $T_{AP}(r)$ given by Equation 3.2 requires the evaluation of an integral that involves the scattered radiometric temperature $T_{SC}(r)$, which itself has an integral form that requires knowledge of $T_{AP}(r_i)$ incident from all directions over the 4π solid angle, which leads to complicated calculations. However, if scattering contribution is negligible, i.e., the single scattering albedo $a<<1$, the complexity of the problem can be substantially reduced, and under such condition, $T_{AP}(r)$ can be directly integrated.

In the presence of rain, the applicability of the scatter free assumption within the Earth's atmosphere depends on the density and the drop size distribution of the rain

droplets relative to the observation wavelength. Next, we focus the discussion on the interaction of rain particles with microwave radiation including extinction (attenuation), backscattering and emission effects. We first consider the interaction with a single spherical particle, then, we extend the discussion to treat a large number of particles within an atmospheric rain volume.

The general mathematical solution for the scattering and absorption of EM waves by a dielectric sphere of arbitrary radius was first introduced by Mie in 1908, and applied to the context of rain by Gunn and East in 1954 [5]. For a spherical rain particle within the atmosphere, the scattering and absorption characteristics are governed by the radius of the particle, r, the wavelength, λ_0, and the complex index of refraction, n.

For a single raindrop particle whose size is much smaller than the EM wave wavelength, Rayleigh approximations to the exact Mie expressions applies. In this limit, the absorption cross section which is defined as the ratio of absorbed power to the incident power density ($Q_a = P_a/S_i$) is proportional to the cube of the particle diameter, and hence, proportional to the volume and mass of the rain drop, while the scattering cross section becomes negligible by comparison. As the size of the raindrop becomes comparable to the EM wavelength, its absorption per unit mass increases and scattering may no longer be ignored.

In a rain volume, the individual particles (raindrops) are usually assumed to be randomly distributed, and therefore, their individual contributions can be summed incoherently to compute the scattering and absorption by a volume containing many rain particles. The range of different rain particle sizes within a rain mass is usually described by a continuous function, known as the drop size distribution p(r), which defines the

concentration of particles per unit volume per unit increment of the drop radius. In literature, the most widely used drop size distributions are Marshall-Palmer and Laws-Parsons distributions, which are in reasonable agreement with one another.

The extinction and backscattering effects of rain volume on microwave radiation are characterized by the rain volume extinction coefficient (κ_e) and the rain volume backscattering coefficient (σ_υ) [3, 5]. The rain volume extinction coefficient (κ_e) is defined as the total rain extinction cross section per unit volume. It has the units of ($Np.m^{-3}.\ m^2 = Np.m^{-1}$), and can be expressed in terms of a dimensionless parameter ($\chi = 2\pi r/\lambda_0$), and the drop size distribution $p(\chi)$ within the rain volume as

$$\kappa_e = \frac{\lambda_0^{\,3}}{8\pi^2}\int_0^\infty \chi^2 \cdot p(\chi)\cdot \xi_e(\chi)\, d\chi \tag{3.6}$$

where ξ_e is the Mie extinction efficiency, which is defined as the algebraic sum of the scattering and absorption cross sections, Q_s and Q_a respectively, normalized by the spherical raindrop cross section area ($A = \pi r^2$), therefore

$$\xi_e = \frac{Q_s + Q_a}{\pi \cdot r^2} \tag{3.7}$$

In practice, it is desirable to relate the rain volume extinction coefficient (κ_e) directly to the rain rate (R). A power law relationship of the following form is commonly used

$$\kappa_e = k \cdot R^b \tag{3.8}$$

where b is a dimensionless parameter, R is the rain rate in mm/hr, and k has the units of $dB.km^{-1}$ per $mm.hr^{-1}$. Both parameters k and b are dependant on the operating frequency. Typical values for k and b over a wide range of frequency are given by Olsen et al [23]. It should be noted that κ_e in $dB.km^{-1}$ is obtained by multiplying κ_e in $Np.m^{-1}$ by the constant $4.34x10^3$.

The rain volume backscattering coefficient σ_υ, which is often called the radar reflectivity, can be calculated using a similar form to Equation 3.6:

$$\sigma_\upsilon = \frac{\lambda_0^{\,3}}{8\pi^2} \int_0^\infty \chi^2 \cdot p(\chi) \cdot \xi_b(\chi) d\chi \tag{3.9}$$

where ξ_b is the Mie backscattering efficiency, defined as ratio of the radar backscattering cross section σ_b to the cross section area of a spherical particle

$$\xi_b = \frac{\sigma_b}{\pi \cdot r^2} \tag{3.10}$$

In the Rayleigh region, an approximate expression for σ_υ can be derived. For an individual rain particle of radius r, the radar backscattering cross section, σ_b, can be approximated as [5]

$$\sigma_b = \frac{64\pi^5}{\lambda_0^4} \cdot r^6 \cdot |K|^2 \tag{3.11}$$

where

$$K = \frac{n^2 - 1}{n^2 + 2} \tag{3.12}$$

The complex quantity, K, is defined in terms of the complex refractive index of water, n. The factor $|K|^2$ varies as a function of temperature and frequency. For example, over the 0^0-20^0C temperature range and 1-10 cm wavelength range, $|K|^2$ for water vary between 0.89 and 0.93 [5].

In a rain volume containing N_v particles, the rain volume backscattering coefficient can be written by virtue of Equation 3.11 as

$$\sigma_\upsilon = \sum_{i=1}^{N_v} \sigma_b(r_i) = \frac{64\pi^5}{\lambda_0^4} \cdot |K|^2 \cdot \sum_{i=1}^{N_v} r_i^6 \tag{3.13}$$

By definition, the reflectivity factor Z is given by

$$Z = \sum_{i=1}^{N_v} d_i \tag{3.14}$$

where $d_i = 2r_i$ is the diameter of the i^{th} rain particle. Using equation above, and expressing d_i in units of meters, Z in mm^6 per m^3, λ_0 in cm, leads to the simplified expression

$$\sigma_\upsilon = 10^{-10} \cdot \frac{\pi^5}{\lambda_0^{\,4}} \cdot |K|^2 \cdot Z \tag{3.15}$$

since σ_υ physically represents the total rain backscattering cross section in m^2 per unit volume in m^3, thus, it has the units of m^{-1}.

In literature, it is a common practice to relate the reflectivity factor Z [mm^6/m^3] directly to the rain rate R [mm/hr] via the well known Z-R relationships which have the following general form

$$Z = a \cdot R^b \tag{3.16}$$

where the parameters, a, and, b, depends on the drop size distribution within a given rain volume.

In addition to its extinction and backscattering effects, the presence of rain in the atmosphere has a strong signature on the total emission of microwave radiation. To obtain a complete solution including scattering effects, the equation of radiative transfer must be solved numerically, however, in the centimeter wavelength region of the microwave spectrum, a rainy atmosphere can be considered a non scattering medium. In this case, the extinction coefficients of atmospheric gases, clouds and precipitation are

due primarily to absorption. The brightness temperature of a rain layer of vertical thickness, H, and physical temperature, T_p, can be approximated by

$$T_B = T_P\left(1 - \Upsilon_\theta\right) \tag{3.17}$$

where Υ_θ is the transmissivity of the rain layer, given by

$$\Upsilon_\theta = e^{-\kappa_a H \sec\theta} \tag{3.18}$$

The angle θ is measured from vertical. The total absorption coefficient, κ_a, consists of contributions due to precipitation, atmospheric gases and clouds. It is given by

$$\kappa_a = \kappa_p + \kappa_c + \kappa_g \tag{3.19}$$

The subscripts p, c and g refer to precipitation, clouds and gases respectively. Next, in the following two sections, a brief overview of the techniques commonly used for estimation of the oceanic rainfall using measurements from satellite-borne radiometers and scatterometers will be highlighted.

Oceanic Rainfall Estimation from Microwave Radiometer Observations

Unlike infrared measurements which are sensitive only to uppermost layer of the clouds, passive microwave observations have shown high sensitivity to rainfall due to the direct interaction between hydrometeors and the microwave radiation which is capable of penetrating clouds and providing more insight into the rain structure. Early studies of estimating precipitation using radiometric measurements from space took place at the end of 1960s. The first microwave radiometers were single frequency instruments, and initial retrieval algorithms focused on the idea that a single frequency measurement can be used to estimate a single rainfall parameter related to rain rate or rain accumulation through idealized brightness temperature-rain rate relationships [24]. After the launch of the Scanning Multichannel Microwave Radiometer (SMMR) which was the first multi-spectral microwave radiometer, launched onboard Nimbus-7 in 1978, retrieval algorithms reached a higher maturity level, and a door was opened for a new class of multi-channel algorithms in which different frequencies are used with the aid of an inversion scheme to retrieve a vector describing the rainfall profile [23]. In general, rainfall retrieval algorithms utilizing passive microwave observations can be categorized into four classes:

The first class of algorithms makes use of the emission characteristics of rainfall against the relatively colder ocean background, thereby, they are known as emission based algorithms [25]. For a space-borne microwave radiometer, the ocean surface appears uniformly cold due to its low surface emissivity (~0.5 for typical frequencies). The presence of raindrops in the atmosphere tends to absorb and re-emit radiation, thus, increase the observed brightness temperature. The emission type algorithms are more

suited to longer wavelengths, which tend to saturate at higher rainfall rates and are less sensitive to scattering effects. However, these algorithms are not applicable over land, where the emission signal is obscured by the high and variable surface emissivity. Also, the inhomogeneity of rainfall within the antenna footprint imposes a problem because of the coarse resolution of measuring frequencies.

The second class of algorithms is referred to as scattering algorithms [26]. As the microwave frequencies increase, scattering effects which are mainly due to ice particles found in raining clouds become more dominant. The scattering effect tends to reflect the upwelling radiation back to the surface, thus, lower the observed brightness temperatures. This type of algorithms can work both over land and water surface, and enjoy a relatively better spatial resolution offered by the high frequency channels. However, since scattering algorithms infer rain based on an indirect measure related to the cloud ice content, scattering algorithms are more susceptible to regional and temporal biases compared to emission based algorithms.

The third class of algorithms is the so called multi-channel regression algorithms [27]. These algorithms use theoretical radiative transfer calculations to derive the regression relationships. As a result, these algorithms become sensitive to the assumed vertical structure of the rain system, including cloud water, rain water and ice profiles. Moreover, these algorithms suffer from the same uncertainties found in aforementioned scattering algorithms.

The final class of algorithms is commonly referred to as profiling algorithms [28]. These algorithms utilize a large data base of potential hydrometeor profiles along with a radiative transfer model to calculate the corresponding brightness temperatures. Once a

database of profiles and associated brightness temperatures is established, the retrieval portion of the algorithm employs an inversion scheme to estimate the entire vertical structure of precipitation, given the set of measured brightness temperatures. The major drawback of these algorithms is being computationally intensive.

Oceanic Rainfall Estimation from Microwave Scatterometer Observations

As noted previously, a scatterometer is a specialized radar calibrated to make accurate measurements of the normalized radar backscatter coefficient, σ^0, of the Earth's surface. Over the ocean, the primary application of the scatterometer σ^0 measurements is to infer the speed and direction of the surface wind vector. The physical basis for the wind retrieval is the relationship between the radar backscatter measurements, σ^0, and the wind induced surface roughness. This relationship has been empirically derived and known as the geophysical model function (GMF) [29].

Traditionally, space-borne scatterometers are designed to operate at microwave frequencies in the C and Ku bands of the EM spectrum. Those microwave frequency bands are chosen to maximize the sensitivity to the surface wind, and minimize the atmospheric effects on the backscatter measurements. Although the atmosphere is nearly transparent to radiation at C and Ku bands under most weather conditions, the presence of rain can significantly modify the normalized radar cross section, σ^0, of the ocean surface measured by a satellite-borne scatterometer.

Rain is known to modify the strength of the scatterometer signal in three ways [30, 31]. Rain drops striking the ocean surface creates rings, stalks and crowns which cause additional surface scattering. Further, the presence of rain in the atmosphere introduces additional volume scattering and attenuates the transmitted microwave signal, and the signal backscattered from the surface. Depending on the relative magnitudes of the wind / rain combination, the aforementioned rain effects can degrade or even corrupt the oceanic wind retrieval process. This phenomenon is more pronounced on the backscatter measurements collected by Ku-band instruments as compared to C-band counterparts.

Therefore, in order to provide accurate retrievals of the oceanic wind vector from the σ^0 backscatter measurements, it is necessary to correct the apparent σ^0 measurements by removing the non-wind (rain related) effects of additional scattering and attenuation on the scatterometer microwave signal as it propagates through the atmosphere. For this purpose, studies have been conducted to identify (and correct where possible) the rain contaminated σ^0 measurements for previous satellite-borne scatterometer missions. In some cases, the scope of the conducted research was expanded to exploit the rain sensitivity on the scatterometer signal to provide quantitative estimates of the rainfall over the oceans.

Rain flagging and correction using brightness temperature measurements were attempted for the fan beam SEASAT scatterometer (SASS) σ^0 observations that were also sampled by the SEASAT SMMR radiometer [32]. However, the SASS rain correction process was complicated by the low and variable (with frequency) measurement resolution of the SMMR compared to the SASS cell size, and also by the collocation

difficulties associated with differences in earth incidence angles between the SMMR / SASS measurements.

The SeaWinds scatterometer is the first space-borne radar utilizing the pencil beam design. A single rotating 1-m parabolic dish generates beams from two feeds: a horizontally polarized inner beam at 46º incidence, and a vertically polarized outer beam at 54.1º incidence. Compared to previous fan beam instruments, the pencil beam design not only allows operation at discrete incidence angles but also affords wide contiguous swath coverage, without a nadir gap.

Rain effects on SeaWinds are found to be severe for low and moderate wind speeds [33]. If the geophysical model function (GMF) does not incorporate the rain scattering and attenuation effects, they are interpreted as wind induced features, which leads to systematic biases in the retrieved oceanic wind vector. The SeaWinds σ^0 measurements collected by polarized twin beams are particularly more sensitive to the presence of rain than previously flown scatterometers. The high rain sensitivity is mainly attributed to the Ku-band operating frequency and the large incidence angle pencil beam design of the SeaWinds instrument. While the SeaWinds rain sensitivity interferes with the measurement of the oceanic wind vector, it does however provide the instrument with an additional capability to estimate the rainfall over the oceans.

Several analysis studies have been conducted to investigate the rain sensitivity and quantify the impact of rain on SeaWinds scatterometer σ^0 measurements. Stiles and Yueh from the Jet Propulsion Laboratory (JPL) assumed that rain effects can be modeled using a simple linear relationship between SeaWinds polarized backscatter observations, σ^0_{meas}, and the wind induced surface backscatter, σ^0_{wind}:

$$\sigma^0_{meas} = \sigma^0_{rain} + \alpha \cdot \sigma^0_{wind} \tag{3.20}$$

where the coefficients of the linear relationship, α and σ^0_{rain}, represent the attenuation and the additional rain backscattering, respectively. These coefficients are rain dependent and empirically derived for each beam using collocated SeaWinds σ^0 observations with SSM/I rain measurement, and the National Center for Environmental Prediction (NCEP) wind fields. Stiles and Yueh determined that measurements from SeaWinds inner H-pol beam are more sensitive to rain than the outer V-pol beam. Also, they found that the sensitivity of both polarized beams to the presence of rain varies dramatically with wind speed.

Draper and Long [30] at Brigham Young University utilized the same simplified model of (3.20) to evaluate the effects of rain on the SeaWinds backscatter measurements, and improve the wind estimation in the presence of rain. They used data from TRMM Precipitation Radar (PR) to derive the rain induced attenuation and backscattering as seen by SeaWinds. Using the simplified model, they identified three backscatter regimes: the first is where rain backscatter overpowers that of the wind, it will be only possible to accurately retrieve rain rates. In the second regime where wind induced backscatter dominates, only wind can be accurately measured. In the third regime where the contributions from rain and wind are of the same order, simultaneous retrieval of rain and wind will be possible.

Another team of researchers (Weissman, Bourassa, O'Brien and Tongue) [33] studied the effects of rain on SeaWinds backscatter measurements by utilizing data from

National Data Buoy Center (NDBC) buoy measurements of wind, and ground based rain observations from National Weather Service Next Generation Weather Radar (NEXRAD). They found, as did Draper and Long, that SeaWinds σ^0 measurements are sensitive to the presence rain over the ocean. Also they believe that the dual polarization capability of the SeaWinds instrument might be helpful in rain detection process.

CHAPTER FOUR: SEAWINDS PASSIVE RAIN RETRIEVAL ALGORITHM

Introduction

The Ku-band microwave remote sensor, SeaWinds, was originally designed to measure the global ocean vector winds. Two identical SeaWinds instruments were launched into space. The first was flown onboard NASA QuikSCAT satellite which has been orbiting the Earth since June 1999, and the second instrument flew onboard the Japanese Advanced Earth Observing Satellite II (ADEOS-II) from December 2002 till October 2003 when an irrecoverable solar panel failure caused a premature end to the ADEOS-II satellite mission. In addition to measuring the radar backscatter, SeaWinds simultaneously measures the polarized microwave brightness temperature of the atmosphere / surface, and this passive microwave measurement capability is known as the QuikSCAT / SeaWinds (on ADEOS-II) Radiometer (QRad / SRad).

This chapter presents the development of a passive retrieval algorithm used to infer instantaneous oceanic rain rates using radiometric T_B measurements from the SeaWinds instrument. This statistical algorithm is trained using near-simultaneous observations of major rain events by QRad and the Tropical Rainfall Measuring Mission (TRMM) Microwave Imager (TMI). The same retrieval algorithm is applied to twin SeaWinds sensors onboard QuikSCAT and ADEOS-II satellite missions, and denoted as QRad / SRad rain retrieval algorithm, respectively. While an additional source for rain

estimation was available from the passive measurements of the Advanced Microwave Scanning Radiometer (AMSR) sensor onboard the short-lived ADEOS-II satellite, the passive QRad measurements are the only radiometric source used to derive oceanic rainfall from the ongoing QuikSCAT satellite mission. The continuous (without nadir gap), wide swath coverage, along with the corresponding extended data set of oceanic rain measurements (since 1999 till present) afford QRad a significant scientific utility of improving the sparse sampling of rainfall over the oceans. Further, since SeaWinds is the only sensor onboard QuikSCAT satellite, the passive QRad rain estimates can be used as an independent flag for quality control purposes to identify rain contaminated wind vector measurements derived from SeaWinds.

Following this introduction, a discussion of QRad oceanic sampling and its potential contribution to NASA's future Global Precipitation Measurement (GPM) Mission is presented. The third section presents a detailed discussion of the statistical QRad (and by implication, SRad) rain algorithm. The passive QRad / SRad rain algorithms have been implemented in NASA Jet Propulsion Laboratory (JPL) level 2B (L2B) science data product. The QRad / SRad rain measurements are available from JPL Physical Oceanography Distributed Data Archive (PO.DAAC).

QRad Oceanic Rain Sampling and the GPM Mission

For more than one decade, multi-frequency microwave radiometer imagers flying on low earth satellites have provided valuable day / night remote sensing of oceanic and atmospheric variables; but the emphasis on oceanic precipitation measurements achieved a significant advance with the launch of the Tropical Rainfall Measuring Mission (TRMM) observatory in late 1997. Because of TRMM's non-sun synchronous orbit, for the first time, precipitation measurements were available from a satellite over all local times so that the diurnal cycle of oceanic precipitation could be studied. However, from 1998 through late 2002, the ocean sampling was very sparse with only four such satellite instruments operating on-orbit; three Defense Meteorological Support Program (DMSP) satellites carrying the Special Sensor Microwave Imager (SSM/I), and the Tropical Rainfall Measuring Mission's (TRMM) Microwave Imager (TMI). The SSM/I's fly on near-polar sun synchronous satellites that provide greater than 90% earth coverage daily; however, since they fly in a day / night terminator orbit, they provide only morning and evening sampling times. On the other hand, the TMI flies in a low inclination (38°) non-sun synchronous orbit that has been optimized to measure tropical rainfall. TMI provides full diurnal sampling over the period of slightly greater than one month. However, even with the four passive microwave sensors, the statistics of oceanic rainfall were badly under-sampled. Since the fall of 2002, a fifth microwave imager, the Advanced Microwave Scanning Radiometer (AMSR-E) on NASA's Aqua earth observing system satellite began its ocean precipitation measurements; but even with this additional radiometer, the diurnal sampling is still less than desired.

Many researchers (e.g., Wilheit et al.[25] ; Petty and Katsaros [34]; Bell and Reid [35]; Chang et al. [36]; Imaoka and Spencer[37]) have studied diurnal sampling of oceanic precipitation using satellite microwave radiometers. Because of the sparse sampling, diurnal cycles must be estimated using large space-time averages, and likewise, it is difficult to determine the rainfall statistics for regional oceanic precipitation. In the future, a constellation of satellites known as the Global Precipitation Mission (GPM), [38, 39], will solve this observational shortage. This proposed constellation, comprised of satellites in low inclination and polar low-earth orbits (non-sun synchronous and sun synchronous), will provide near-global coverage with a worst case revisit time of three hours at the equator. An important aspect of GPM is the use of a highly capable "core observatory" (similar to TRMM) to provide rainfall classification and rain rate retrievals. This will be augmented by six or more less-capable "constellation" satellites carrying microwave radiometers, which are cross-calibrated to the core observatory, and provide the rapid temporal sampling of rainfall. Thus, in the future, scientists and operational users will have to learn to accommodate rain retrievals of varying quality in their research and applications.

In September 1999, the QuikSCAT Radiometer (QRad) began ocean precipitation measurements, which provides additional independent samples over SSM/I and TMI. A typical example of the QRad sampling is shown in Figure 13 for a three-hour window (universal time: 00:00 - 03:00). Also shown are the corresponding sampling coverage for TMI and three SSM/I's. It is observed that QRad increases the coverage area by about 10%; but even with five microwave imagers, the ocean sampling is still only approximately 60% in a typical 3-hour window.

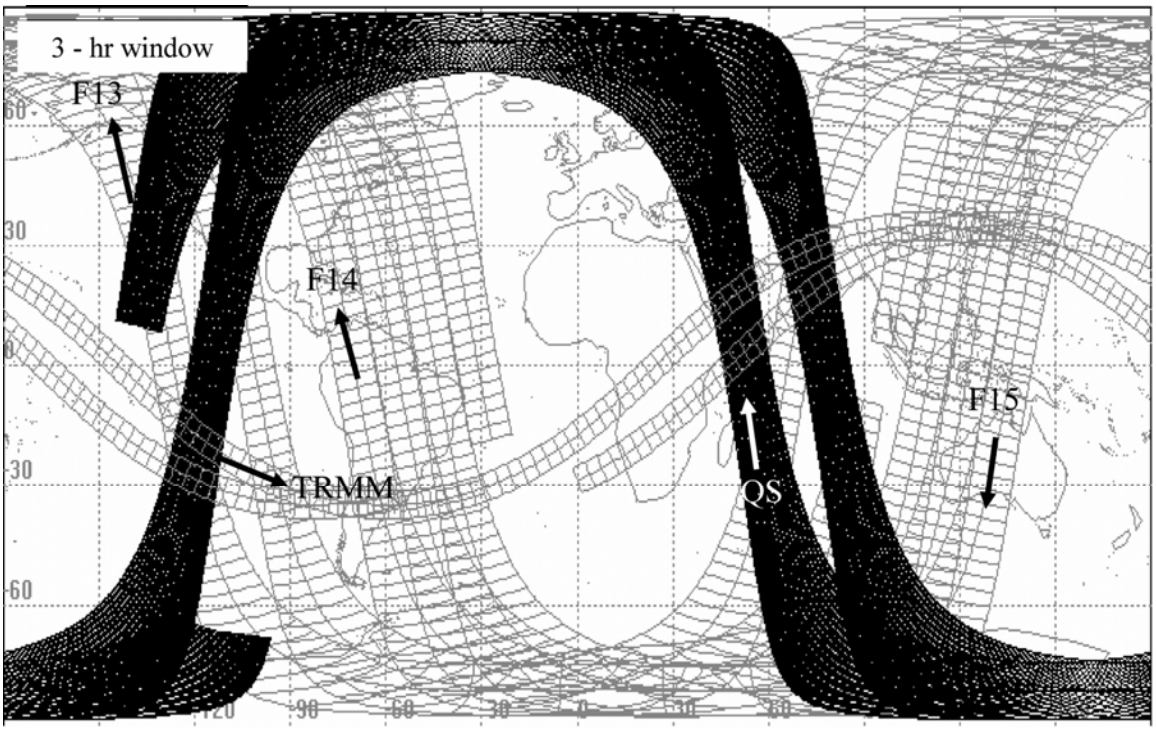

Figure 13: Three hour sampling provided by 3-SSMI's (F-13, F-14 & F-15), TRMM Microwave Imager and QuikSCAT Radiometer swaths for time window, 0 – 3 hours Zulu, on March 1, 2000.

Never the less, the QRad's sampling contribution is significant in that the daily average revisit time is reduced as shown in Figure 14. For clarity of presentation, sampling improvements, due to the QRad and averaged over 20º latitudinal zones, are quantitatively summarized in Table 3. Further, an additional illustration of QRad oceanic sampling contribution is shown in Figure 15 which presents a typical scenario of "local time of day" QRad sampling over a 1°x 1° box located at equator and prime meridian for a period of one month. Also shown are the local time samplings for TMI and three SSM/I instruments. It is clear that QRad is providing independent sampling which complements and fills in the gaps between the sampling times of the other satellites. Thus, the QRad time series (from September 1999 to present) is a valuable addition to the ocean

precipitation climate data set. Further, the early availability of QRad rain measurements provides an excellent opportunity for learning how to utilize future GPM data sets. As will be described, even though the quality of the QRad rain retrievals are somewhat limited compared to TMI and SSM/I, they certainly are useful in that they provide additional temporal / spatial sampling.

Moreover, the QRad rain estimates provide simultaneous, collocated precipitation measurements with QuikSCAT ocean surface wind vectors for rain-flagging contaminated wind vector retrievals. In the following section, the statistical inversion passive QRad rain rate algorithm is presented. The description given is also applicable to SeaWinds on ADEOS-II Radiometer (SRad) rain retrieval algorithm.

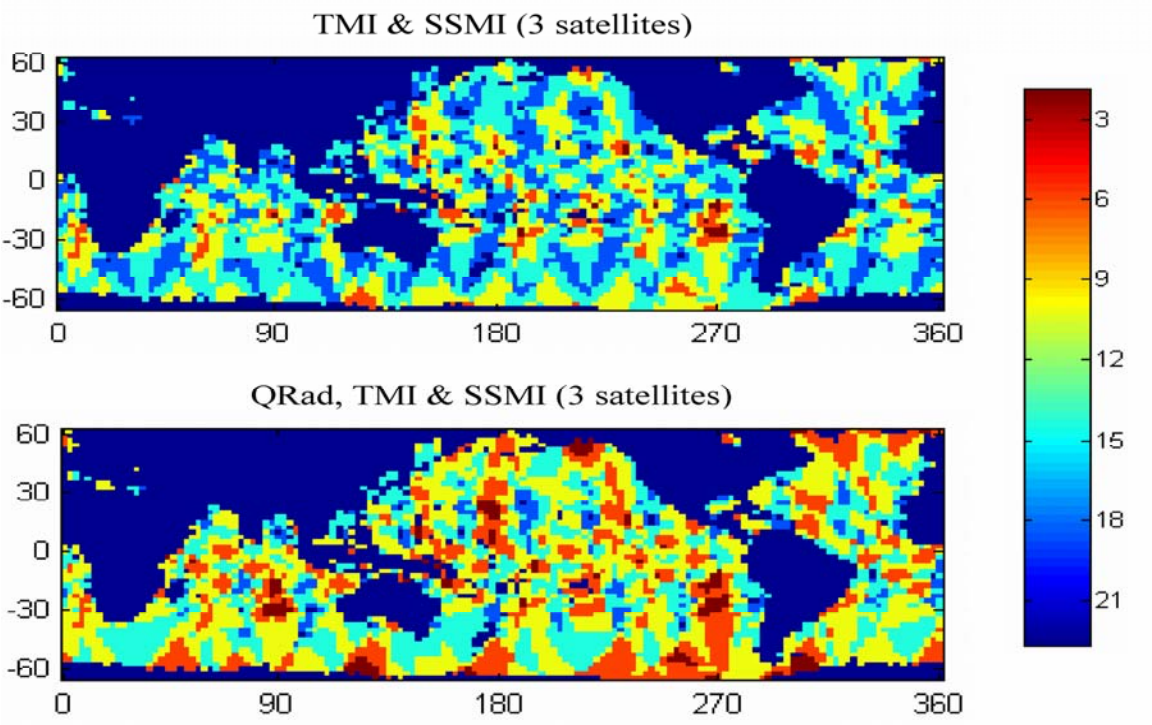

Figure 14: Ocean sampling, daily average revisit time. Upper panel is TMI and 3-SSMI's and lower panel is sampling with QRad added

Table 3: Average oceanic coverage in a typical 3-hour window. Improvements due to QRad contribution are calculated for regions of 20º latitudinal zones

Region	Ocean Coverage without QRad	Ocean Coverage with QRad	QRad Contribution
40ºN - 60ºN	57.94 %	68.55 %	10.61 %
20ºN - 40ºN	58.23 %	64.69 %	6.46 %
0º - 20ºN	63.70 %	71.34 %	7.64 %
20ºS - 0º	63.13 %	70.17 %	7.04 %
40ºS - 20ºS	57.69 %	63.87 %	6.18 %
60ºS - 40ºS	58.34 %	68.26 %	9.93 %

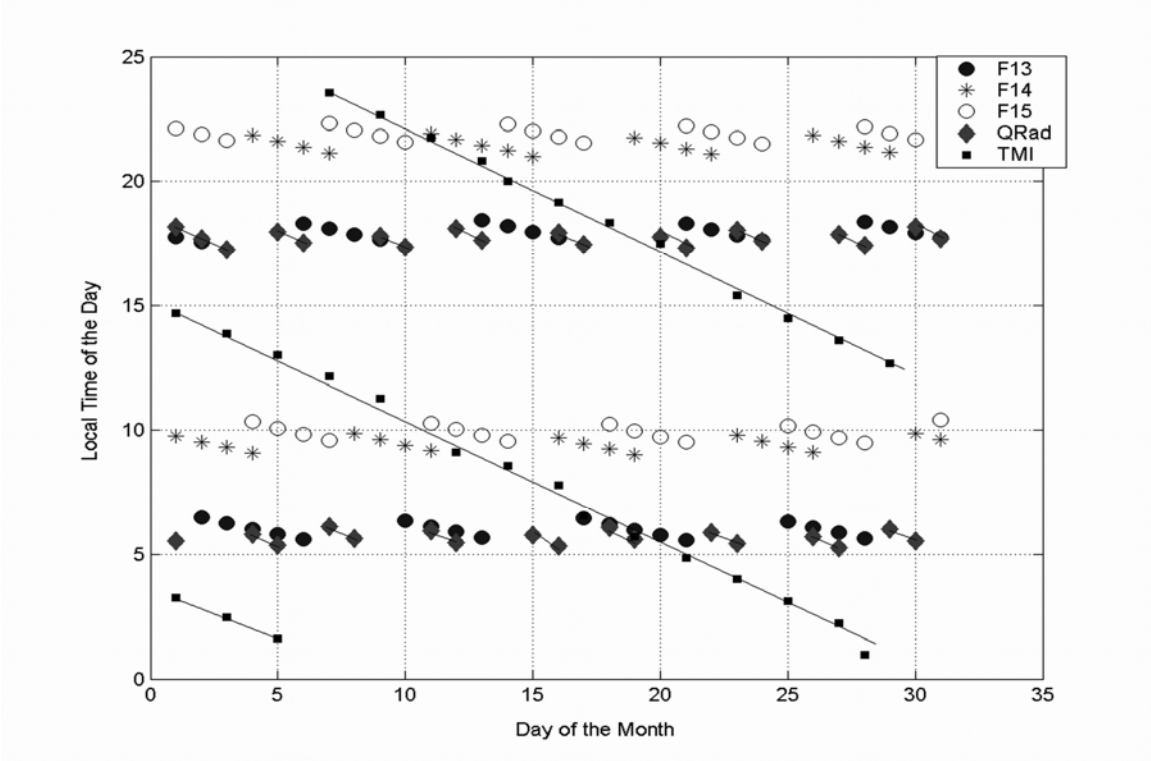

Figure 15: Typical time of day sampling for SSM/I (F-13, F-14 and F-15), TMI and QuikSCAT Radiometer (QRad). Sample location is 1°x 1° latitude / longitude box located at equator and prime meridian.

QRad Passive Integrated Rain Rate Algorithm

The QRad (henceforth, by implication, SRad) rain rate algorithm is a statistical based retrieval that uses an empirical passive brightness temperature - rain rate (T_B-R) relationship to derive the integrated rain rate over the oceans [40]. Because the measured ocean brightness temperature is directly proportional to the path integrated rain rate, this is the chosen retrieved geophysical parameter. To calculate the average rain rate measured in mm/hr requires knowledge of the rain path length. Users may convert QRad integrated rain rate to surface rain rate by dividing by this rain path length that is equal to the height of the rain times the secant of the incidence angle. The QRad T_B-R relationship was derived using a data set of rain events that were near-simultaneously observed by QRad and the TMI. In order to get a valid observation of the precipitation conditions affecting the QRad T_B measurements, the collocation time difference for a given event is restricted to be less than ±30 minutes compared to the TMI observation. A simplified algorithm block diagram is presented in Figure 16. The data inputs are:

1. The QRad T_B's from the QuikSCAT level 2A (L2A) and the collocated numerical weather prediction (NWP) wind fields from the National Centers for Environmental Prediction (NCEP) which are obtained from the QuikSCAT level 2B (L2B) data products available at (http://podaac.jpl.nasa.gov/quikscat/).
2. A priori information in the form of monthly-tabulated ocean background brightness temperatures.

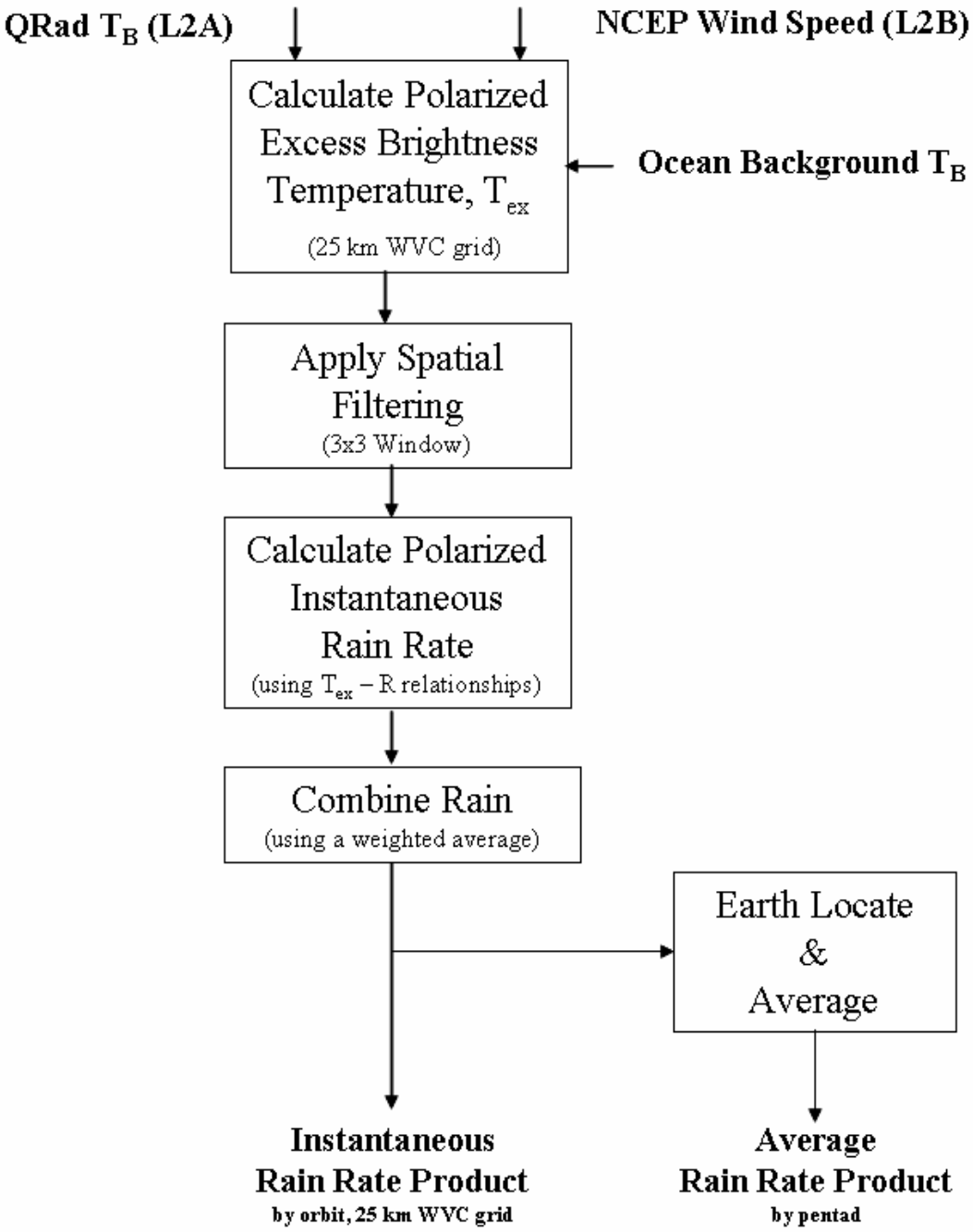

Figure 16: A simplified QRad rain rate algorithm block diagram.

The individual polarized L2A QRad T_B's, and the collocated L2B NCEP wind speed products are provided on a spacecraft measurement grid of wind vector cells at 25 km resolution. These two products are used with the ocean background to calculate the excess brightness (T_{ex}) upon which the rain retrieval is based. The passive QRad rain algorithm outputs an instantaneous rain rate product, by orbit revolution, at 25-km resolution wind vector cell (WVC) measurement grid. Further, the algorithm can output a five-day (pentad) rain rate average on a 0.25° x 0.25° Earth-located latitude / longitude grid. Both products are binned in 0.5 hour universal time windows. Next, the further details of the QRad rain algorithm will be presented.

TRMM Training Data Products

The QRad rain rate algorithm was trained using a data set of four hundred twenty one significant rain events that were observed within ± 0.5 hrs with TMI. The importance of such simultaneous observation is driven by the fact that the spatial structure and intensity of a typical rain event can rapidly vary with time, thereby, a close collocation time difference is essential in order to have a valid observation of the precipitation conditions affecting the QRad T_B measurement. The collocated rain events are chosen from different seasons of the year 2000, having locations that span the full latitudinal range of the tropical rainfall region as shown in Figure 17.

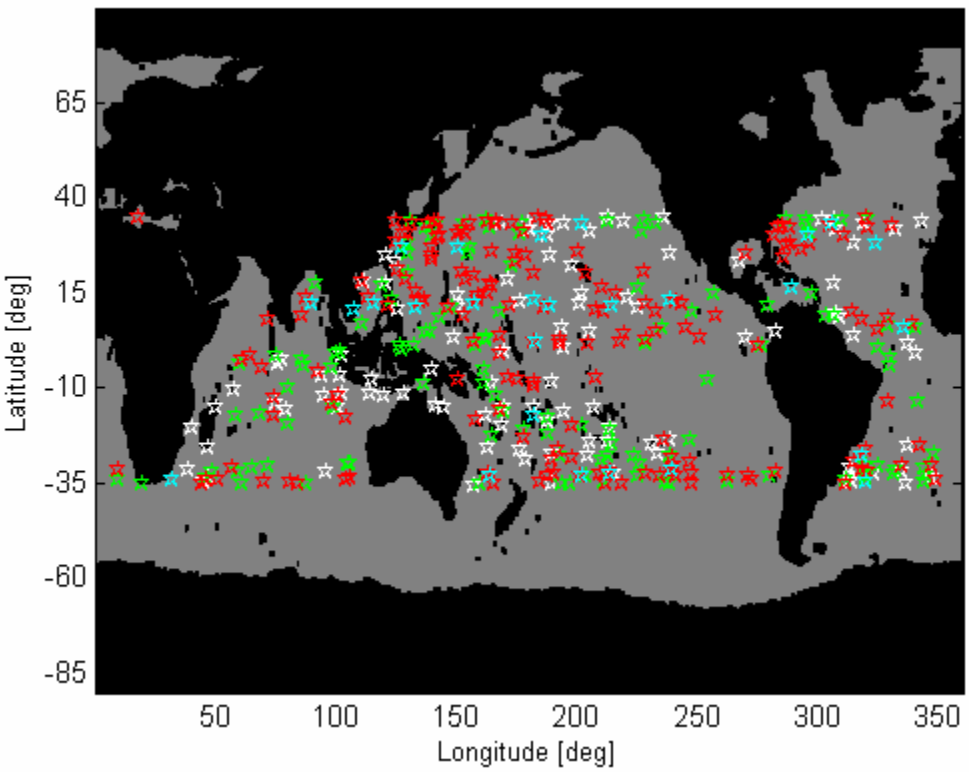

Figure 17: Locations of simultaneous collocated rain events for 421 QRad / TRMM training data set. Collocation time difference is restricted to ±30 minutes.

In the QRad algorithm development activity, we use the following TRMM products available through the TRMM Science Data and Information System (TSDIS) (http://tsdis.gsfc.nasa.gov):

1. 2A12 product, TMI derived surface rain rate over oceans.
2. 3A11 product, TMI derived monthly freezing level over oceans.

We use the TRMM 2A12 product to provide surface rainfall rate to train the QRad rain algorithm. The 2A12 algorithm retrieves precipitation based upon nine channels of TMI brightness temperature [28]. This algorithm uses a Bayesian approach that utilizes cloud resolving models to generate a large database of potential hydrometeor

profiles and a microwave radiative transfer model to compute the corresponding TMI channel brightness temperatures. This algorithm generates vertical hydrometeor profiles on a pixel basis. For each pixel, cloud liquid water, precipitation water, cloud ice water, precipitation ice, and the latent heating are given at 14 vertical layers. The surface rainfall and associated confidence are also computed.

We use the TRMM 3A11 product to estimate the height of the rain over the ocean for use in the QRad algorithm. The TMI 3A11 algorithm [25] also uses the TMI brightness temperatures to infer the freezing level, which is the estimated height of 0°C isotherm over oceans in 5° x 5° boxes for one month. It also produces 5° x 5° monthly oceanic rainfall maps using TMI Level-1 brightness temperatures.

Passive Excess Brightness Temperature (T_{ex}) Model

Due to their low emissivity; ocean surfaces appear as relatively uniform cold T_B backgrounds at low frequency satellite microwave radiometer observations. The presence of rain in the atmosphere tends to absorb and re-emit microwave radiation, and as a result, the oceanic microwave brightness temperature when viewed through a raining atmosphere is greater than that when viewed through a clear atmosphere. Rain can be inferred from the differential (excess) part between the raining and clear ocean T_B; so the extraction of the rain signal depends directly upon the knowledge of the ocean brightness when viewed through an intervening atmosphere without rain.

The brightness temperature observed by the satellite microwave radiometer is determined by the electromagnetic frequency, polarization, incidence angle and by a number of atmospheric geophysical variable profiles including temperature, oxygen density, water density (vapor, cloud liquid and rain) as well as the ocean surface geophysical variables: sea surface temperature, salinity and surface wind speed. The usual remote sensing scenario is for the observing microwave radiometer to have the number of independent measurements greater than the number of unknown geophysical parameters. For example, according to Wentz and Spencer [41], they use 7 SSM/I channels to retrieve 4 parameters; surface wind speed, integrated water vapor, integrated cloud liquid water and path average rain rate. Parameters that contribute significantly to the brightness but are not retrieved are known a priori, frequently from climatology or numerical models.

Mears et al. [42] have characterized the monthly mean ocean T_B for the QRad channels using seven years of measurements from the SSM/I. This ocean brightness temperature climatology accounts for all of the geophysical parameters except the transient effects of rain and surface winds (which have been removed in the data analysis). Fortunately, the Ku-band (13.4 GHz) T_B responds weakly to the atmospheric and surface geophysical parameters included in this climatological background. Further, all of these parameters vary slowly in space and time (seasonally). As an example, the dynamic range of the horizontally polarized ocean background temperature with latitude for the month of March is (91 K ~ 103 K), while the vertically polarized ocean background temperature for the same month lies in the range (165 K ~ 182 K). In both cases, the longitude variations are almost flat.

On the other hand, rain and wind are very transient with weather systems, and they need to be retrieved simultaneously. Because there are only two QRad channels (V- and H-pol), we use the ocean (and atmosphere) brightness climatology as a priori information in conjunction with collocated Numerical Weather Prediction (NWP) wind speed measurements from the National Centers for Environmental Prediction (NCEP). We define the rain contribution to the measured brightness temperature as the "excess brightness" (T_{ex}) which is equal to the residual of the average measured QRad T_B after subtracting ocean background brightness temperature (which includes non-raining atmosphere) and the brightness temperature due to the surface wind speed. Thus, the polarized T_{ex} is:

$$T_{ex-p} = T_{B\,QRad-p} - T_{B\,Ocean-p} - T_{B\,W.speed-p} \tag{4.1}$$

where

$$T_{BQRad} = \frac{1}{n}\sum_{i=1}^{n} T_{Bi}\text{, is the average measured QRad } T_B\text{, K.} \tag{4.2}$$

n	number of pulses within a Wind Vector Cell (WVC).
$T_{B\,Ocean}$	ocean background T_B, K. (includes atmosphere without rain)
$T_{B\,W.speed}$	T_B due to the wind speed, K.
p	polarization.

The ocean background is interpolated to the day of the observation using monthly latitude / longitude tables at 0.25° spatial resolution. The NCEP ocean surface wind speeds are obtained from QuikSCAT L2B data files [43]. They are used in our analysis to provide an estimate of the wind induced brightness contribution ($T_{B\ Wspeed}$) to the QRad brightness temperature measurement. The NCEP winds are interpolated from 2.5º global latitude / longitude grid to the SeaWinds WVC locations. It is commonly known in literature that the 1000 mbar NCEP wind speeds are somewhat biased high compared to the 10 m neutral stability wind measured by SeaWinds. To adjust for the bias, a multiplicative constant is determined using linear regression analysis over rain free (as verified by TMI) QuikSCAT / NCEP collocated winds. The bias correction constant is determined as

$$ws_{QuikSCAT} = 0.84 \times ws_{NCEP} \tag{4.3}$$

In order to derive an estimate for the wind speed contribution ($T_{B\ Wspeed}$) in Equation (4.1), we use background corrected QRad T_B measurements along with collocated, bias-adjusted NCEP wind data over rain free scenarios (as verified by TMI observations). Next, the collocated data are bin averaged by NCEP winds in 0.5 m/s steps to estimate a first order brightness correction using least squares analysis

$$T_{BW.speed-p} = a_{0p} + a_{1p} \cdot wspd \tag{4.4}$$

where

a_{ip} are empirical wind speed coefficients (p = V-pol & H-pol) given in Table 4.

wspd is the collocated, bias adjusted NCEP ocean surface wind speed, m/s

The derived first order brightness temperature corrections (H-pol & V-pol) due to the surface wind speed are depicted in Figure 18. Typical values for the polarized brightness temperature ($T_{B\ Wspeed}$) due to a wind speed measurement of 8 m/s are 4.82 K for the H-pol, and 1.42 K for the V-pol.

Passive Excess Brightness - Integrated Rain Rate Relationship

The passive QRad rain rate algorithm is a statistical based retrieval that uses an empirical brightness temperature - rain rate (T_B-R) relationship. This relationship is derived using a QRad brightness temperature and TMI integrated rain rate data set from four hundred and twenty one significant rain events that are observed within ± 0.5 hrs. In the propagation direction, the total atmospheric absorption and emission of microwave energy is directly proportional to the rain path length; thus, the observed rain brightness temperature is proportional to the integrated rain rate.

The T_B-R relationship is calculated using a regression analysis of the QRad excess brightness (T_{ex}) with the corresponding collocated TMI integrated rain rate (IRR). First,

the polarized QRad T_{ex} are produced on a 25 km WVC measurement grid using Equation (4.1). As noted previously, since the SeaWinds instrument design was optimized as radar, QRad is not a high performance radiometer. While typical radiometers have bandwidths of 100's MHz, QRad has a limited receiver bandwidth of about 750 KHz, which results in a poor radiometric precision ΔT ~25 Kelvin per pulse. Therefore, the polarized QRad T_{ex} measurements are smoothed using a weighted 3x3 spatial averaging filter to reduce the unwanted random noise component of the measurement, thereby, improve the effective radiometric precision (ΔT) of the measurements.

Next, the TMI 2A12 surface rain rates are converted to IRR and collocated with the corresponding QRad WVCs that included the center of the TMI measurement. Because the TMI integrated rain rate value is not available in 2A12, the IRR is approximated to be the product of the TMI surface rain rate (mm/hr) and the rain path length (km). For this calculation, we use the TMI retrieved freezing level (TMI 3A11 product) as the rain height interpolated to the corresponding QRad WVC locations and multiply by the secant of the TMI incident angle (52.8°). As an example, a typical average value for rain height near the equator during the month of March 2000 is about 4.9 km.

Finally, the WVC collocated data are binned by TMI IRR, averaged and then used in a least-squares curve fit procedure to determine an optimal 3rd order polynomial. This polynomial is forced to pass through the origin producing a zero rain estimate in response to a null T_{ex} measurement. The estimated coefficients are provided in Table 5, and the resulting transfer functions for SeaWinds twin beams are depicted in Figure 19.

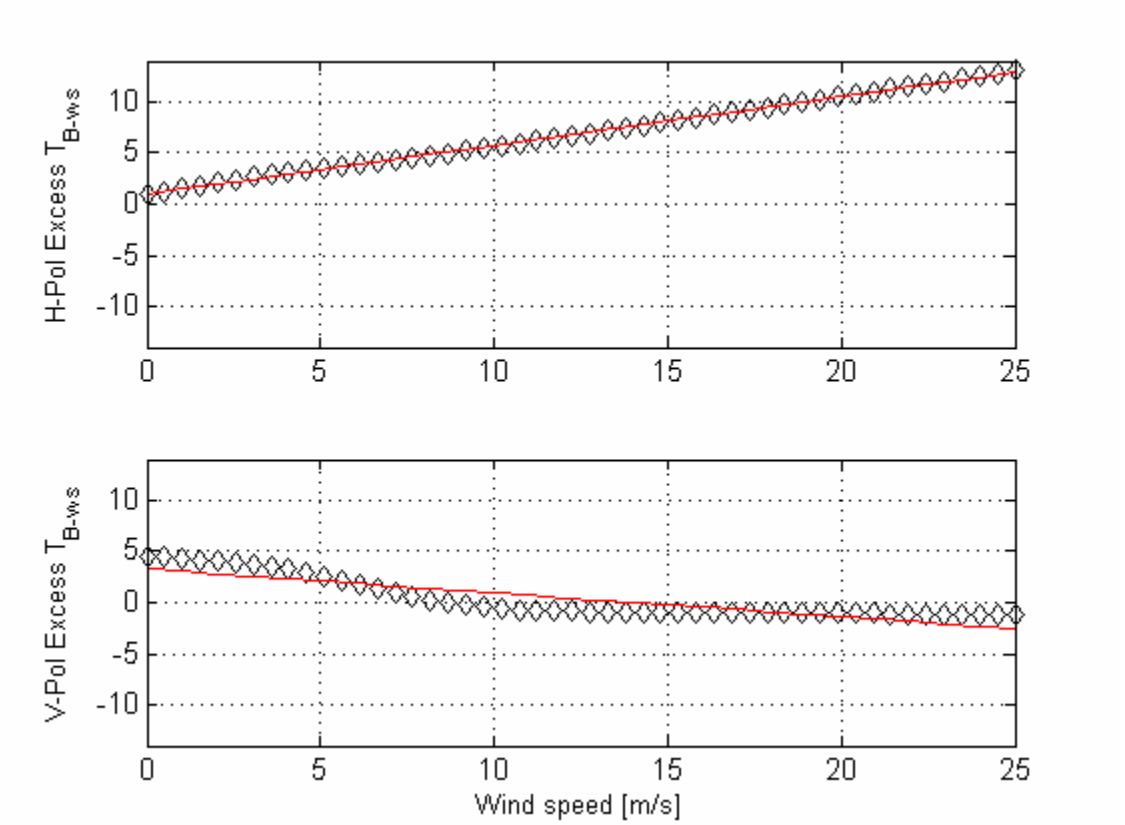

Figure 18: QRad brightness temperature correction due to surface wind speed. Upper panel depicts the correction applied to the H-pol inner beam, and the lower panel shows the correction for the outer V-pol beam. Diamonds denote binned / averaged data.

Table 4: Regression coefficients for empirical excess brightness temperature - wind speed relationship

	b_0	b_1
H-pol	1.0156	0.4752
V-pol	3.2834	-0.2332

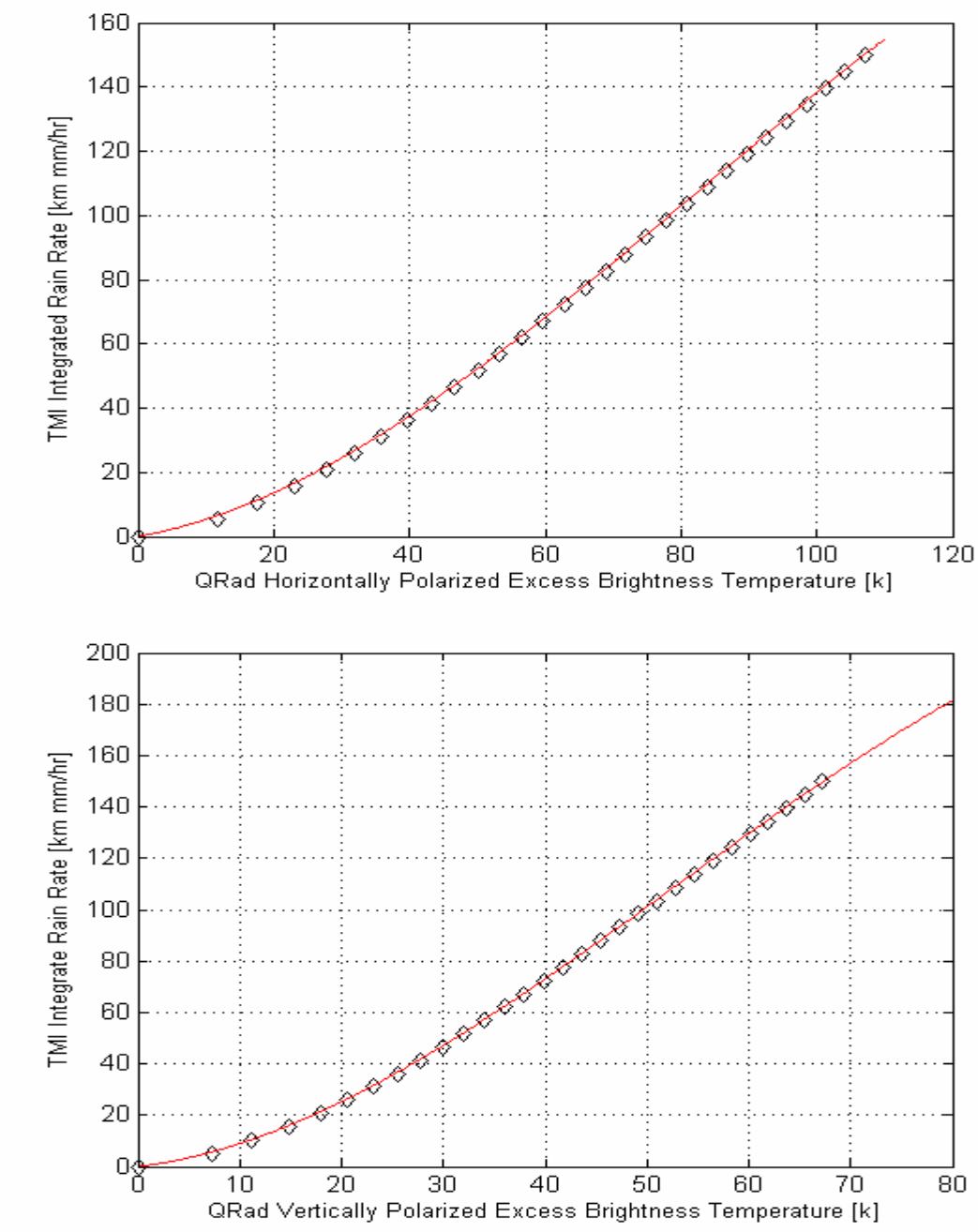

Figure 19: QRad (T_{ex} – R) 3rd order transfer function for H- pol (upper panel) and for V-pol (lower panel). Diamonds denote binned / averaged data.

Table 5: Passive integrated rain rate - excess brightness temperature regression coefficients.

	b_0	b_1	b_2	b_3
H-pol	0	0.3649	0.0169	-0.0001
V-pol	0	0.4643	0.0455	-0.0003

QRad Integrated Rain Rate

The integrated rain rate is calculated from the polarized T_{ex} using the T_B-R relationship given as:

$$IRR_p = b_{0p} + b_{1p} * Tex_p + b_{2p} * Tex_p^{\,2} + b_{3p} * Tex_p^{\,3} \qquad (4.5)$$

where

b_i regression coefficients, given in Table 5.

The final QRad rain rate product is a weighted-average of the polarized rain rates. The usual procedure is to weight measurements by their inverse variances; but for QRad, the variances for V- and H-pol are somewhat similar. Due to their higher sensitivity to the presence of rain, the QRad H-pol T_{ex} measurements are known to have a relatively wider dynamic range compared to their V-pol counterparts. This can be explained by the fact that the H-pol EM radiance is more sensitive to rain drops since those drops tend to flatten into oblique spheroids as they fall toward the surface.

In addition to the H-pol and V-pol weighting factors, the QRad algorithm has provisions for fine tuning against TMI rain measurements in the form of a linear slope and offset coefficients. Hence, the final QRad rain rate product (km*mm/hr) has the following form:

$$IRR_{QRad} = c_0 + c_1\left(\alpha \cdot IRR_h + \beta \cdot IRR_v\right) \tag{4.6}$$

Where:

α, β are empirically derived H-pol / V-pol weighting factors expressed as percentages with values of 0.86 and 0.14, respectively.

c_1, c_o are empirically derived slope and offset calibration to adjust the resulting QRad IRR to match the TMI IRR for the training data set. In the current version of the algorithm, c_o and c_1 have values of approximately zero and unity respectively. In order to determine the values of different calibration parameters: c_0, c_1, α, β in Equation (4.6), a numerical optimization routine is utilized to minimize the mean square error (MSE) between the TMI IRR and the resulting QRad IRR over the algorithm training data set.

By inverting the (T_B – R) transfer functions given by Equation (4.5), and utilizing the empirical wind induced brightness temperature relationship of Equation (4.4), the total polarized excess brightness (above background T_B) observed by QRad is simulated and shown in Figure 20 as a function of the integrated rain rate and surface wind speed. Also shown on the figure (in solid red) is the locus of the total excess T_B points where the rain induced contribution is equal to 50 % of the simulated total polarized excess T_B measurement. It can be readily seen from the figure that under most rain / wind

combinations, the T_B response of QRad twin beams is mainly rain dominated. For example, as the upper panel of Figure 20 illustrates, once the rain rate exceeds the threshold of 15 km* mm/hr, the rain induced excess T_B contribution observed by QRad inner H-pol beam is more than 50 % of the total measured excess T_B regardless of the brightness contribution due to the wind speed blowing over the ocean surface.

A quantitative comparison between the QRad and TMI IRR's for the four hundred and twenty one rain events is presented as a scatter diagram in Figure 21. As the figure depicts, the derived QRad IRR's have a considerable scatter especially at the higher rain rates, which is mainly attributed to the coarse QRad (ΔT) measurement, however, the QRad IRR's are well behaved in the mean compared to TMI. This can be verified by smoothing the scatter diagram in steps of 5 km mm/hr (~ 0.6 mm/hr) shown as blue diamonds on the figure. This may be also verified by examining in the statistics of differences (QRad minus TMI) presented in Table 6. For this comparison, we use the same data as Figure 21; but now we bin the data in six ranges of TMI IRR. The mean of the individual histograms is near zero, that verifies the T_B-R least mean squares regression procedure; however the standard deviations are large as a result of the poor QRad ΔT.

Additional quantitative comparisons between TMI and QRad for the four hundred and twenty one rain events are presented in terms of the IRR probability density functions (pdf's) and cumulative distribution functions (cdf's) shown in Figures 22 and 23, respectively. The large ΔT causes some distortion in the QRad pdf especially for high IRR; however, this does not produce a significant accumulation error as seen by examining the QRad cdf.

Since the QRad rain rate algorithm is applicable only over the ocean, we use a conservative land mask with extended land boundaries (and small islands deleted) to determine where the rain rate algorithm is applied. Unfortunately, when QRad measurements are close to land, the measured T_B is also affected by the "hot" radiance from land that enters through the antenna pattern side-lobes. Thus, within about 150 km of land, the measured QRad T_B has a land bias of about +5 to +10 K. To compensate for this effect, the background brightness temperature over the land is set to its typical value of 270K, and the ocean/land background is smoothed using a 3 x 3 pixel window to eliminate the effect of the sharp land-ocean boundary. In this way, the ocean brightness temperature near the boundary is elevated in an attempt to remove the influence of land on measured T_{ex}. The final step is to evaluate the monthly rain rate at all land/water boundaries and identify anomalous negative rain rates, when ocean background is too high; and positive rain rates, when ocean background is too low. The final land mask is subjectively adjusted to remove these anomalous rain rates that may result along the land borders.

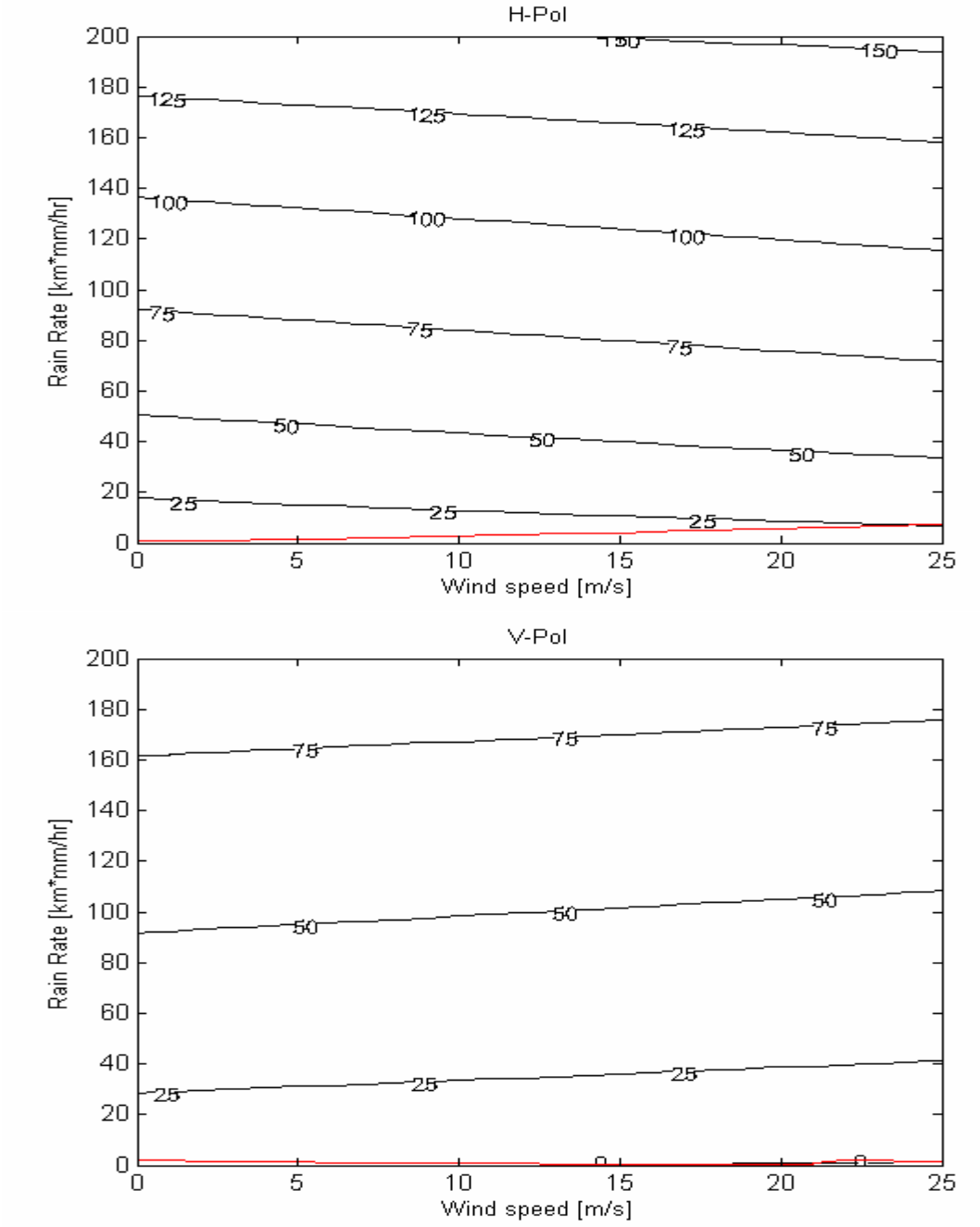

Figure 20: Contour plots of simulated total excess TB measurements observed by QRad inner H-pol beam (upper panel) and the outer V-pol beam (lower panel) as a function of the integrated rain rate and wind speed.

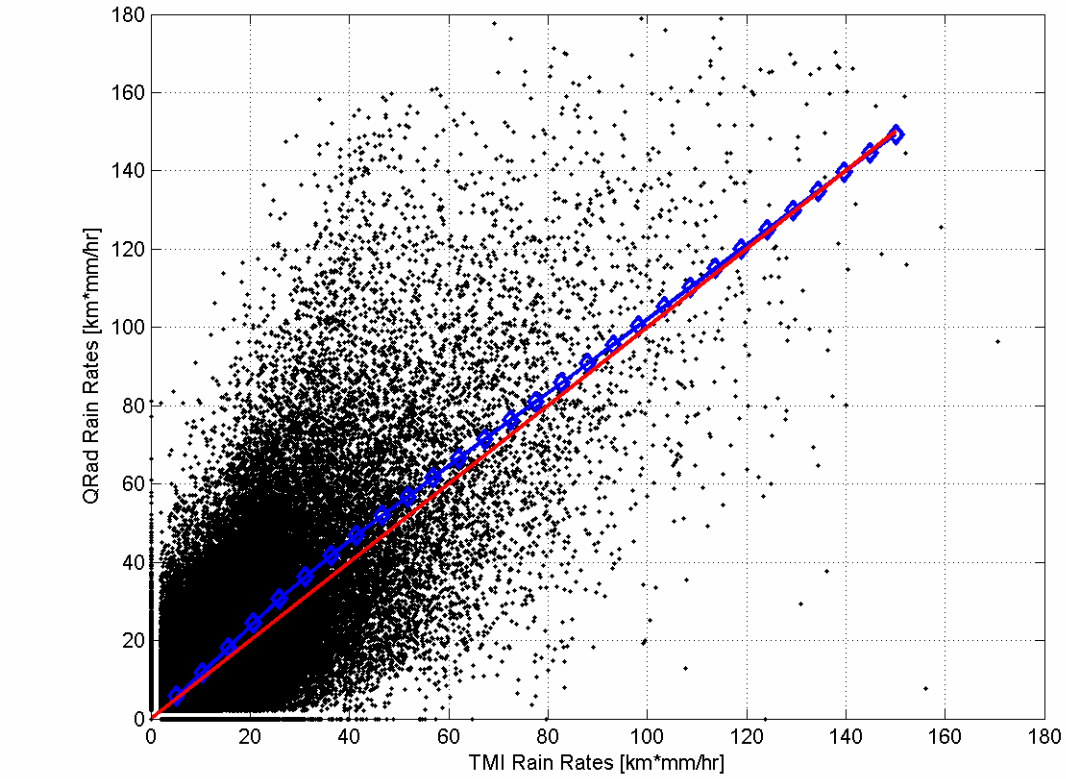

Figure 21: Instantaneous integrated rain rate comparisons for four hundred twenty one collocated rain events for QRad and TMI. Spatial resolution is 0.25° (25 km).

Table 6: Instantaneous integrated rain rate (km*mm/hr) differences for six TMI ranges. For each range, the difference (QRad minus TMI) is calculated.

TMI Range	Number of points	Difference mean	Difference std	Difference rms/<TMI>
0 – 4	112190	0.8780	3.2018	2.9465
4 – 8	28366	0.4222	6.5841	1.1430
8 – 12	15798	0.3413	8.9964	0.9136
12 – 24	24081	1.2614	14.1051	0.8317
24 – 32	7220	1.0704	20.9018	0.7581
> 32	11522	-1.3409	30.3480	0.5955

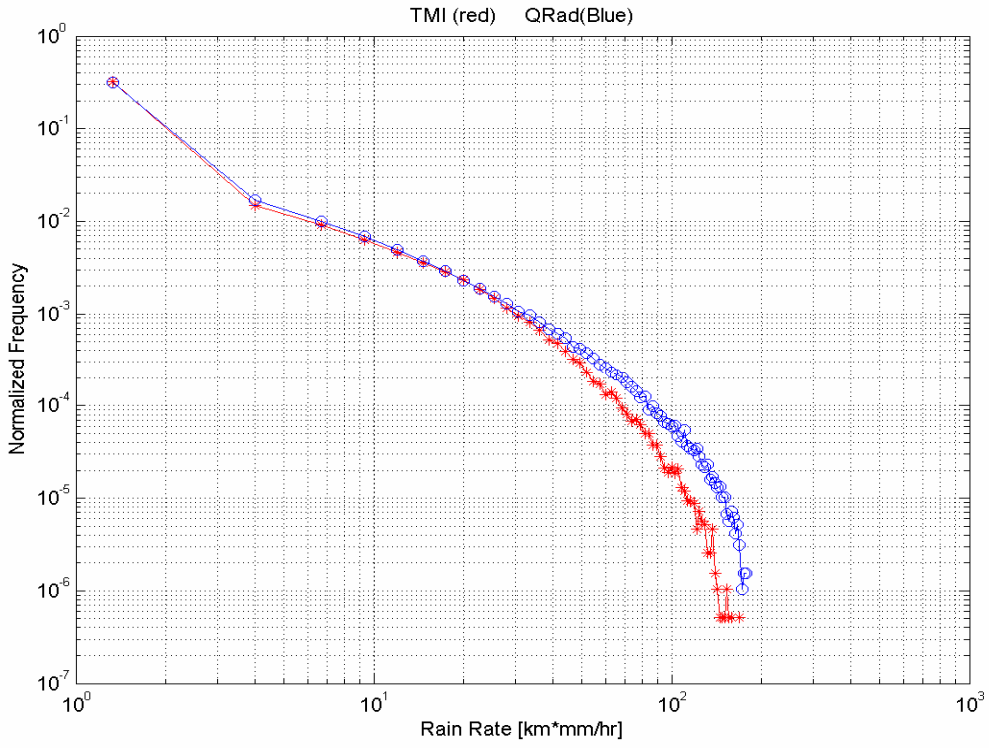

Figure 22: Probability density function for integrated rain rate at four hundred twenty one collocated rain events for QRad and TMI.

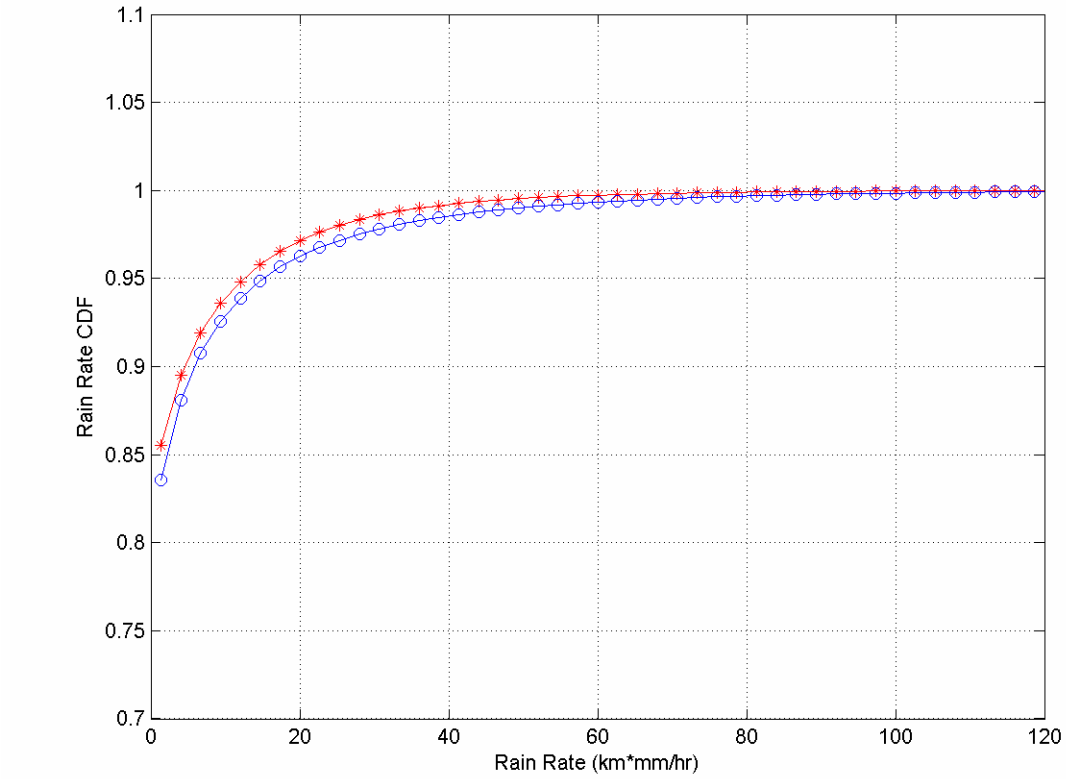

Figure 23: Cumulative distribution function for integrated rain rate at four hundred twenty one collocated rain events for QRad and TMI.

.

CHAPTER FIVE: VALIDATION OF PASSIVE QRAD RAIN ALGORITHM

Introduction

In this chapter we evaluate the performance of the passive QRad rain rate retrieval algorithm. The evaluation activity is performed through comparisons with independent rain measurements from the TMI 2A12 surface rain rates, and the TRMM 3B42RT composite microwave and visible / infrared near-real time data product. Results demonstrate that QRad rain rate measurements are in good agreement with these independent microwave rain observations and superior to the visible / infrared rain estimates.

Therefore, the QRad rain measurement time series (from 1999 till present) is a valuable addition to the oceanic precipitation climatology that can be used to improve the diurnal estimation of the global rainfall, which is a goal for NASA's future Global Precipitation Mission (GPM) program. Moreover, the availability of QRad data will provide GPM users early access to learn to use less-precise rain measurements that will occur in the GPM era with the use of less-capable constellation satellites. The QRad rain algorithm has been implemented in JPL level 2B (L2B) science data product as part of QuikSCAT winds data reprocessing to improve the rain flagging of rain-contaminated oceanic wind vector retrievals.

Validation Data Products

TMI, an improved design of the SSM/I instrument, is dedicated to obtaining quantitative measurements of rainfall. The oceanic instantaneous rain rate, measured by the TMI is widely accepted by the science community to be the best estimate of the true rain rate available from a passive microwave sensor. Thus, to evaluate the QRad retrieved rain rate capabilities, we use the TRMM 2A12 instantaneous surface rain rate and the TRMM 3B42RT surface rain rates for the comparison data set. The TMI 2A12 instantaneous rain rate product has been validated by the TRMM science team through numerous comparisons with other independent rain measurements [44]. The TRMM 3B42RT data product [45] available from (ftp://aeolus.nascom.nasa.gov/pub/merged) combines precipitation estimates in global 3 hour universal time windows (± 90 minute span around synoptic observation hours 00 UTC, 03 UTC, 06 UTC, …, 21UTC). These estimates are derived from all available high quality (HQ) microwave sources from low earth orbits (three SSM/I's and TMI) combined with visible and infrared rain rate (VAR) estimates derived from geostationary visible / infrared observations. For each 0.25° grid point the HQ rain rate estimate is used, if available; otherwise the VAR value is used. The 3-hour temporal resolution is driven by the need for the HQ to accumulate a reasonable sample without encompassing a large fraction of the diurnal cycle. The TRMM 3B42RT is based on the Goddard Profiling Algorithm (GPROF) [28, 46]. GPROF is a multi-channel physical approach for retrieving rainfall and vertical structure information from passive microwave satellite observations. It applies a Bayesian inversion method to the observed microwave brightness temperatures using an extensive

library of cloud model based relations between hydrometeor profiles and microwave brightness temperatures. Each hydrometeor profile is associated with a surface precipitation rate. GPROF includes a procedure that accounts for inhomogeneities of the rainfall within the satellite field of view. The GPROF-SSM/I estimates are computed from the SSM/I satellite data records (SDRs), while the GPROF-TMI estimates are computed by TSDIS as 2A12RT. The GPROF-SSM/I estimates are calibrated and probability matched to 2A12RT. The VAR infrared precipitation estimate are HQ-calibrated locally in time and space. The TRMM 3B42RT rain rates are adjusted to remove bias via histogram matching. Here, we use rain estimates from the TRMM 3B42RT high quality (HQ) microwave sources as the rain "surface truth" for the QRad validation activity.

Also, we use SSM/I rain products provided by Remote Sensing Systems (http://www.remss.com) for quantitative comparisons with the average QRad rain product. SSM/I rain products have been validated against independent rain measurements as reported by [41]. Next, we present subjective evaluations for the two QRad precipitation data products.

Instantaneous Rain Rates

A typical instantaneous rain image example is given in Figure 24. The upper panel shows the TMI / QRad near-simultaneous overlapping swaths. Both satellites were

in descending revs and observed the rain event within ~ 20 minute pass time difference. The corresponding rain images are given in the lower panel. For clarity of presentation, both rain images were resampled to 0.125° resolution. The color bar on the right side indicates the rain rate values (mm/hr); and both rain images have identical color scales for retrieved rain rates. The shape and intensity of the rain event were well captured by QRad. In fact, the correlation coefficient for the two images is found to be 89.7%.

Another instantaneous rain image comparison between QRad and the TMI 2A12 surface rain product is presented in Figure 25. The rain event was observed on April 19 2003 within 10 minutes of the TRMM overpass. The upper left panel shows the TMI integrated rain rate, and the corresponding QRad rain estimate is given in the upper right panel. The pixel resolution is 25 km on a WVC measurement grid. Color scales are identical for both images and proportional to the integrated rain rates in (km*mm/hr). To reduce the possible occurrence of false rainy pixels resulting from the noisy QRad (ΔT), we apply a threshold of 2 km*mm/hr on both integrated rain values (equivalent to ~ 0.25 mm/hr). This threshold is empirically derived to optimize the spatial rain patterns as observed by QRad (compared to TMI) over the collocated training data set. It is observed that the shape and the relative intensity of the rain are well captured by QRad. For this particular event, the correlation coefficient is found to be 90%.

In order to quantify the performance of QRad measurements as a stand alone flag for identifying the rain contaminated wind vector retrievals, we produce binary maps that are quantized into four levels to classify the rain pattern for the given collocated rain event, as shown in the lower panel of Figure 25. Using the TMI binary rain image as the surface truth, we classify the pixels of the binary rain image into three categories: the first

is agreement percentage, which is the percentage of pixels that are simultaneously identified by both sensors (QRad and TMI) as raining pixels or non raining pixels. The second category is the false alarm percentage, which is the percentage of pixels classified as raining pixels by QRad, while identified as non raining pixels by TMI. The third category defined as miss-rain percentage is the percentage of pixels classified as raining pixels by TMI, while QRad identified those pixels as rain free. The different percentages of the rain pattern classification are calculated for the event under consideration, and found to be as follows: the agreement percentage = 92.89%, false alarm percentage = 4.46%, and miss-rain percentage = 2.65%. These results emphasize the utility of QRad rain measurements as a powerful stand-alone rain flag.

Additional evaluations of the instantaneous QRad retrieval algorithm consisted of comparisons with the high quality merged TRMM 3B42RT real time multi-satellite precipitation data product. A hundred and eight significant rain events that were observed by QRad and HQ microwave radiometers are used as an additional independent data set for this validation activity. Overall the rain intensity and spatial rain patterns were well captured by QRad and the correlation coefficients between corresponding rain images was typically > 70%.

The first quantitative comparison for these hundred and eight rain events is presented as a scatter plot in Figure 26. Statistical results of the differences (QRad minus HQ) are presented in Table 7, where we bin the data in five ranges of HQ rain rate. Although the standard deviations for the individual bins are large due to the poor QRad ΔT, the retrievals are well behaved in the mean.

The second quantitative comparison for the hundred and eight rain events is presented in terms of the rain rate probability density functions (pdf's) shown in Figure 27. Clearly, the large ΔT causes some distortion in QRad pdf for low rain rate values; however, for larger rain rates > 2.5 mm/hr, the QRad pdf captures the behavior of the HQ rain rate distribution.

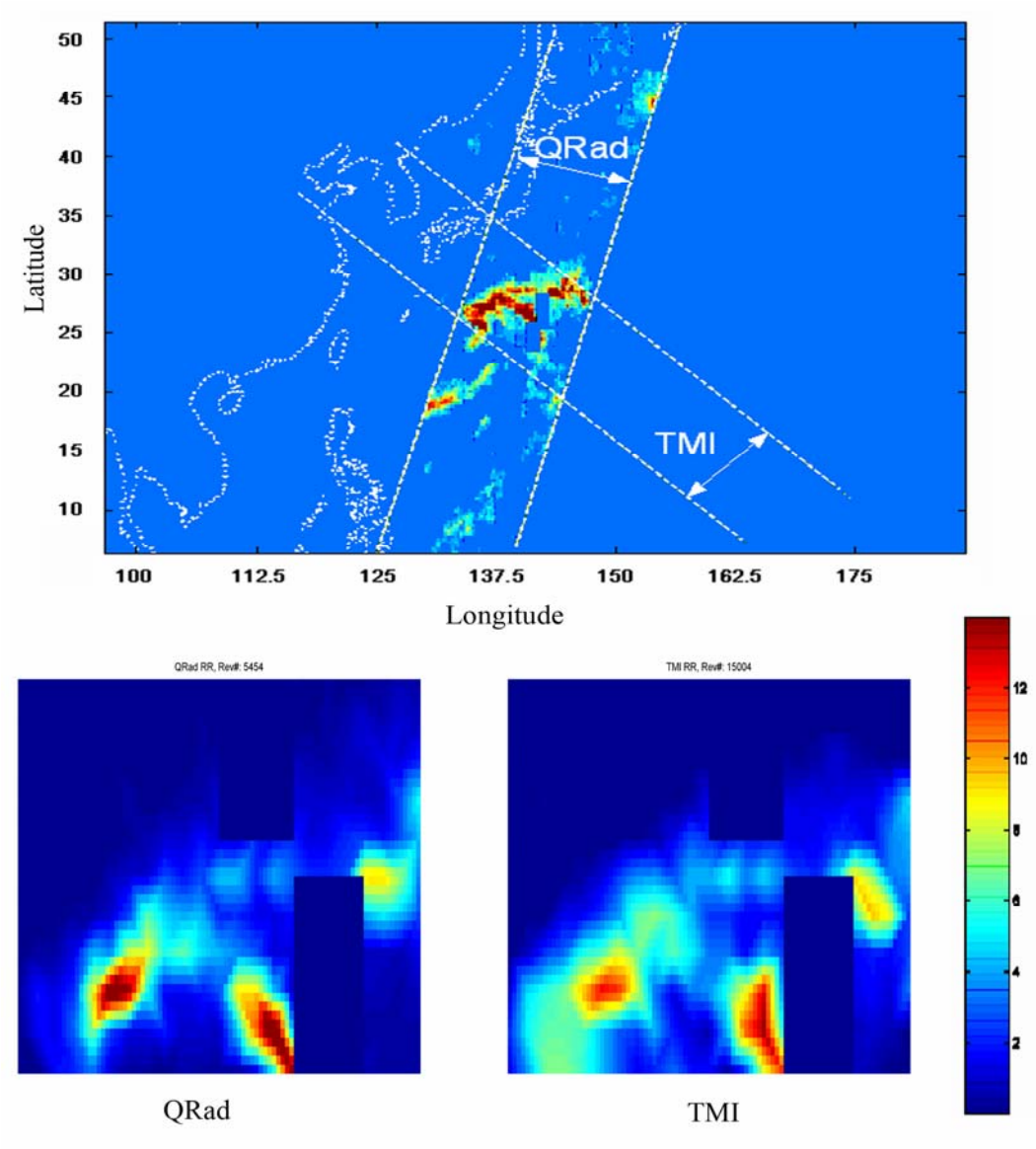

Figure 24: Example of instantaneous rain rate images produced by QRad and TMI. Spatial sampling is 0.125° (12.5 km), and coincidence time difference is ~20 min.

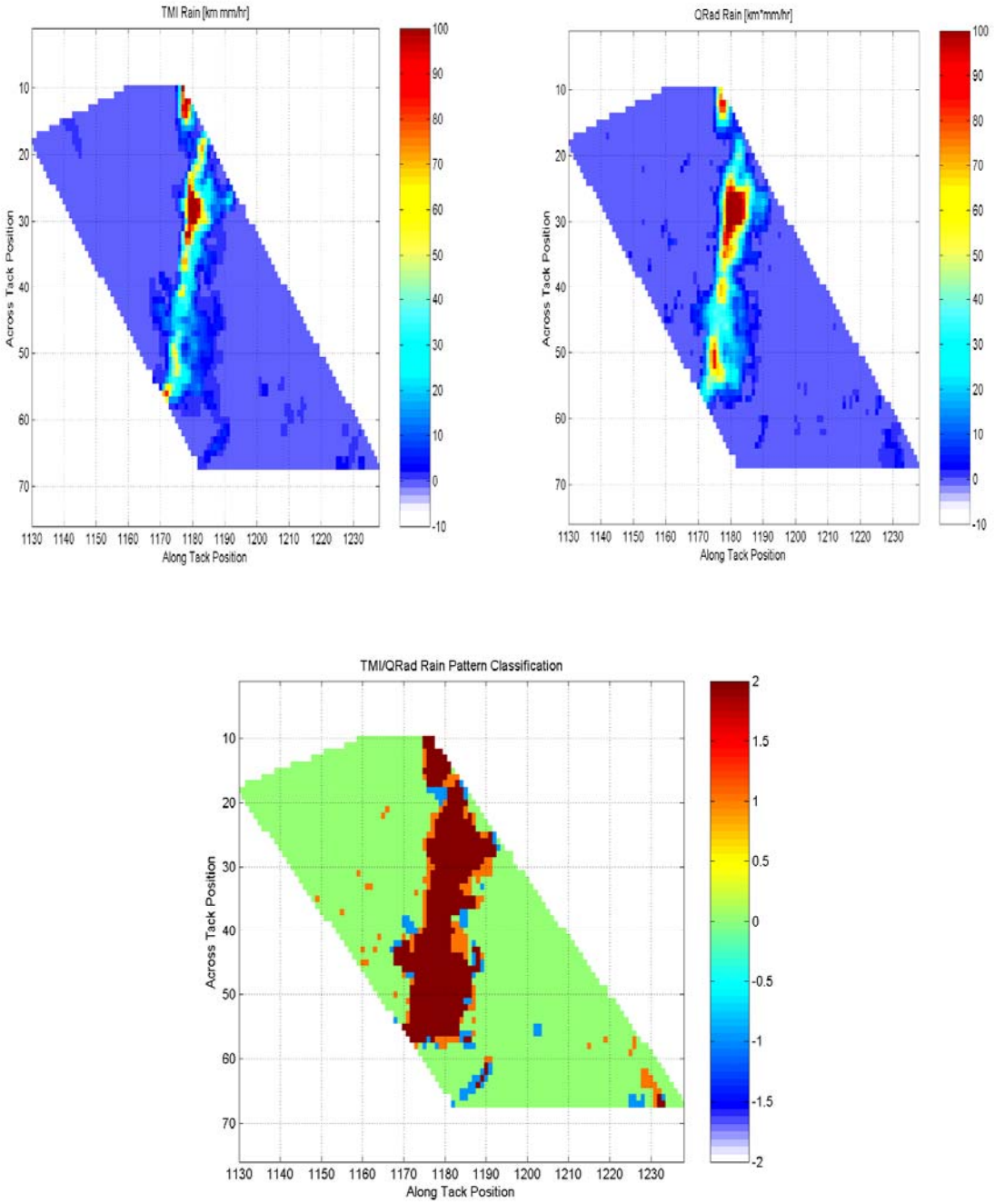

Figure 25: A second example of a rain event measured by TMI 2A12 product (top left panel) and QRad (top right panel). Spatial resolution is 25 km (WVC measurement grid) and coincidence time difference ~ 10 minutes. Lower panel depicts the corresponding rain pattern classification. Classification categories include: agreement (color indices 0, green & 2, deep red), false alarm (color index 1, orange) and miss rain (color index -1, blue).

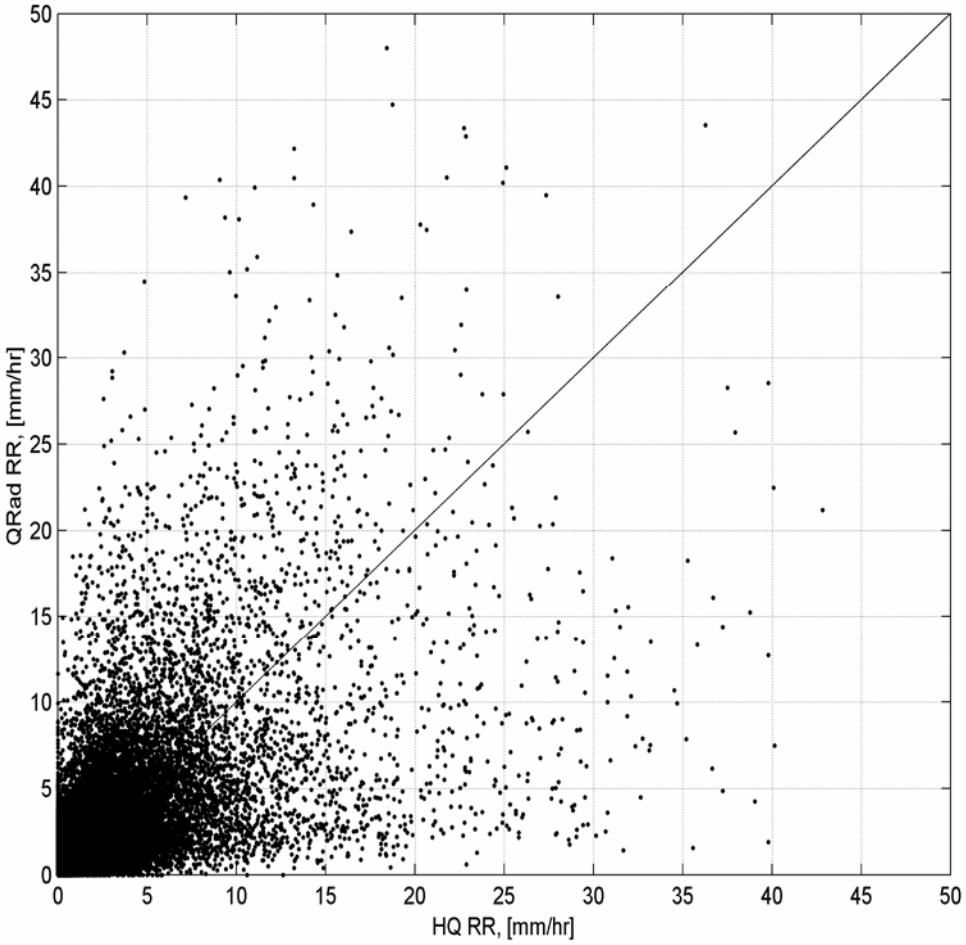

Figure 26: Instantaneous rain rate comparisons for a hundred and eight collocated rain events for QRad and TRMM 3B42RT HQ (TMI and SSM/I) product. Spatial resolution is 0.25° (25 km) and coincidence time difference is < 75 minutes.

Table 7: Instantaneous rain rate (mm/hr) differences for five TRMM 3B42RT HQ data ranges. For each range, the difference (QRad minus HQ) is calculated.

HQ Range	Number of points	Difference mean	Difference std	Difference rms/<HQ>
0 – 1	14582	0.5330	0.9548	2.6428
1 – 2	7842	0.3571	1.7383	1.2278
2 – 4	6492	0.1350	2.7590	0.9736
4 – 8	3637	-0.5062	4.0268	0.7385
> 8	1939	-4.2267	8.9058	0.7218

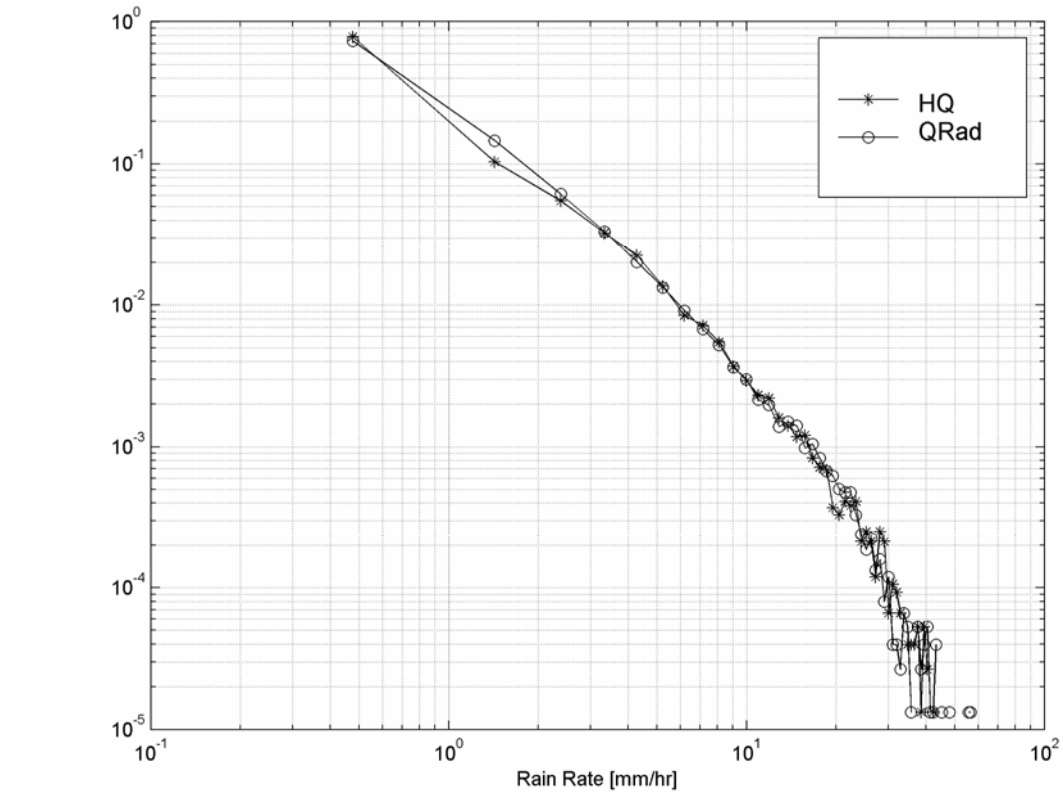

Figure 27: Rain rate probability density function for a hundred and eight collocated rain events for QRad and TRMM 3B42RT HQ (TMI and SSM/I) product

Next, we present sample image comparisons of collocated rain events of QRad and HQ retrieved rain rates. Although these collocated rain events are obtained from the 3-hour UTC windows, we utilize a satellite orbit database, along with specialized collocation tools to estimate the overpass time differences between QRad and HQ observations. These collocations span a period of about two weeks during the month of June 2003. First, the QRad rain was put into 3-hour universal time windows (± 90 minute span around synoptic observation hours 00 UTC, 03 UTC, 06 UTC, … , 21 UTC). Then, the resulting time binned rain images were gridded to a 0.25° x 0.25° latitude / longitude Earth measurement grid to match the HQ rain product resolution.

The upper panel in Figure 28 shows a collocated rain event with low rain values that was observed on June 18 2003 during the 06 UTC time-window where the coincidence time differences are < 35 min. The QRad rain rates are shown on the right side, while the HQ rain rates are shown on the left side, and the color bars indicate the rain rate (mm/hr) values. The correlation coefficient between the two images is 85%. The lower panel shows a second collocated rain event with moderate rain values that was observed on June 21, 2003 during the 06 UTC time-window where the coincidence time differences are also < 35 min. For this case, the spatial correlation coefficient is 75%. A third rain image comparison presented in the upper panel of Figure 29 represents an example of high rain rate that was observed on June 24, 2003 during the 15 UTC time-window where the coincidence time differences are < 60 min. The correlation is found to be 80%. The last collocated rain event example is shown in the lower panel of the same figure. This rain event was observed on June 25, 2003 during the 15 UTC time-window

where the coincidence time differences are also < 60 min. The correlation coefficient for this event is found to be 85%.

In general, there is very good spatial correlation between QRad and HQ rain patterns. Because of the smaller IFOV and lower ΔT, the HQ images are "crisper"; nevertheless, the shape and relative intensity of the rain events are well captured by the QRad images. On an absolute basis, the QRad underestimates the higher rain rates because of the non-linear effects of beam filling. Further, the effects of the high ΔT result in "noisy pixels" that is apparent in the QRad rain images. Most differences between HQ and QRad are attributed to errors in the QRad retrievals; however some differences may be "real" in that they could be the result of the different pass times of QRad and HQ over the rain events.

When compared to rain measurements obtained form visible / infrared satellite observations, microwave based QRad rain estimates perform superbly. As an example, Figure 30 presents two collocated rain events between QRad and the TRMM 3B42RT VAR data product. The QRad rain rates are shown on the right side, while the VAR rain rates are shown on the left side. The color bars are proportional to the rain rate (mm/hr) values. For these comparisons we apply a conservative threshold of 1 mm/hr to QRad rain rates to eliminate any random bogus rain pixels. In both cases, it can be seen that the VAR rain estimates failed to detect a significant portion of the low and moderate rain event structure. These examples are quite typical, and they emphasize the superior performance of the microwave rain retrievals compared to rain estimates from visible and infrared sources.

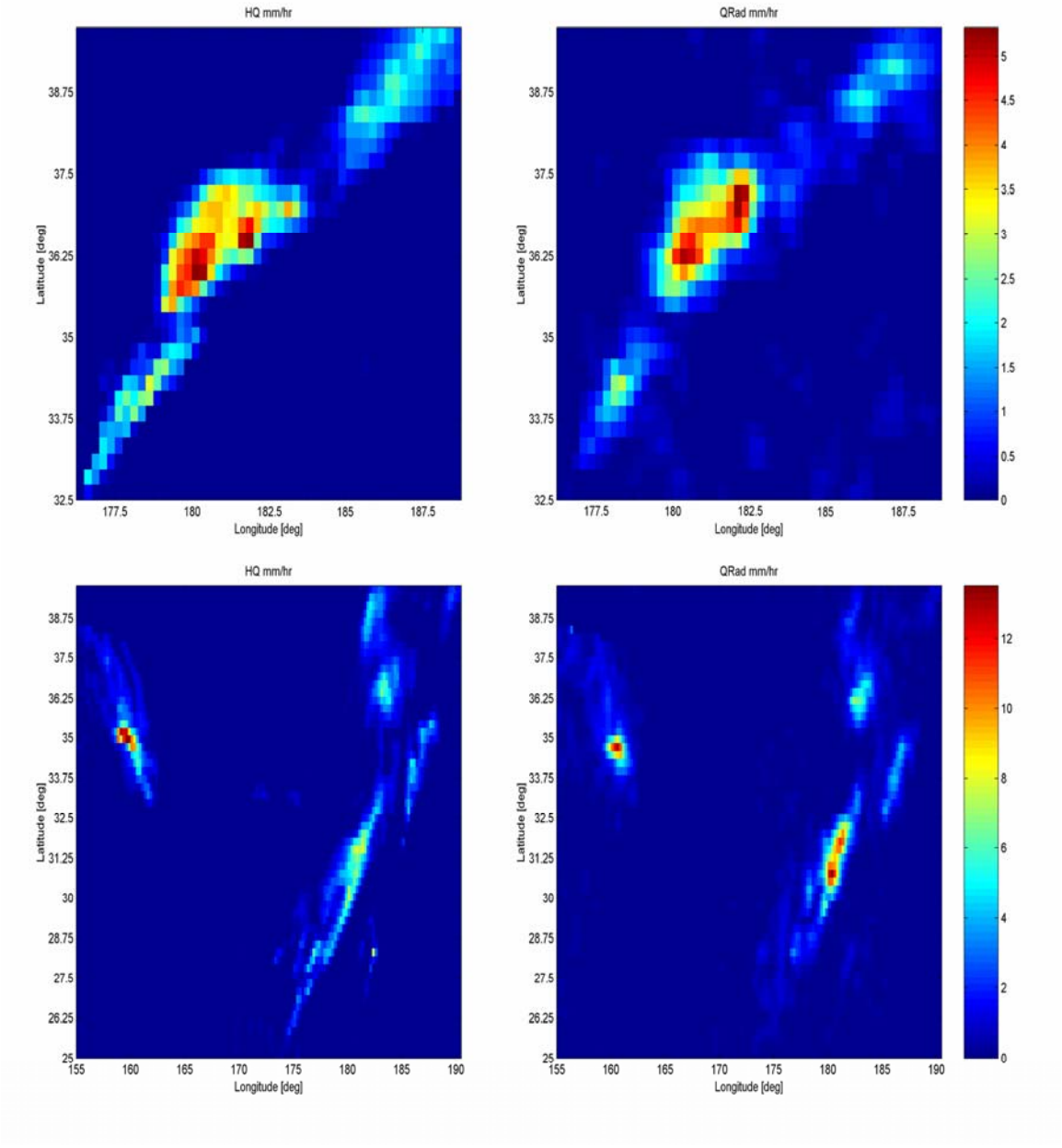

Figure 28: Examples of rain events measured by QRad (right) and TRMM 3B42RT HQ (TMI and SSM/I) product (left). Spatial resolution is 0.25° (25 km) and coincidence time difference < 35 min.

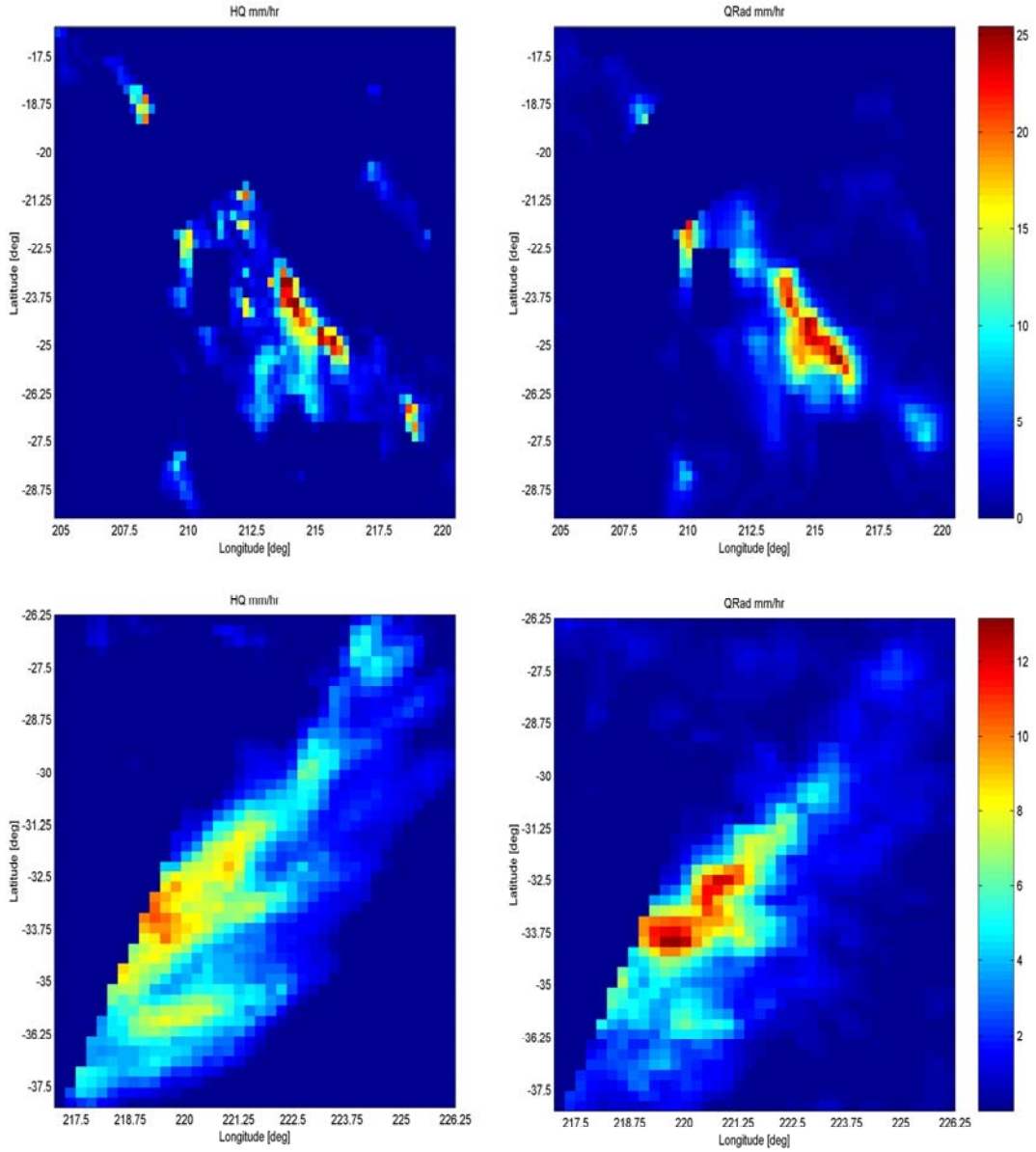

Figure 29: Other examples of rain events measured by QRad (right) and TRMM 3B42RT HQ (TMI and SSM/I) product (left). Spatial resolution is 0.25° (25 km) and coincidence time difference < 60 min.

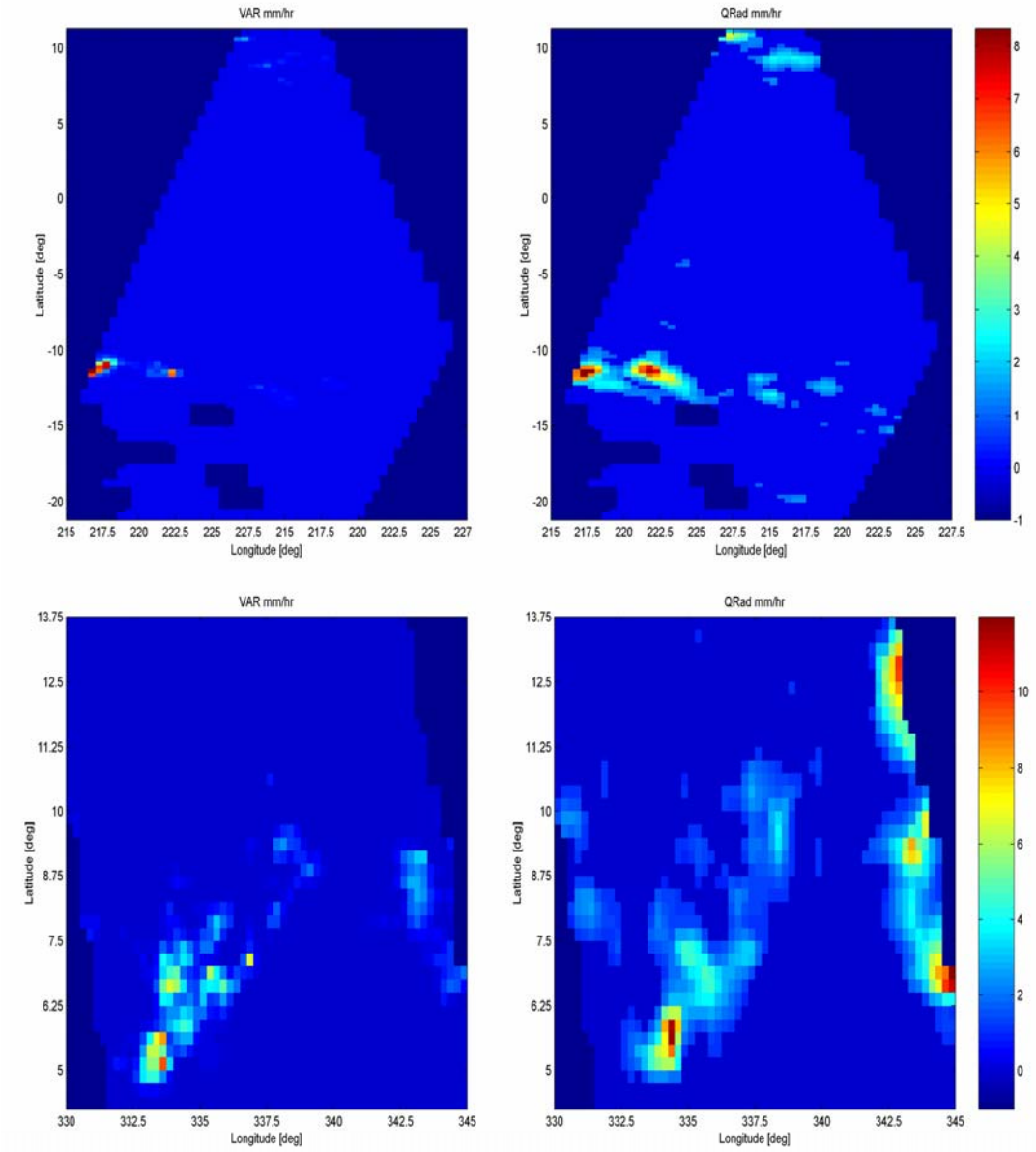

Figure 30: Typical examples of near-simultaneous collocation cases for QRad (right) and TRMM 3B42RT VAR (visible and infrared) product (left). Spatial resolution is 0.25° (25 km).

Averaged Rain Rates

For the average rain rate product, we perform temporal (pentad) and spatial (0.5° x 0.5°) averaging of all instantaneous rain rate values which significantly reduces the random component of the rain retrieval. As an example, Figure 31 shows the average rain rate for March 2000, produced from QRad, TMI and SSM/I-F13, averaged over the global region ±40° latitude on a 0.5° x 0.5° latitude / longitude grid. As the spatial resolution decreases (i.e., spatial averaging area increases), the correlation improves. An example of the differences between the three rain rate retrievals for 0.5° x 0.5° for March 2000 is presented in Figure 32, and the statistical measures for these cases are given in Table 8. Here, there is excellent agreement between TMI and SSM/I and quite reasonable comparisons for both with QRad. Most of the difference occurs in the vicinity of the Inter-Tropical Convergence Zone (ITCZ) area where the convective rain activity predominates. In general, there is excellent correlation between the spatial patterns of rain; however there are fine scale differences due to the larger spatial resolution of QRad, and its poorer radiometric precision (ΔT). Nevertheless, the shape and the relative intensity of the rain are well captured by QRad.

Finally, Figure 33 shows a time series of QRad and TMI zonal five-day (pentad) rain rates, averaged over the tropical ocean from 0° N to 20° N. Pentad averages were calculated for about nine months during January 2000 through September 2000. Although QRad slightly over estimates the rain rate, there is high correlation between these two time series (~ 86%), and this result is in excellent agreement with a similar study of Imaoka and Spencer [37] between pentad averages for TMI and SSM/I.

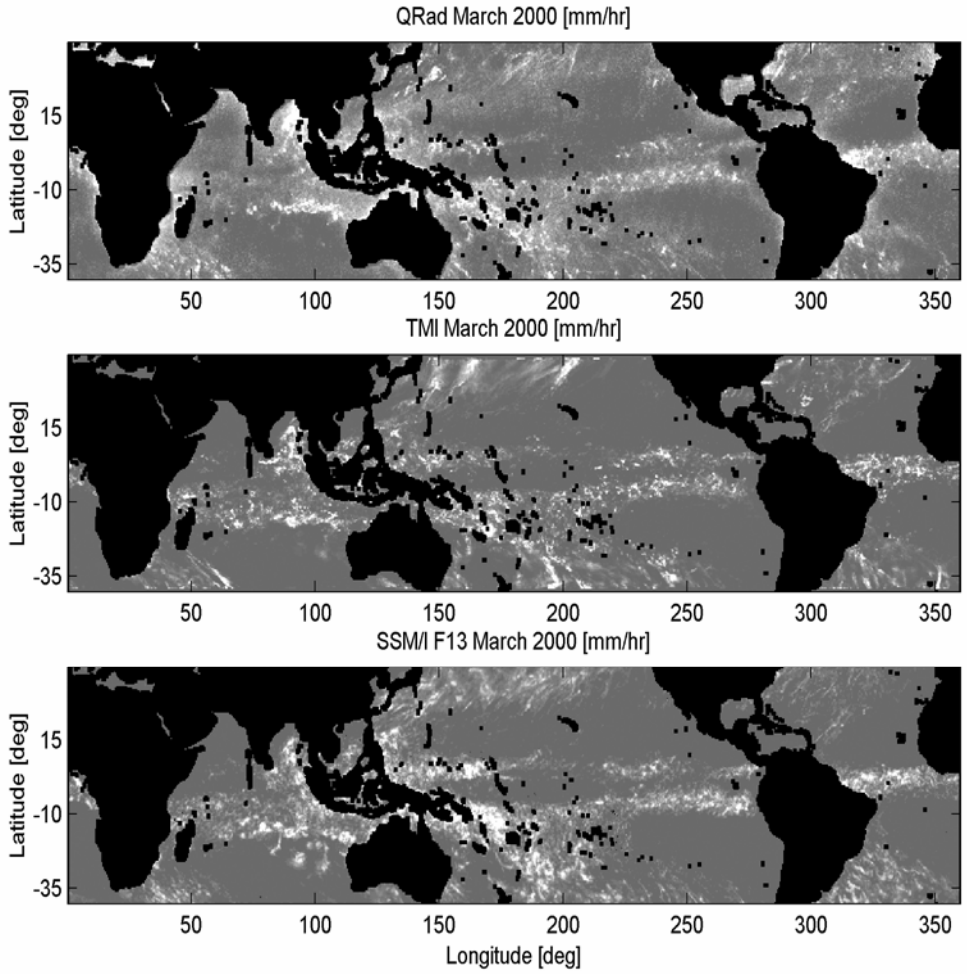

Figure 31: Monthly rain images produced by QRad, TMI and SSM/I F13 for March 2000. Spatial resolution 0.5º (50 km).

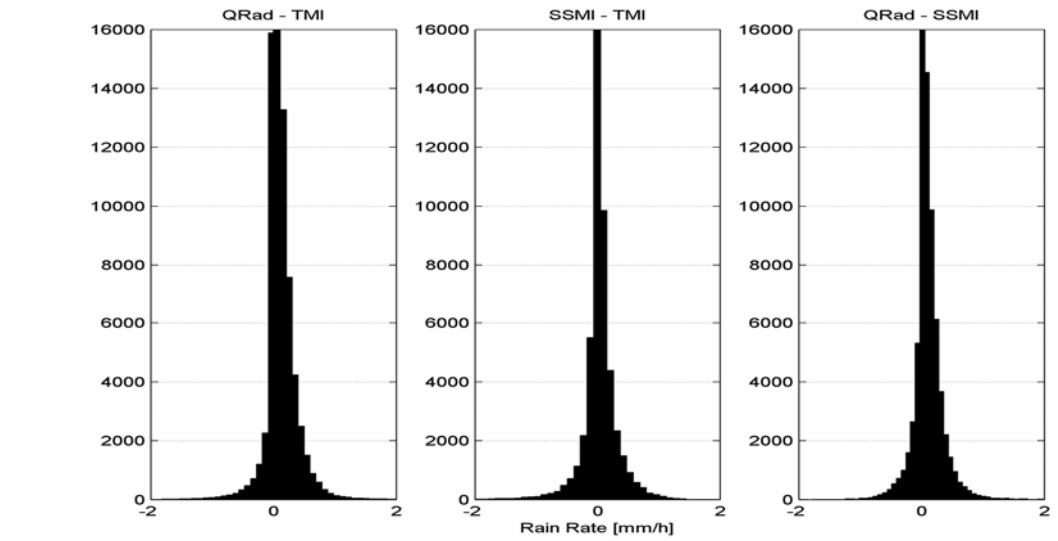

Figure 32: Monthly, global, 0.5° x 0.5° spatially averaged, rain rate differences for March 2000. From the left are: QRad-TMI, SSM/I-TMI, and QRad-SSM/I.

Table 8: Monthly average rain rate (mm/hr) differences between QRad/TMI, SSMI/TMI, and QRad/SSMI for March 2000.

Difference	Number of points	Difference mean	Difference std
QRad - SSMI	75463	9.877 e-2	2.50 e-1
QRad - TMI	75463	1.148 e-1	2.78 e-1
SSMI - TMI	75463	1.892 e-2	2.56 e-1

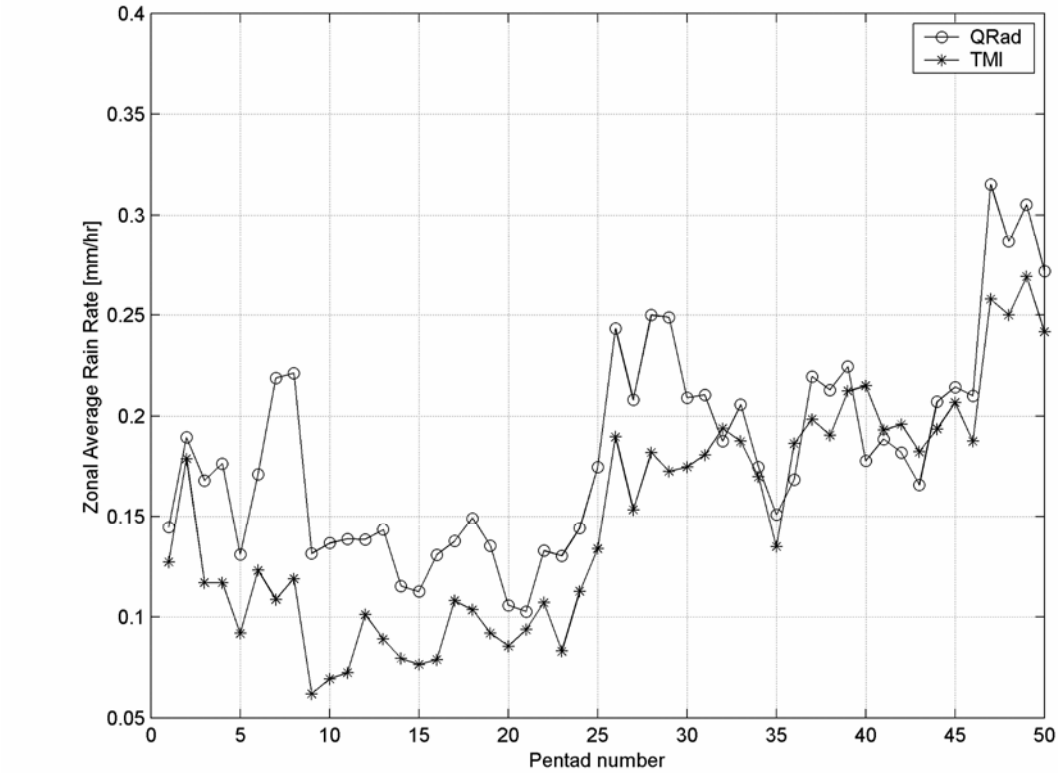

Figure 33: Zonal averages (0° N to 20° N) of five day (pentad) average rain rate for QRad and TMI from January 2000 through September 2000.

CHAPTER SIX: MODELING SEAWINDS ACTIVE BACKSCATTER MEASUREMENTS IN THE PRESENCE OF RAIN

Introduction

The scatterometer SeaWinds is a Ku-band microwave sensor that was originally designed as a specialized radar to measure the speed and direction of the near-surface wind vector over the ocean. SeaWinds employs a conical scanning, dual polarized pencil beam antenna system to collect the normalized radar cross section (σ^0) measurements from the Earth's surface. The inner beam is horizontally polarized (H-pol) with an incidence angle of 46º, while the outer beam is vertically polarized (V-pol) with nominal incidence of 54.1º. The SeaWinds conical scan design affords continuous wide swath coverage of about 1800 km, without a nadir gap.

Once the σ^0 measurements are made, the oceanic wind vector retrieval process is performed by inverting a geophysical model function (GMF) relating the radar backscatter and near surface vector wind. The GMF exhibits a bi-harmonic ($\cos 2\chi$) dependence on wind direction; therefore, multiple σ^0 measurements from several azimuth angles are required to determine the wind vector. Due to the noisy σ^0 measurements and the periodic nature of the GMF, multiple wind vector estimates (aliases) may exist. To select a unique solution, a post estimation procedure known as dealiasing is required.

In rain free, moderate wind speed regions, winds estimated by the SeaWinds scatterometer are proven to be remarkably accurate. However, in the presence of rain, the

accuracy of the retrieved wind vector can be adversely degraded. The impact of rain on scatterometer σ^0 measurements is threefold: first, rain drops falling on the ocean surface perturb the surface and alter the wind induced backscatter signature. Second, the atmospheric rain volume generates additional backscatter, which augments the radar backscatter from the surface. Third, rain has a two-way attenuation effect on the scatterometer signal passing through the rain volume.

Operating at a Ku-band frequency of 13.4 GHz, the SeaWinds scatterometer is more susceptible to rain effects compared to its counterpart C-band scatterometers. The impact of rain on the backscattered signal measured by SeaWinds is further amplified due to its high incidence angles of operation. This sensitivity of the SeaWinds backscatter measurements to the presence of rain can be exploited to provide quantitative rain estimates from the measured backscatter signal.

In this chapter, we develop a simple forward model to characterize the effects of rain on SeaWinds measured backscatter signal. With the assumption that the rain effects are isotropic, the polarized scatterometer signal is empirically modeled as a function of the integrated rain rate and the wind vector. Following this introduction, we present a brief description of the training dataset utilized in building our model. In the third section, we provide a detailed discussion of the development of the empirical forward model, which is specifically tuned to SeaWinds geometry and operating frequency. Validation of the model is performed through comparisons with actual backscatter measurement data from SeaWinds. Results demonstrate the fact that the simple model can accurately reproduce the effects of rain on the measured backscatter signal. This forward model will be used later in conjunction with SeaWinds active backscatter measurements to formulate

a combined passive / active mathematical inversion algorithm to enhance the passive-only oceanic rainfall estimates from QRad.

Training Dataset

In order to model the effect of rain on the backscatter measurements obtained from SeaWinds, we collocate SeaWinds σ^0 observations with rain measurements produced by the Tropical Rainfall Measuring Mission (TRMM) Microwave Imager (TMI) and the numerical weather prediction (NWP) wind fields from the National Centers for Environmental Prediction (NCEP). The same collocation database, consisting of four hundred twenty one near simultaneously observed regions of major rain events, used earlier in training the passive QRad algorithm is utilized again to estimate the rain induced model parameters. Each collocated region consists of the overlapping swaths of the SeaWinds and TMI instruments in which the overpass time difference is restricted to be within ± 30 minutes. The importance of such near simultaneous observation is driven by the fact that the spatial structure and intensity of a typical rain event can rapidly vary with time, thereby, a close collocation time difference is essential in order to capture the precipitation conditions affecting the SeaWinds scatterometer σ^0 measurements. The collocated rain events used in the forward model development activity are chosen from different seasons of the year 2000, having geographical locations (previously shown in

Figure 17) that span the full latitudinal range of the tropical rainfall region where rain is most frequent.

The SeaWinds σ^0 measurements are obtained from QuikSCAT level 2A (L2A) data product. Each L2A data product file contains σ^0 observations acquired during one full orbital satellite revolution (rev), spatially grouped by wind vector cell (WVC) rows. Each WVC row stores a scan of σ^0 measurements, and corresponds to a single cross-track cut of the SeaWinds measurement swath. Due to SeaWinds rotating pencil beam antenna design, the number of σ^0 measurements which fall within a particular WVC is highly dependent on the cell's cross-track location. Under nominal operating conditions, SeaWinds generates 709 pulses over its full swath as the spacecraft travels a distance of 25 km in the along-track direction, which is the width of a single WVC row. However, to accommodate the instrument highest pulse rate, the L2A product allocates space for a total of 810 measurement pulses per wind vector cell row. Thus, to cover a single satellite revolution, the 25 km resolution L2A product files reports the σ^0 measurements in a two dimensional array of 1624 WVC rows, and 810 cells per row.

The NCEP wind fields are used in our model to provide an estimate of the surface backscatter under non-raining conditions. These fields, included in the QuikSCAT level 2B (L2B) product are derived from operational NCEP maps which provide wind estimates at 1000 mbar level, having a spatial resolution of 2.5º x 2.5º on a latitude / longitude grid, and a temporal resolution of 6 hours. The NCEP wind speed and direction estimates in the L2B data files are interpolated to match the QuikSCAT wind vector cell locations. They are utilized as an external nudging source to aid filtering in the QuikSCAT wind retrieval processor and produce a unique wind vector field solution.

Compared to the L2A data product, the L2B file processing employs a different data organization. The L2B processor generates a grid of wind vector cells (WVC) aligned in the along-track and the cross-track axes of the QuikSCAT spacecraft measurement swath, where each WVC is a square with a dimension of 25 km. Therefore, in order to acquire data for one complete satellite orbital revolution, a total of 1624 WVC rows (in the along-track direction), with 76 WVCs per row (in the cross-track direction) are needed. The differences between L2A / L2B data organization necessitate co-registering both data sources on a common grid. To achieve this goal, the L2A σ^0 measurements are collocated on the L2B WVC grid. For each WVC, the σ^0 measurements falling within the cell are averaged and assigned to that particular WVC location. Both, the L2A and L2B data products are available from NASA Physical Oceanography Distributed Active Archive Center (PODAAC) at the Jet Propulsion Laboratory (JPL).

To evaluate the effect of rain on SeaWinds backscatter σ^0 measurements, we utilize the integrated rain rate estimates obtained from the TMI sensor. As noted previously, due to the lack of direct integrated rain rate measurements by TMI, we approximate the integrated rain rate values as the product of the TMI surface rain rate obtained from the TRMM 2A12 data product, and the freezing rain height from the TRMM 3A11 data product. Once an estimate of the integrated rain rate is obtained, it is collocated with the SeaWinds σ^0 measurements and the NCEP wind fields on a common WVC measurement grid structure.

Development of SeaWinds σ^0 Forward Model

This section presents the development of an empirical model to characterize the impact of rain on the backscatter measurements acquired by the SeaWinds instrument. The statistical model incorporates the effects of scatterometer signal attenuation and total augmentation on the measured backscatter due to the presence of rain.

Rain Effects on SeaWinds σ^0 Observations

In the presence of rain over the ocean, the SeaWinds scatterometer microwave signal may be affected in three ways: the rain drops impinging on the ocean surface alter the roughness of the centimeter scale capillary wave field by creating additional surface features such as the ring waves which result from the collapse of splash created stalk. Such rain induced features alter the wind scattering signature of the ocean surface by presenting additional backscattering from rain and suppressing the measured σ^0 wind directional dependence [47-49].

In addition to the rain surface perturbation effect on the measured backscatter, the volume of rain in the atmosphere has a two-way attenuating effect on the scatterometer signal; where the rain column attenuates both the transmitted radar signal, and the wind generated echo from the ocean surface. Additionally, the volume of rain scatters the

signal incident upon it, which under certain wind / rain combinations can completely mask the echo from the ocean surface.

At the high incidence angle measurement of SeaWinds, the path length which the scatterometer microwave signal has to travel increases, thereby, the rain attenuation and volume scattering effects are magnified. Likewise, the sensitivity of the backscatter signal to the roughness of the ocean surface becomes more pronounced at higher incidence angles. Thus, the Ku-band operating frequency and measuring geometry affords the SeaWinds instrument a high sensitivity to the presence of rain.

In literature, it is widely accepted to characterize the aforementioned effects of rain on the measured radar signal using the following simple mathematical form [30, 31]:

$$\sigma^0_{meas}(r,u,\chi,p,\theta) = \alpha(r,p,\theta)\cdot\sigma^0_{wind}(u,\chi,p,\theta) + \sigma^0_{excess}(r,p,\theta) \tag{6.1}$$

According to this model, the measured radar backscatter, σ^0_{meas}, is equal to the algebraic sum of two scattering terms in the normal space. The first term, $\alpha\cdot\sigma^0_{wind}$, represents the non-raining wind-generated surface scattering attenuated by α due to signal propagation through the rain column. The second term accounts for the additional (excess) scattering due to the presence of rain. The excess rain-induced backscatter component includes the scattering contributions from the attenuated surface perturbation, $\alpha\cdot\sigma^0_{surface}$, and the atmospheric rain volume, $\sigma^0_{rain-vol}$, and given by:

$$\sigma^0_{excess}(r,p,\theta) = \alpha(r,p,\theta)\cdot\sigma^0_{surface}(r,p,\theta) + \sigma^0_{rain-vol}(r,p,\theta) \tag{6.2}$$

In the above formulation, r denotes the integrated rain rate, u is the wind speed, χ is the relative azimuth direction, p is the polarization of the electromagnetic radiation and θ is the viewing angle of incidence of the radar instrument. In deriving this simplified model, it is assumed that the rain induced attenuation, $\alpha(r, p, \theta)$, and excess backscattering, $\sigma_{ex}^{0}(r, p, \theta)$, terms are isotropic functions of the rain rate, or in other words, these rain effects exhibit azimuth independence with respect to the radar antenna look direction through the rain volume. On the other hand, both rain attenuation and backscattering effects are dependent upon the incidence angle and the electromagnetic polarization of the radar signal. Since the SeaWinds scatterometer employs two pencil beams to collect backscatter measurements, and each beam corresponds to a particular polarization and incidence angle; where the inner beam is horizontally polarized (H-pol) at an incidence angle of 46º, and the outer beam is vertically polarized (V-pol) operating at 54.1º incidence; it is important to analyze the impact of rain on the polarized σ^0 measurements acquired by the two SeaWinds beams independently.

Estimating SeaWinds σ^0 Model Parameters

In order to estimate the rain induced attenuation and backscattering terms of the simplified model given by Equation (6.1), we utilize the tri-collocated dataset (described earlier) of SeaWinds backscatter measurements with NCEP numerical wind fields and the

integrated rain rates produced by TMI, with all three data source being co-registered on the SeaWinds 25 x 25 km measurement grid of wind vector cells (WVCs).

Previous studies have analyzed the effects of rain on SeaWinds σ^0 measurements using data from buoy [50], SSM/I radiometer [31], and TRMM precipitation radar (PR) [30]. For consistency purposes, in this dissertation we analyze the rain impact on SeaWinds σ^0 measurements utilizing data obtained from the TMI radiometer onboard TRMM satellite, which is the same data source used to derive the excess brightness temperature / integrated rain rate (T_{ex} – IRR) transfer functions employed in the passive QRad rain retrieval algorithm. As noted earlier, the TMI integrated rain rates are estimated as the product of the surface rain rate (mm/hr) and the rain path length (km). The path length is calculated using the rain freezing height retrieved by TMI and multiplied by the secant of the incidence angle of the TMI instrument. Because the integrated rain rate measurements from TMI are reported at a higher resolution compared to the SeaWinds 25 km x 25 km WVC measurement grid, the TMI measurements whose centers are included in a given WVC are averaged and assigned to that particular cell.

In the model parameter estimation activity, we use the collocated data from numerical weather prediction NCEP wind fields to provide estimates of the non raining wind induced surface backscatter, σ^0_{wind}. As noted earlier, the NCEP winds are interpolated in space and time to match the SeaWinds WVC locations. However, it is commonly known that under rain free conditions, the 1000 mbar NCEP wind estimates are somewhat biased high compared to the 10 m neutral stability wind measurements retrieved by SeaWinds. This bias is attributed to the differences in the measurement scale height, and the numerical prediction errors. Therefore, a bias correction is employed to

match the NCEP wind estimates to the winds measured by the SeaWinds scatterometer. By using regression analysis, and utilizing a large data set of near simultaneously collocated rain free SeaWinds / NCEP wind measurements, a first order multiplicative constant correction is determined as ($ws_{QuikSCAT} = 0.84 \times ws_{NCEP}$). The new bias corrected NCEP wind fields are projected through the QSCAT-1 GMF to produce an estimate of the rain free wind generated backscatter:

$$\sigma^0_{wind}\left(u, \chi, p, \theta\right) = \mathfrak{M}\left(u_{NCEP}, \chi_{NCEP}, p, \theta\right) \tag{6.3}$$

where $\mathfrak{M}$ denotes the QuikSCAT GMF table, θ is incidence angle of the SeaWinds instrument, p is the polarization of the electromagnetic radiation, u_{NCEP} is the bias corrected NCEP wind speed, and χ_{NCEP} is the relative azimuth direction defined as the difference between the antenna azimuth and the NCEP wind direction:

$$\chi_{NCEP} = Azimuth - wind\ direction \tag{6.4}$$

Once the TMI IRR, and the polarized non-raining surface backscatter contribution due to wind speed, σ^0_{wind}, are available, the estimation process of the rain induced attenuation and excess backscattering terms given by Equation (6.1), and their associated model parameters proceeds as follows:

First, quality control is performed on the WVC grided, tri-collocated training dataset. A conservative land mask is employed to exclude land contaminated pixels,

further, appropriate flags are applied to identify and remove any WVC pixel contaminated with ice or bad measurements from the analysis. Next, the collocated TMI integrated rain rate values are used to bin the polarized SeaWinds backscatter measurements, σ^0_{meas}, and the corresponding rain free, wind induced surface backscattering observations, σ^0_{wind}. As noted previously, because the H-pol and V-pol beams of the SeaWinds instrument have different characteristics, the σ^0 measurements obtained from each beam will be impacted by the presence of rain in a different fashion, and therefore, measurements acquired by each beam are analyzed separately in the parameter estimation process. For each particular antenna beam and integrated rain rate bin, least squares error analysis is performed using the binned σ^0 data to determine the best constant values for the multiplicative attenuation, α, and the additive excess backscattering, σ^0_{excess}, terms in Equation (6.1). The estimated quantities are assigned to the average TMI integrated rain rate value for the particular bin under consideration. The integrated rain bins are 5 km* mm/hr (~ 0.625 mm/hr) wide, and encompass the range of 0 – 200 km*mm/hr, observed in the training dataset. For the case of zero rain (as observed by TMI), an additional rain free bin is included, where it is assumed that the corresponding rain excess backscattering is negligible ($\sigma^0_{excess} \approx 0$), and there is no attenuation due to rain ($\alpha \approx 1$). The bin averaged data of the rain induced attenuation and excess backscatter (for both SeaWinds beams) are shown in Figures 34 and 35, respectively.

In the next step of the estimation process, parametric forms are chosen for the excess backscattering, σ^0_{excess}, and the attenuation, α, terms as a function of the integrated rain rate. The following mathematical forms are used to model α, and σ^0_{excess} [31]:

$$\alpha(r,p,\theta) = \exp(-k_\alpha(p,\theta)\cdot r^{\eta_\alpha(p,\theta)}) \tag{6.5}$$

$$\sigma^0_{excess}(r,p,\theta) = k_{ex}(p,\theta)\cdot r^{\eta_{ex}(p,\theta)} \tag{6.6}$$

In the last step of the model estimation process, a second regression analysis is performed to fit the selected parametric forms given by Equations (6.5) and (6.6) to the binned data, and determine the optimum values for the different parameters of the attenuation model (k_α, η_α), and the excess backscattering model (k_{ex}, η_{ex}). Each one of these four parameters takes two values corresponding to a particular SeaWinds beam (inner beam: p = H-pol, θ = 46º / outer beam: p = V-pol, θ = 54.1º). The values for the different parameters are listed in Table 9, and the resulting attenuation and excess backscattering models are shown as solid lines on Figures 34 and 35, respectively.

From these two figures, a number of key observations can be made. First, it is noted that as the integrated rain rate increases, the excess backscattering increases (shown in decibels), and the rain induced attenuation increases as well (shown in absolute decibels). Further, it is observed in Figure 34 that the SeaWinds outer (V-pol) beam experiences a higher attenuation in the presence of rain as compared to the inner (H-pol) beam. This is mainly due to the fact that the measurements acquired by the vertically

polarized outer beam travel a longer distance within the rain volume because of the beam's larger angle of incidence. Moreover, as Figure 35 illustrates, compared to their V-pol counterparts, the SeaWinds H-pol σ^0 measurements are more sensitive to rain, as is the case for the polarized radiometric excess brightness temperatures. This is due to the oblateness of the rain drops, especially at higher rain rates.

Using the parametric functional forms of the polarized rain induced attenuation, and rain excess backscatter, given by Equations (6.5) and (6.6), in conjunction with the simplified rain effect model of Equation (6.1), the polarized backscatter σ^0 measurements, as seen by the SeaWinds scatterometer, are simulated, and shown in Figure 36, as a function of the integrated rain rate and the wind induced surface backscatter. Also shown on the figure (solid red) is the locus of the backscatter σ^0 points, where the rain induced excess backscatter contribution is equal to 50 % of the simulated overall polarized backscatter σ^0 measurement. It can be readily seen from the figure that although the design of SeaWinds scatterometer was mainly optimized for oceanic wind vector observation, the response of SeaWinds twin beams, is rain dominated under a wide range of rain / wind combinations which are located in the upper diagonal regions of the figures. The sensitivity of SeaWinds instrument to the presence of oceanic rain will be utilized in the next chapter to retrieve quantitative estimates of the oceanic rainfall.

SeaWinds σ^0 Model Validation

In order to validate the simplified SeaWinds rain effect model given by Equation (6.1), we compare the model outputs to actual polarized σ^0 measurements acquired by SeaWinds as function of the integrated rain rate, and the wind generated backscatter estimates, σ^0_{wind}, obtained from the bias corrected NCEP wind vectors. Figures 37 – 40 show the SeaWinds backscatter measurements, σ^0_{meas}, plotted against σ^0_{wind} for the inner H-pol beam, and the outer V-pol beam, respectively. The rain rates listed on the subplots corresponds to the average of the rain rate bin used to generate the data.

In viewing the various scatter plots, it is helpful to recall that in the absence of rain, the polarized σ^0_{meas} and σ^0_{wind} data should be scattered along the perfect agreement lines. Also, it should be recalled that the magnitude of σ^0_{wind} (shown in decibels) is proportional to the wind speed magnitude (i.e., the larger the σ^0_{wind} magnitude, the higher the corresponding wind speed). It can be observed from the figures that the sensitivity of the SeaWinds σ^0 measurements to the presence of rain is dependent on the magnitude of the wind speed. For example, as can be seen from the top left panels in Figures 37 and 39, the low rain rate values can significantly affect the low σ^0 measurements, which corresponds to low wind speed observations, however, the impact of low rain on the high σ^0 measurements that corresponds to high wind speeds is negligible.

For each subplot in Figures 37 - 40, the predicted σ^0 values obtained using the simple rain model are shown in blue / green for the H-pol / V-pol beams, respectively. It is readily observed that the simple rain effect model of Equation (6.1) does track the data

very well, and therefore, this simple empirical model is capable of reproducing the impact of rain on the σ^0 measurements collected by SeaWinds.

Table 9: Coefficients of rain induced attenuation and excess backscattering models for SeaWinds scatterometer

	Attenuation (α)		Excess Backscattering (σ^0_{excess})	
	k_α	η_α	k_{ex}	η_{ex}
H-Pol	0.0893	0.3699	0.0023	0.5916
V-Pol	0.1337	0.4586	0.0030	0.4256

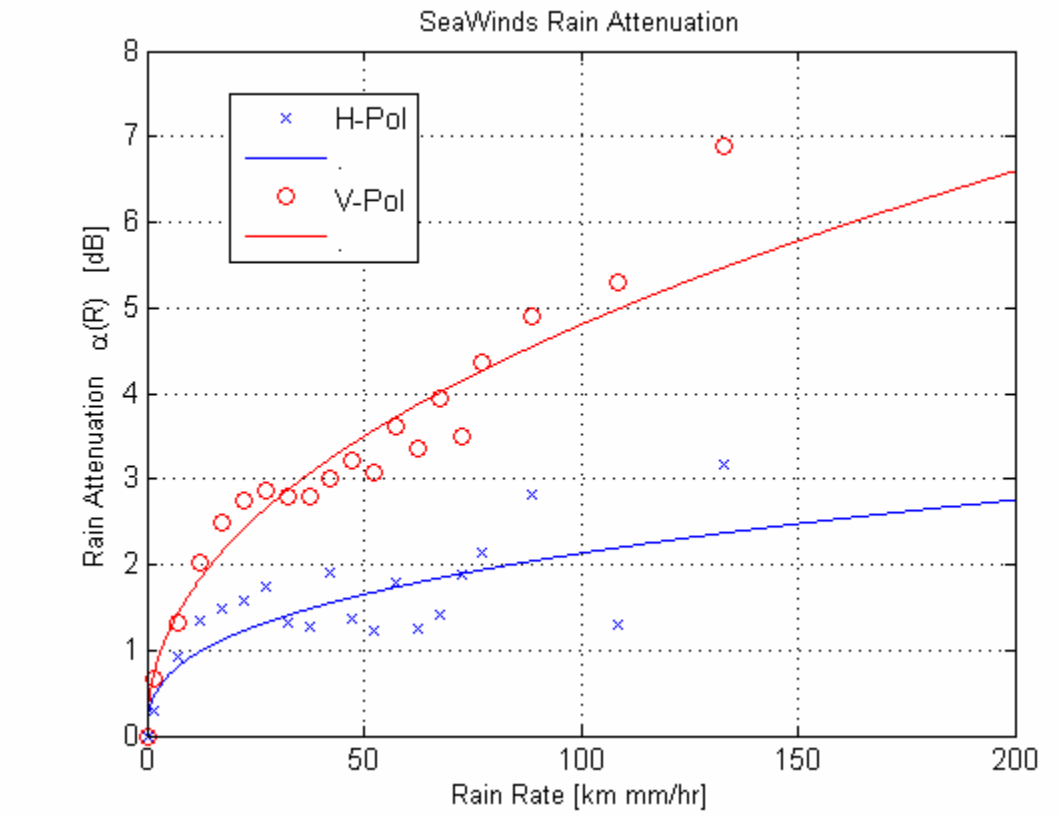

Figure 34: Rain attenuation as observed by SeaWinds H-Pol inner beam (blue), and V-Pol outer beam (red). The symbols denote the binned / averaged data. The solid lines depict the rain attenuation estimated using the parametric form given by Equation (6.5).

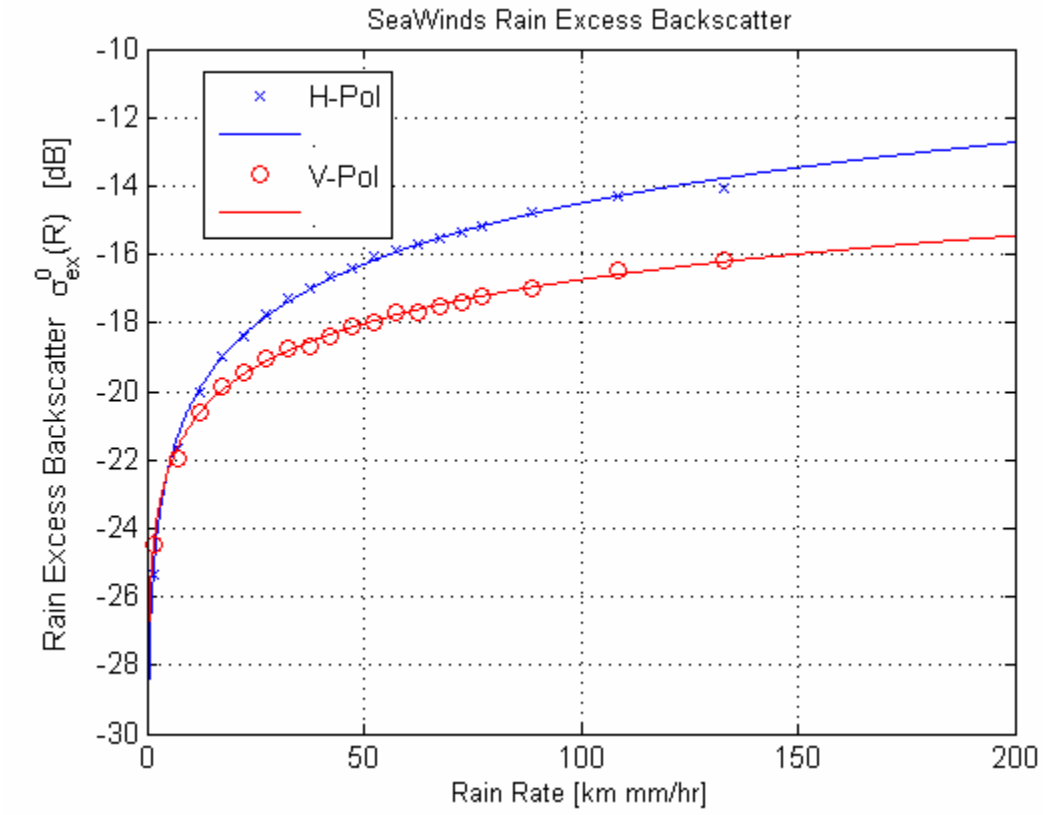

Figure 35: Excess backscatter due to rain as observed by SeaWinds H-Pol inner beam (blue), and V-Pol outer beam (red). The symbols denote the binned / averaged data. The solid lines depict the rain induced excess backscatter estimated using the parametric form given by Equation (6.6).

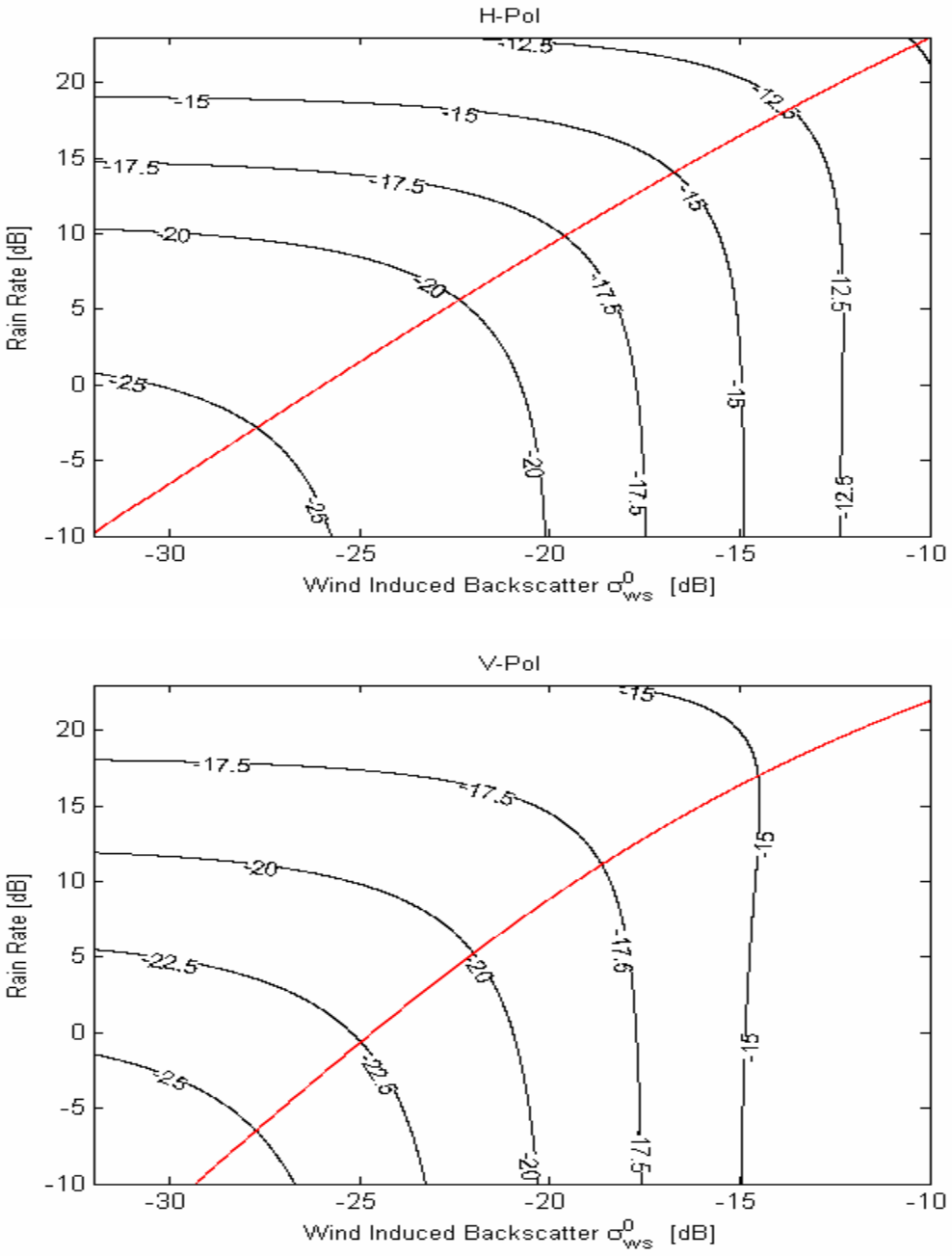

Figure 36: Simulation of SeaWinds scatterometer response as a function of rain rate and surface wind vector induced backscatter. The upper panel shows the response of the H-Pol inner beam, and the lower panel depicts the response of the V-Pol outer beam. The solid red lines indicate the response where excess backscatter due to rain is equal to 50% of the total observed backscatter.

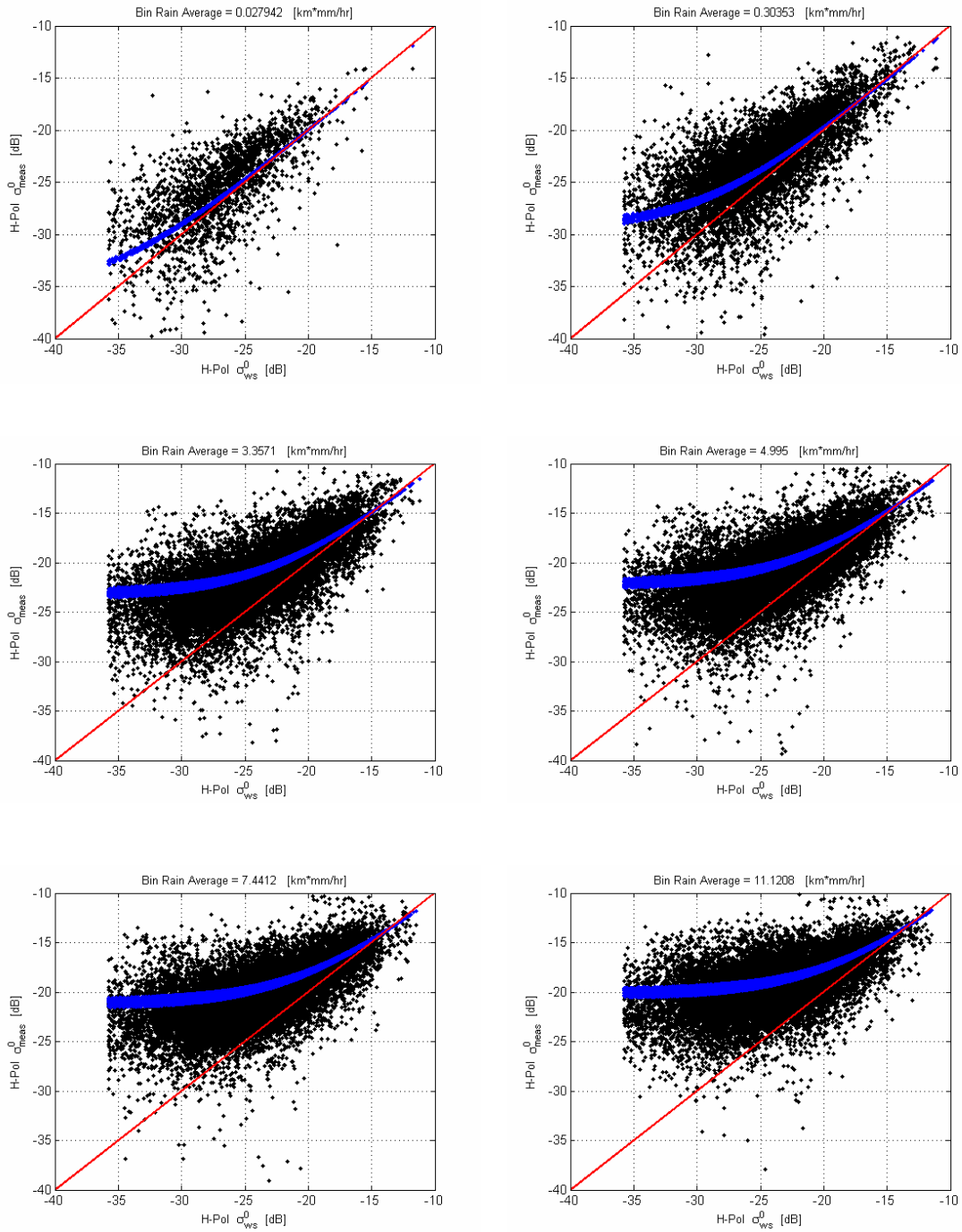

Figure 37: SeaWinds backscatter measurements acquired by the inner H-Pol beam plotted as a function of rain rate and wind induced backscatter. Blue represents the backscatter estimate from the simplified model of Equation (6.1).

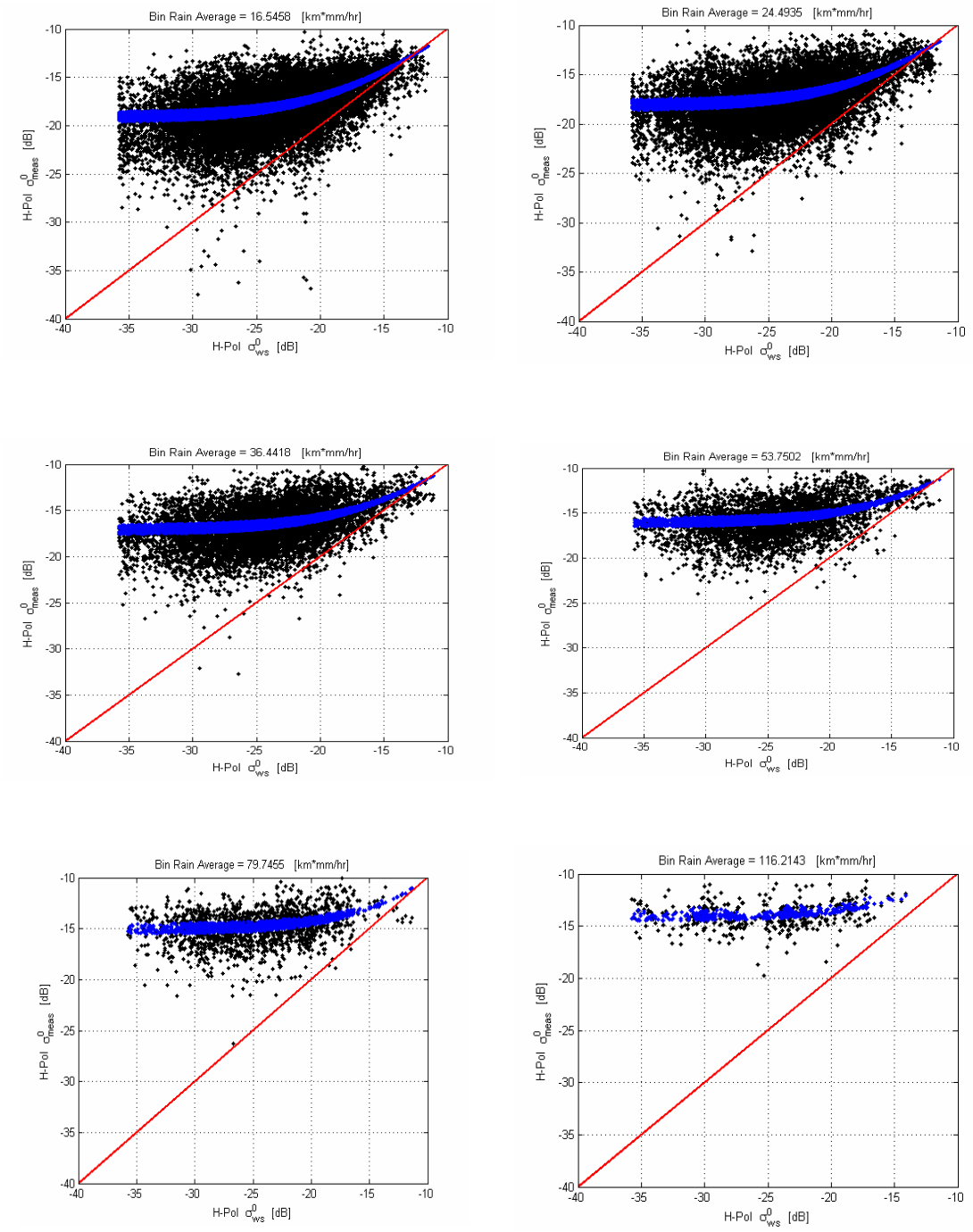

Figure 38: SeaWinds backscatter measurements acquired by the inner H-Pol beam plotted as a function of rain rate and wind induced backscatter. Blue represents the backscatter estimate from the simplified model of Equation (6.1).

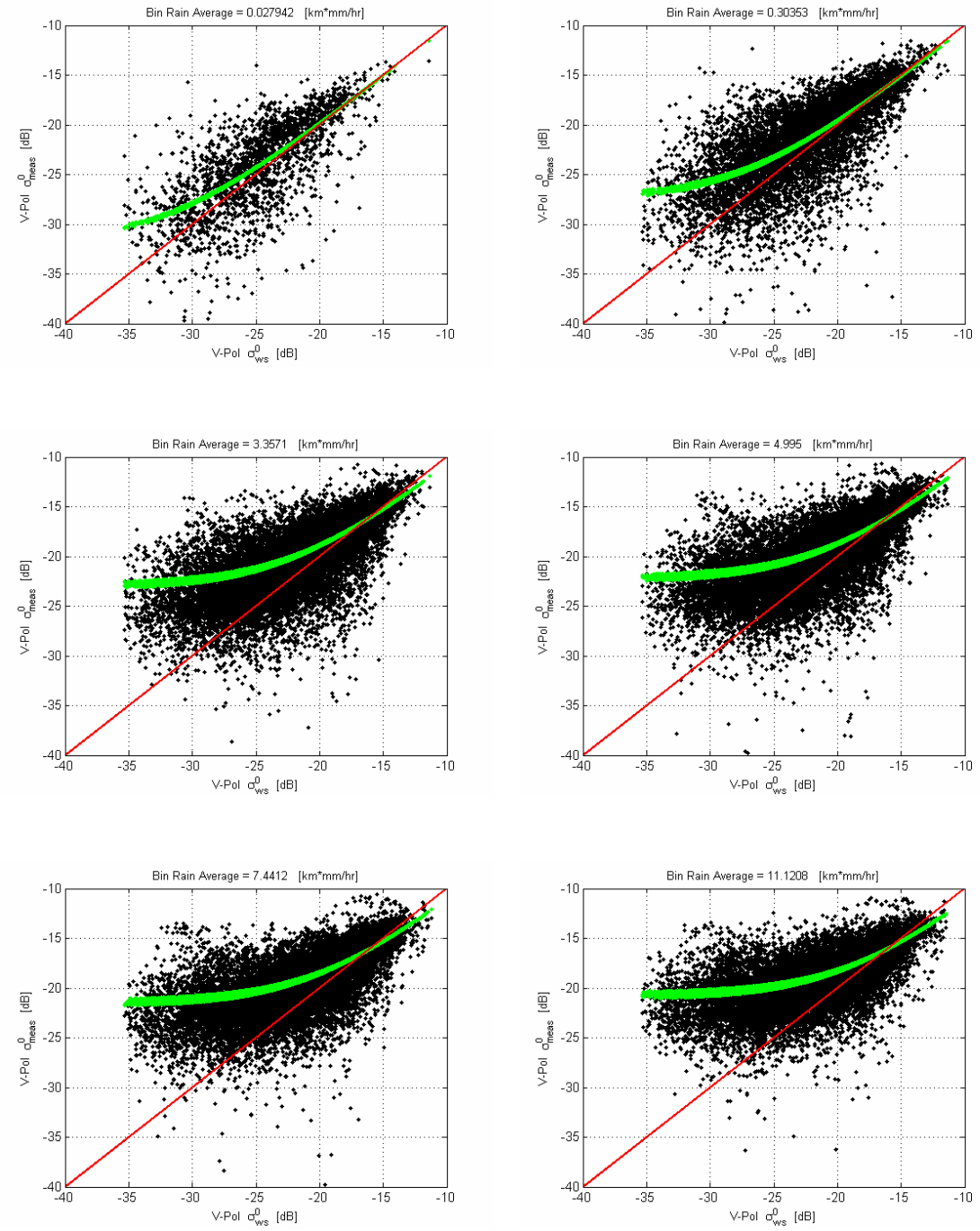

Figure 39: SeaWinds backscatter measurements acquired by the outer V-Pol beam plotted as a function of rain rate and wind induced backscatter. Green represents the backscatter estimate from the simplified model of Equation (6.1).

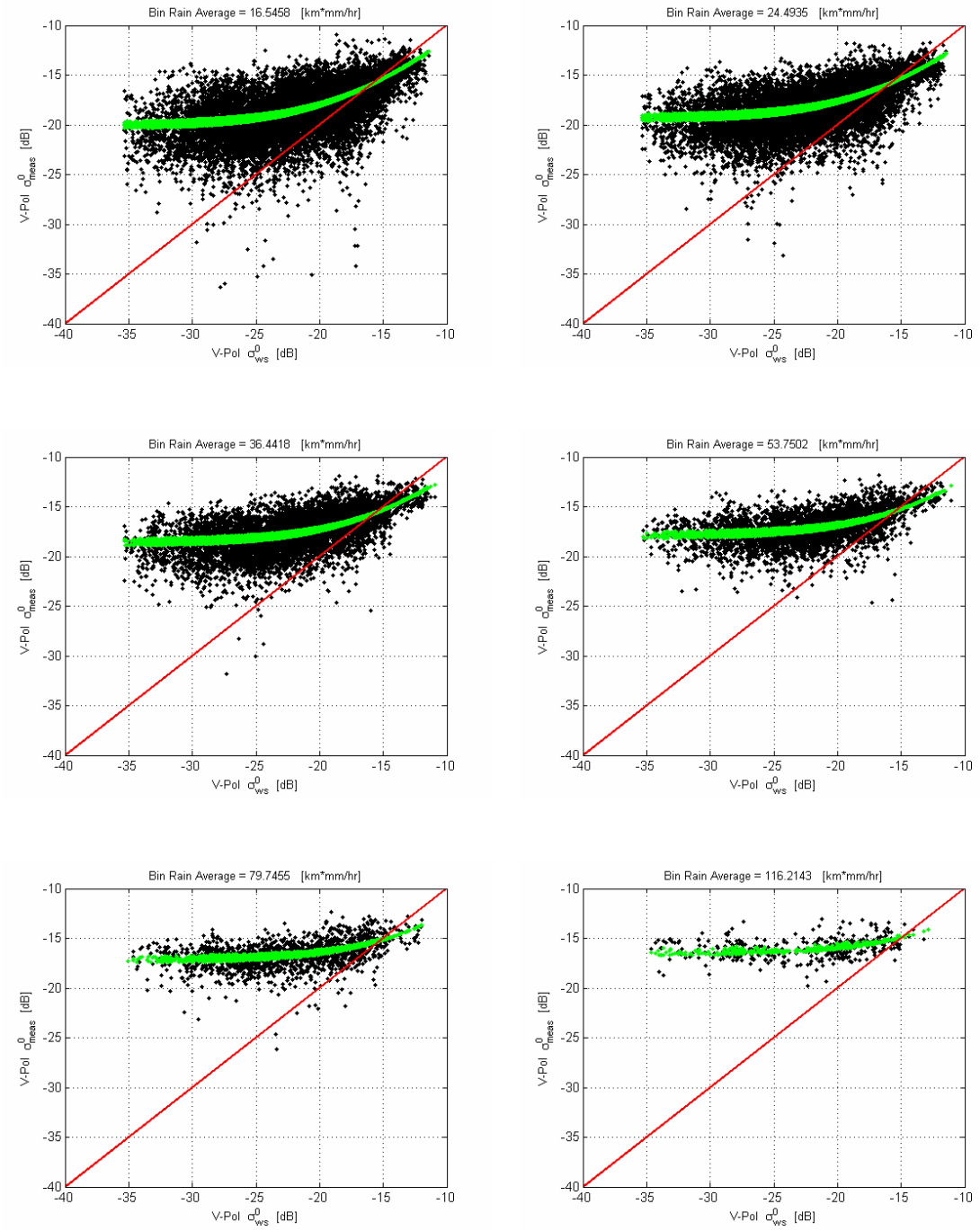

Figure 40: SeaWinds backscatter measurements acquired by the outer V-Pol beam plotted as a function of rain rate and wind induced backscatter. Green represents the backscatter estimate from the simplified model of Equation (6.1).

CHAPTER SEVEN: RAINFALL RETRIEVALS USING COMBINED PASSIVE AND ACTIVE MEASUREMENTS

Introduction

The SeaWinds microwave sensor has the simultaneous capability of measuring the polarized active radar backscatter, σ^0, as well as the passive radiometric emission, T_B, from the Earth surface and intervening atmosphere. The linearly polarized, σ^0 and T_B, measurements are collected by SeaWinds at a Ku-band frequency of 13.4 GHz over the entire 360º conical scan with separate offset pencil beams at 46° incidence (H-pol), and 54.1° incidence (V-pol). The individual T_B's are averaged on a spacecraft wind vector cell (WVC) measurement grid of 25 km resolution, which results in mean polarized T_B's and σ^0 measurements being perfectly collocated, spatially and temporally.

As discussed earlier, both active σ^0 and passive T_B measurements acquired by SeaWinds exhibit a high sensitivity to the presence of rainfall over the ocean surface. So far, we have utilized the rain sensitivity of the measured passive radiometric brightness temperatures to empirically establish brightness temperature – rain rate (T_B-R) transfer functions, which were employed in the framework of the passive QRad / SRad retrieval algorithms to provide estimates of the oceanic rain. Further, based upon the sensitivity of the SeaWinds active scatterometer signal to the presence of rain over the ocean, we developed in the previous chapter simple parametric models to quantify the rain induced

attenuation and the excess backscatter effects on SeaWinds σ^0 measurements as functions of the integrated rain rate.

In this chapter, we investigate incorporating the additional piece of rain information available from the SeaWinds active backscatter measurements to enhance the quantitative rain estimates derived from the passive-only QRad (and by implication, SRad) rain retrieval algorithm. Following this introduction, the combined passive / active algorithm, known as SeaWinds rain retrieval algorithm is discussed in details.

SeaWinds Passive / Active Rain Retrieval Algorithm

The physical basis of the SeaWinds rain retrieval algorithm [51] is the correlation between the polarized passive brightness temperature (T_B) / active radar backscatter (σ^0) measurements collected by the SeaWinds sensor, and the rain rates observed by the TRMM Microwave Imager (TMI). Due to the relatively long duration of the SeaWinds transmitted microwave pulse, the polarized rain induced passive emissions, as well as the polarized active backscatter measurements are directly proportional to the path integrated rain rate, which is the retrieved geophysical parameter from SeaWinds measurements.

The SeaWinds rain algorithm is tuned utilizing the same collocation dataset of four hundred twenty one rain events used previously to train the passive QRad algorithm, and to characterize the rain induced attenuation and backscattering effects on SeaWinds active σ^0 measurements. Figure 41, presents a simplified block diagram of the combined

passive / active SeaWinds rain retrieval algorithm. The data inputs to the algorithm are: the passive QRad (SRad) rain estimates, the individual polarized σ^0 measurements from level 2A (L2A) data files, and the collocated bias-adjusted NCEP wind vectors from level 2B (L2B) data product.

The various input data are co-registered on a spacecraft wind vector cell (WVC) measurement grid of 25 km x 25 km resolution, and used to make a correction for the rain attenuated oceanic surface wind vector backscatter contribution to the σ^0 measurements, and thereby, provide an estimate of the polarized rain induced excess backscatter, σ^0_{ex}, upon which the rain retrieval is based. The output of the SeaWinds algorithm is an instantaneous rain rate product, by satellite orbit revolution, which is posted on the 25 km WVC measurement grid. The instantaneous rain product can be fed to an averaging subroutine to provide a global, Earth gridded rain rate product.

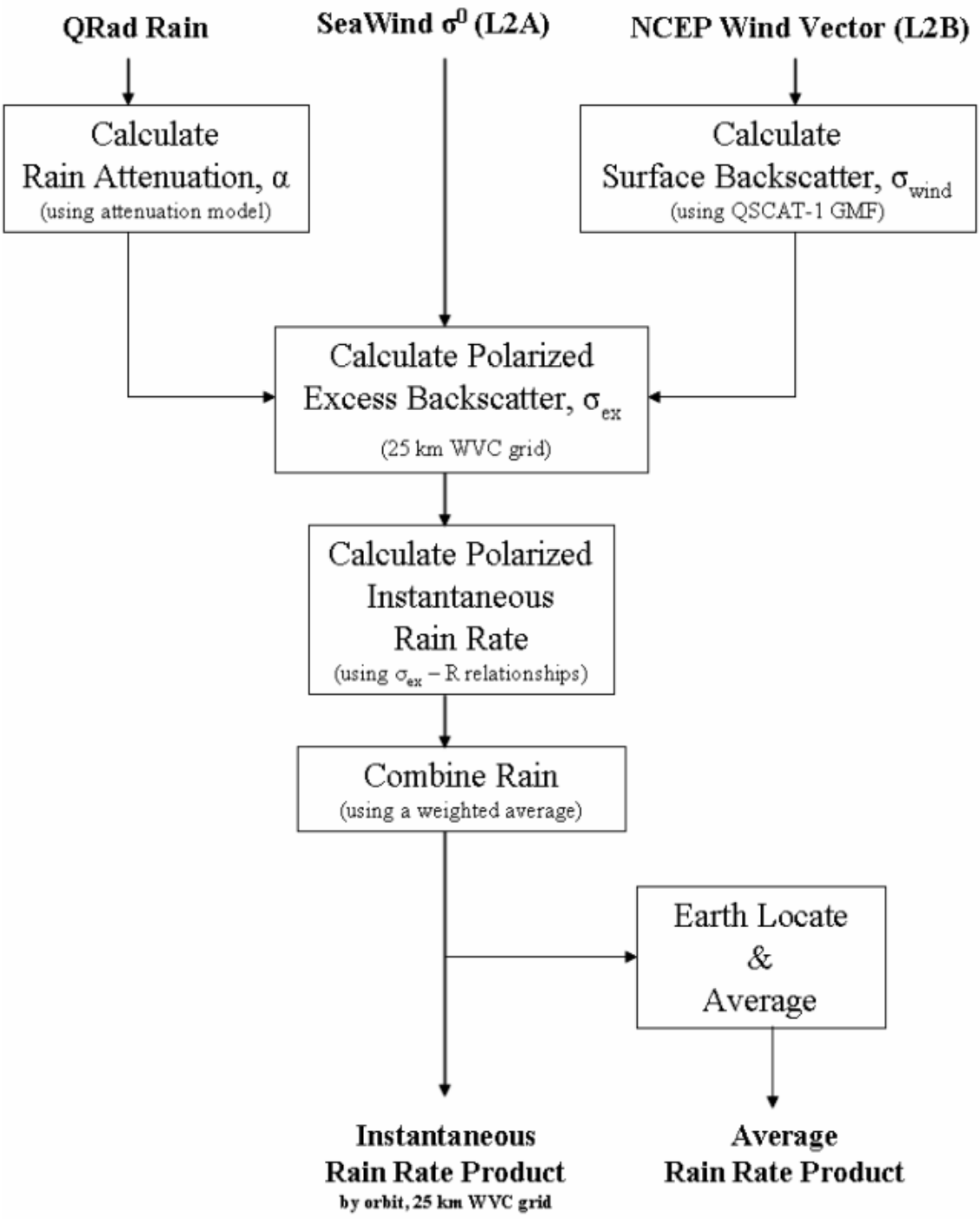

Figure 41: A simplified block diagram of the passive / active SeaWinds rain rate algorithm.

Rain Retrieval Methodology

The SeaWinds rain algorithm is a statistical inversion algorithm that exploits the additional rain sensitivity of SeaWinds active backscatter σ^0 measurements to enhance the passive-only rainfall estimates from QRad. The algorithm combines the passive QRad rain measurements, the active σ^0 measurements, along with the empirical rain induced excess backscatter and attenuation models to formulate a minimum objective function mathematical model that provides an improved quantitative estimate of the oceanic rain.

The SeaWinds combined passive / active rain algorithm retrieves the oceanic rain on a WVC measurement grid of 25 km spatial resolution. In order to get an accurate estimate of the oceanic rain from the polarized active backscatter measurements, it is necessary to correct for the transient contribution of the oceanic surface wind vector on the backscatter measured by SeaWinds. In this regard, we utilize the collocated NCEP wind vectors, which are projected through the QSCAT-1 GMF table using Equation (6.3), to produce an estimate of the wind generated surface backscatter (σ^0_{ws}). The rain contribution to the measured backscatter (σ^0_m) signal, defined as the rain excess backscatter (σ^0_{ex}), can be estimated by re-arranging Equation (6.1):

$$\sigma^0_{ex}(r, p, \theta) = \sigma^0_m(r, u, \chi, p, \theta) - \alpha(r, p, \theta) \cdot \sigma^0_{ws}(u, \chi, p, \theta) \qquad (7.1)$$

For each measurement pulse within a particular WVC, the attenuated wind backscatter contribution, $\alpha(r) \cdot \sigma^0_{ws}$, is estimated using the collocated QRad measurement

projected through the SeaWinds attenuation model, given by Equation (6.5). Next, the polarized rain rates are calculated from the estimated polarized excess backscatter measurements by formulating and minimizing a weighted least squared error objective function between the measurements and the excess backscatter model function:

$$J = \sum_{i=1}^{N} \frac{\left(\sigma_{ex,i}^{meas} - \sigma_{ex,i}^{model}\right)^2}{\delta_i(IRR_{QRad})} \tag{7.2}$$

where, N, is the total number of the polarized measurements (pulses) accumulated in a given WVC. The variance, δ_i, is estimated for each pulse using the QRad rain measurment in the corresponding WVC, along with the excess backscatter model of Equation (6.6). The final SeaWinds rain product (km*mm/hr) is a weighted average of the polarized rain estimates from Equation (7.2):

$$IRR_{SeaWinds} = \gamma_h \cdot IRR_h^{PA} + \gamma_v \cdot IRR_v^{PA} \tag{7.3}$$

In the above formula, the ^{PA} superscript is used as an indication that the polarized rain estimates (IRR_h^{PA} and IRR_v^{PA}) are derived from the combined passive / active measurements. The weighting factors, γ_h and γ_v, have the values of 0.90 and 0.10, respectively. These factors are empirically derived, and optimized using an iterative numerical subroutine that minimizes the mean square error (MSE) between the SeaWinds

rain estimates ($IRR_{SeaWinds}$) from Equation (7.3), and the collocated TMI IRR's over the algorithm training dataset.

The resulting scatter diagram between SeaWinds and TMI IRR's for the four hundred twenty one collocated rain events is shown in Figure 42. Also, for further comparisons, scatter diagrams are generated using the same dataset for different wind speed regimes as shown in Figure 43. As these figures illustrate, the SeaWinds retrieved rain rates exhibit a somewhat high variability compared to TMI rain, which is mainly attributed to the partial antenna beamfilling phenomenon (mostly pronounced at the high rain rates), and the inherent coarse radiometric resolution (ΔT) in the passive QRad measurement. Nevertheless, compared to TMI rain estimates, the retrieved SeaWinds IRR's are well correlated, and well behaved in the mean regardless of the underlying wind speed regime. This can be visually seen from the data points being reasonably scattered along the perfect agreement lines. Also, this can be verified by examining the statistics of the differences between overall data (SeaWinds – TMI) for various IRR bins, as presented in Table 10.

Next, we compare the performance of the rain retrievals derived from the combined passive / active SeaWinds algorithm to those obtained from the passive-only QRad algorithm. In performing the comparisons, it is necessary to recall that the passive brightness temperature measurements acquired by QRad are mainly rain dominated under most wind / rain conditions (previously simulated and shown in Figure 20). However, depending on the observed wind / rain combination, the active backscatter return collected by the SeaWinds twin beams (previously simulated and shown in Figure 36) can be either rain or wind dominated. Therefore, to identify the regime to which a given

SeaWinds-based WVC-rain estimate belongs, we calculate the average ratio of the rain induced excess backscatter to the total model backscatter estimate, given the NCEP wind vector and the QRad rain measurement in that particular WVC. The average rain excess backscatter ratio, η_{ex}, is used as an indicator to identify the level to which a given WVC is rain dominated, and expressed as:

$$\eta_{ex} = \sum_{i=1}^{N} \sigma_{ex,i}^{0}(r,p,\theta) \Big/ \sigma_{meas,i}^{0}(r,u,\chi,p,\theta) \tag{7.4}$$

The rain retrieval comparisons are conducted by examining the correlation coefficient of the SeaWinds / QRad retrievals against TMI rain rates, as a function of an "η_{ex} - based" threshold applied to the rain data. Figure 44 demonstrates that when no η_{ex} threshold is applied to the data, the calculated correlation coefficients of SeaWinds and QRad retrievals against TMI rain are somewhat comparable (~ 80%). However, as the applied threshold is increased, meaning that the rain data used in the comparison is increasingly dominated by rain, the combined passive / active SeaWinds rain retrievals affords an improved performance over the passive-only, QRad, rain measurements. Also, comparisons of the root mean square (RMS) error of SeaWinds / QRad retrievals (against TMI rain), show that an improvement of about 1.5 km*mm/hr (~ 20%) is achieved using the combined passive / active retrievals.

In the next section, we expand the validation activity of the combined SeaWinds retrievals through additional comparisons with standard TMI 2A12 rain product.

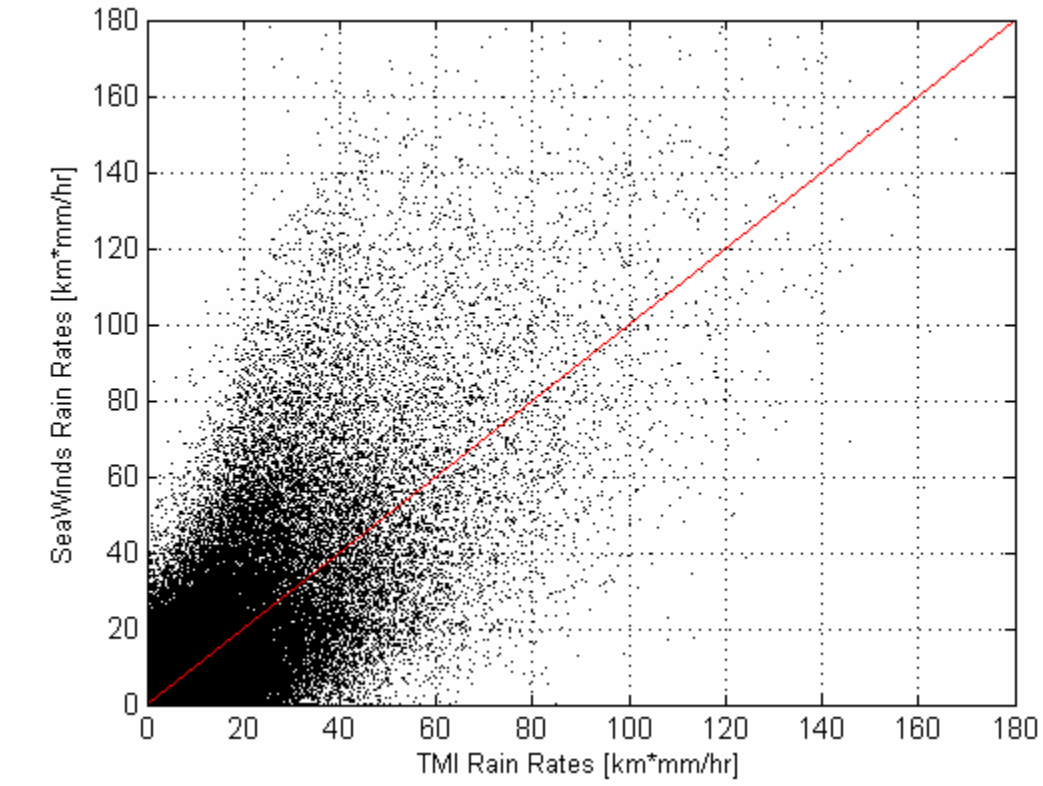

Figure 42: Instantaneous integrated rain rate comparisons for four hundred twenty one collocated rain events for SeaWinds and TMI. Spatial resolution is 0.25° (25 km).

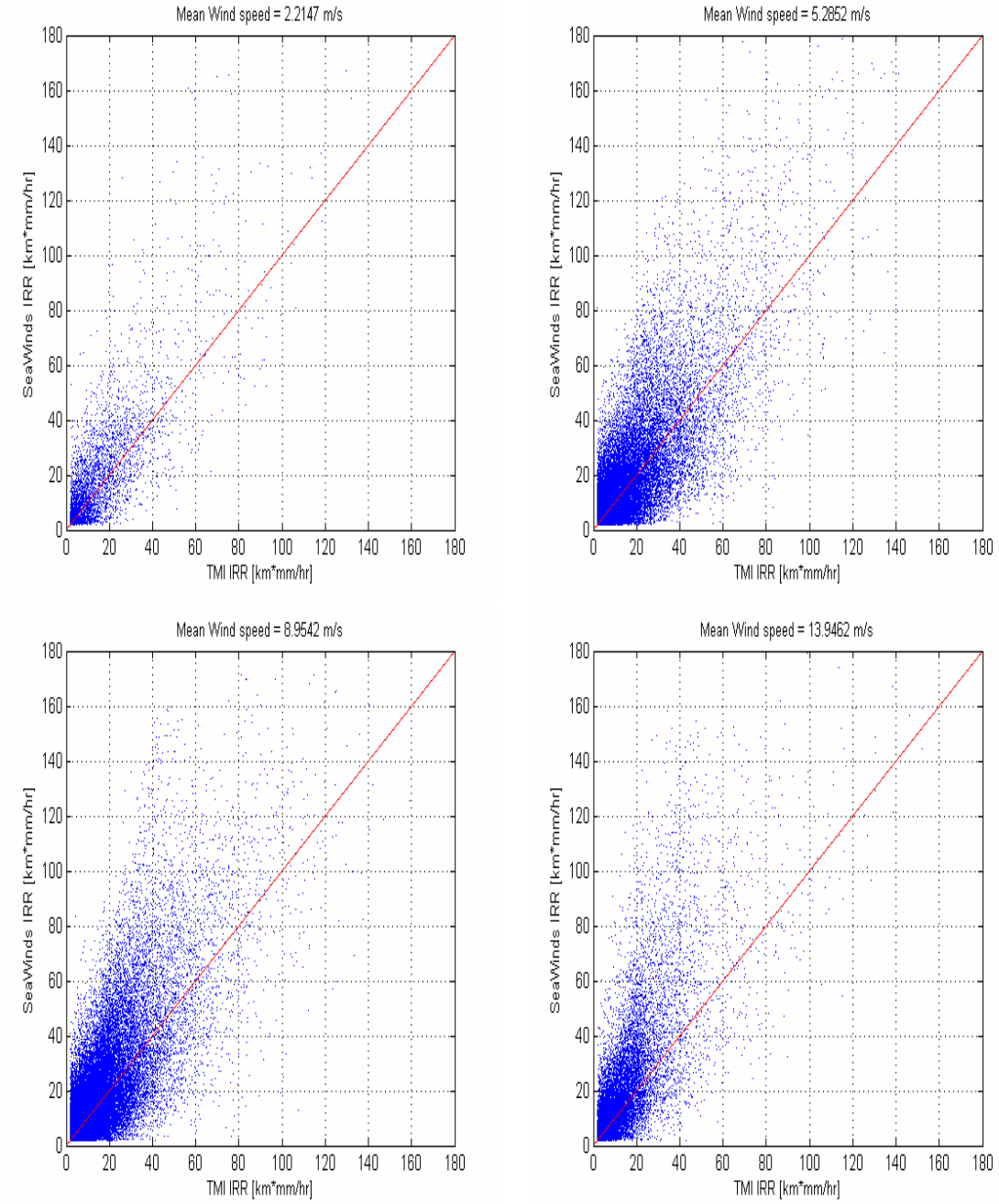

Figure 43: Instantaneous integrated rain rate comparisons for four hundred twenty one collocated rain events for SeaWinds and TMI over different wind speed regimes. Spatial resolution is 0.25° (25 km). For each regime, the average wind speed is shown on top.

Table 10: Instantaneous integrated rain rate (km*mm/hr) differences for six TMI ranges. For each range, the difference (SeaWinds minus TMI) is calculated.

TMI Range	Number of points	Difference mean	Difference std	Difference rms/<TMI>
0 – 4	112190	0.5622	2.6253	2.3789
4 – 8	28366	-0.4544	5.8533	1.0173
8 – 12	15798	-0.6628	8.4558	0.8608
12 – 24	24081	0.3938	13.8950	0.8169
24 – 32	7220	0.7318	20.7341	0.7514
> 32	11522	-1.0145	27.7985	0.5467

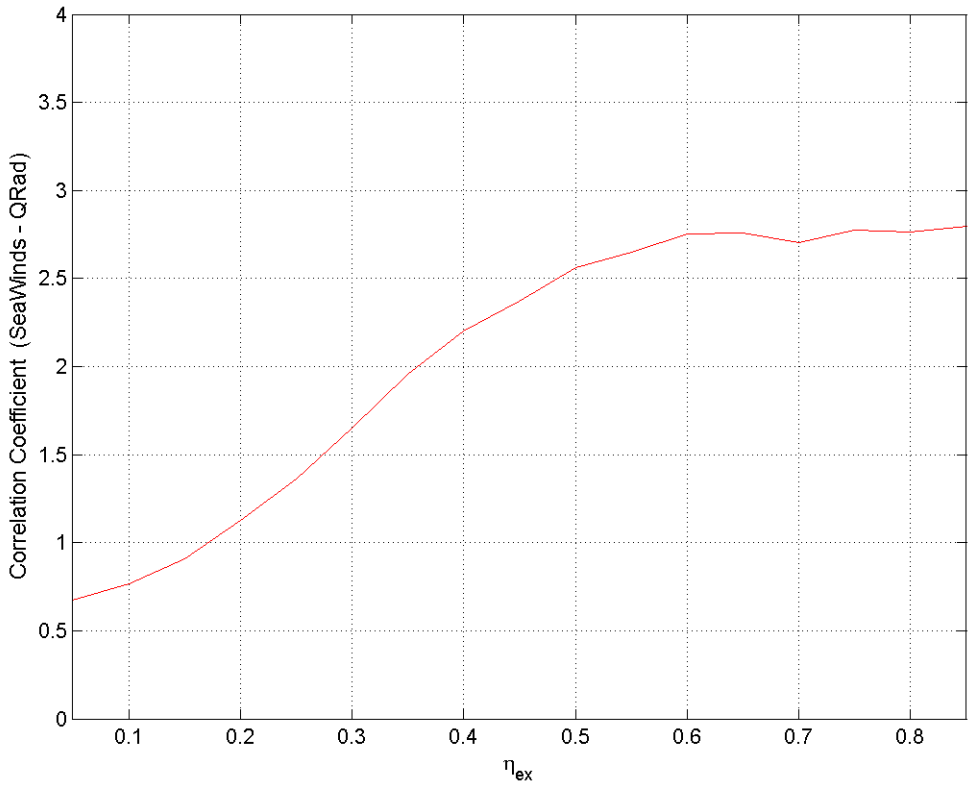

Figure 44: Improvement in correlation coefficients (SeaWinds minus QRad) vs. TMI as a function of rain excess backscatter ratio, η_{ex} .

Validation of SeaWinds Rain Retrievals

In order to further assess the performance of the combined passive / active SeaWinds oceanic rain retrieval algorithm, we perform quantitative near simultaneous comparisons with standard TRMM 2A12 rain product derived from the TMI sensor, which has a well established rain measurement accuracy [44]. The validation activity is based upon seventy two collocated rain events, near simultaneously observed by SeaWinds and TMI. This collocation dataset is independent from the one used in tuning the SeaWinds rain algorithm, and it spans a period of about seven months from April ~ October of the year 2003. To ensure temporal collocation, the worst case coincidence time difference for observing a particular rain event is restricted to be less than 30 minutes. Figure 45 depicts the geographic locations of the collocated rain events.

In order to compare SeaWinds and TMI rain rates, it is necessary to take into account the scales on which both sensors report their corresponding rain measurements. While SeaWinds report a single rain estimate for each 25 x 25 km WVC, the TMI sensor reports rain at a higher (finer) spatial resolution. Therefore, to create rain values with compatible spatial resolution to SeaWinds derived rain rates, the TMI rain measurements located inside a given WVC are spatially averaged and assigned to that particular WVC.

A scatter plot of TMI rain rates against the SeaWinds derived rain rates, for the seventy two collocated validation rain events, is shown in Figure 46. A comparison of the corresponding rain data probability density functions (pdf's) is presented in Figure 47. Although a slight distortion is observed at the low rain values, it can be readily seen that

the general shape of the pdf curves does match very well. The statistics of the rain error (SeaWinds – TMI), associated with the retrievals for three different wind speed regimes, are calculated and displayed graphically in Figure 48. As the figure illustrates, the rain error statistics of SeaWinds retrievals are almost unbiased, with close-to-zero mean values, regardless of the surface wind speed. These results demonstrate that the magnitude of the rain rates derived from SeaWinds correlate very well with TMI rain, further, the results verify that the wind correction procedure employed in the rain retrieval algorithm is well behaved in the mean.

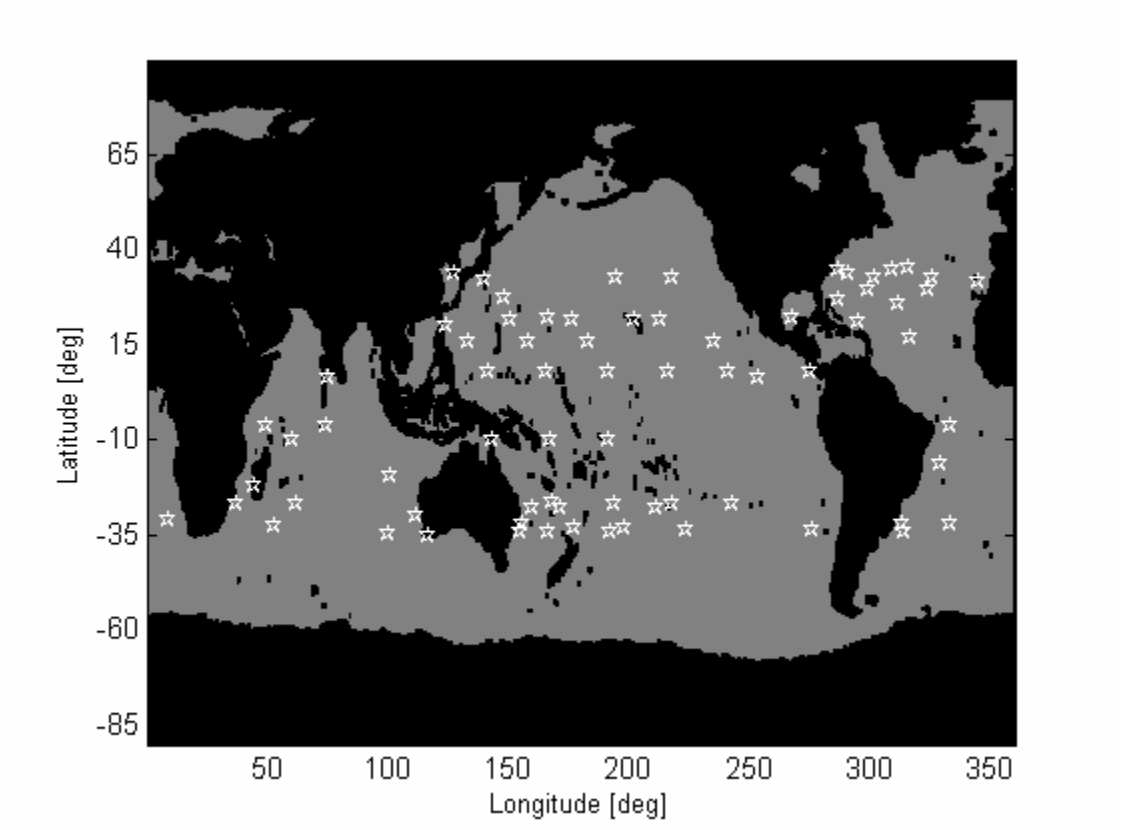

Figure 45: Locations of simultaneous collocated rain events for seventy two SeaWinds / TMI independent validation dataset. Collocation time difference is restricted to ±30 minutes.

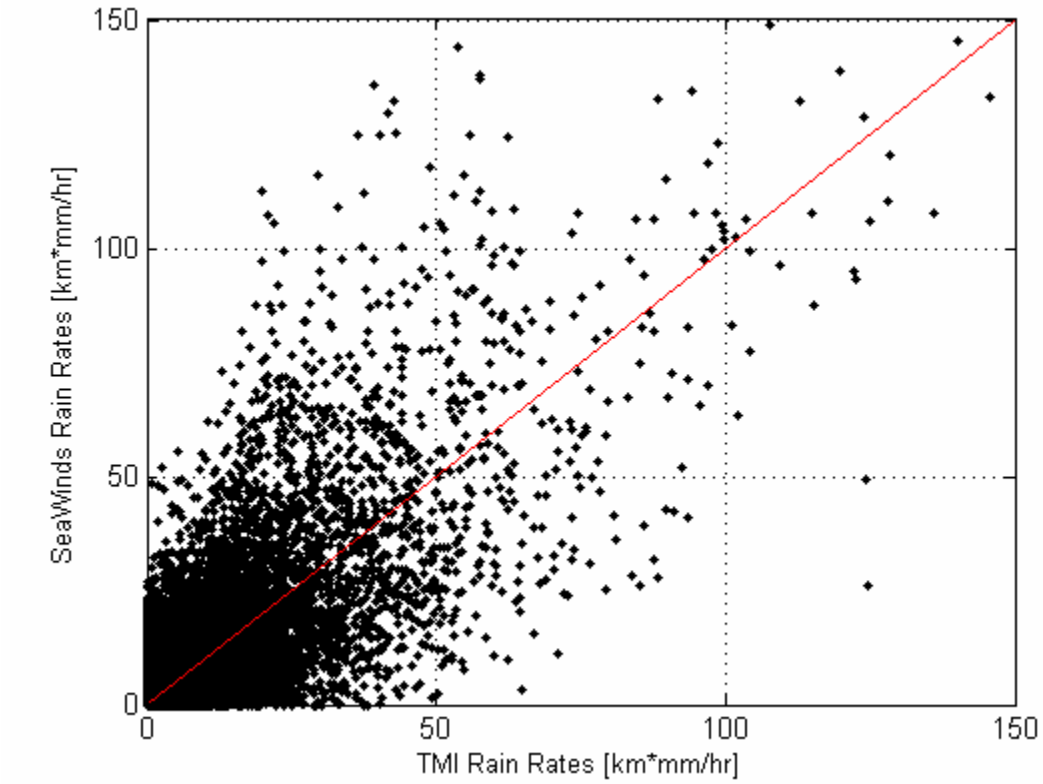

Figure 46: Instantaneous integrated rain rate comparisons for seventy two collocated rain events for SeaWinds and TMI. Spatial resolution is 0.25° (25 km).

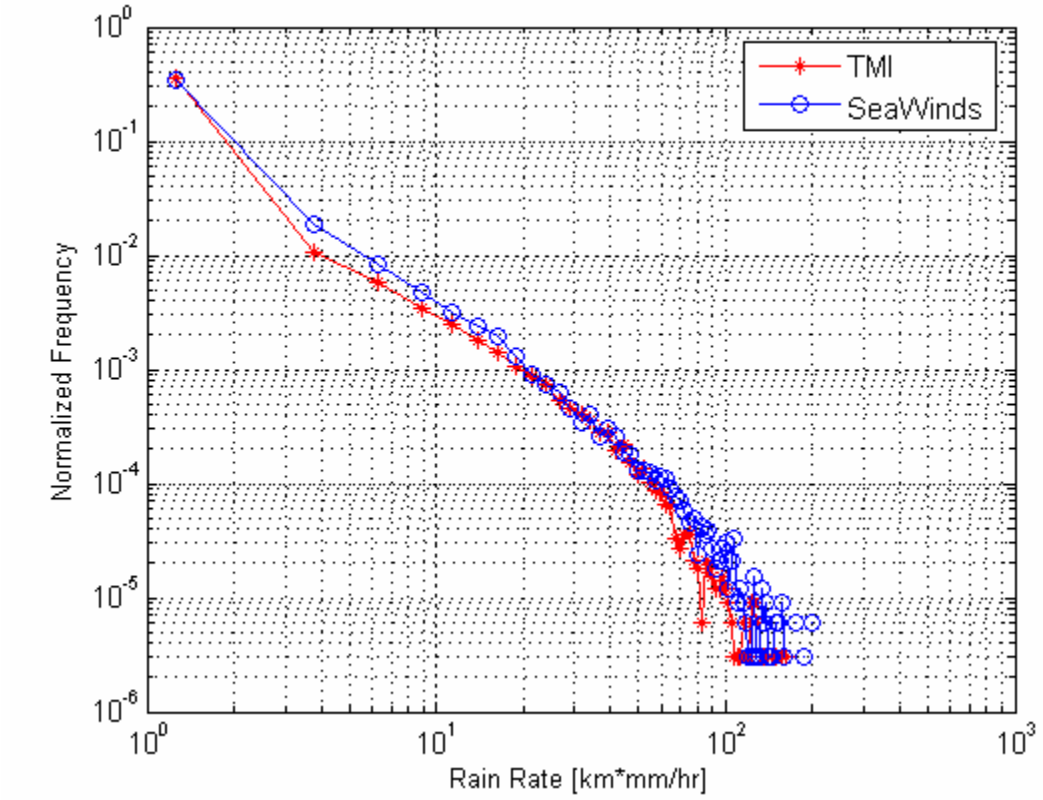

Figure 47: Rain rate probability density function for seventy two collocated validation rain events for SeaWinds and TMI.

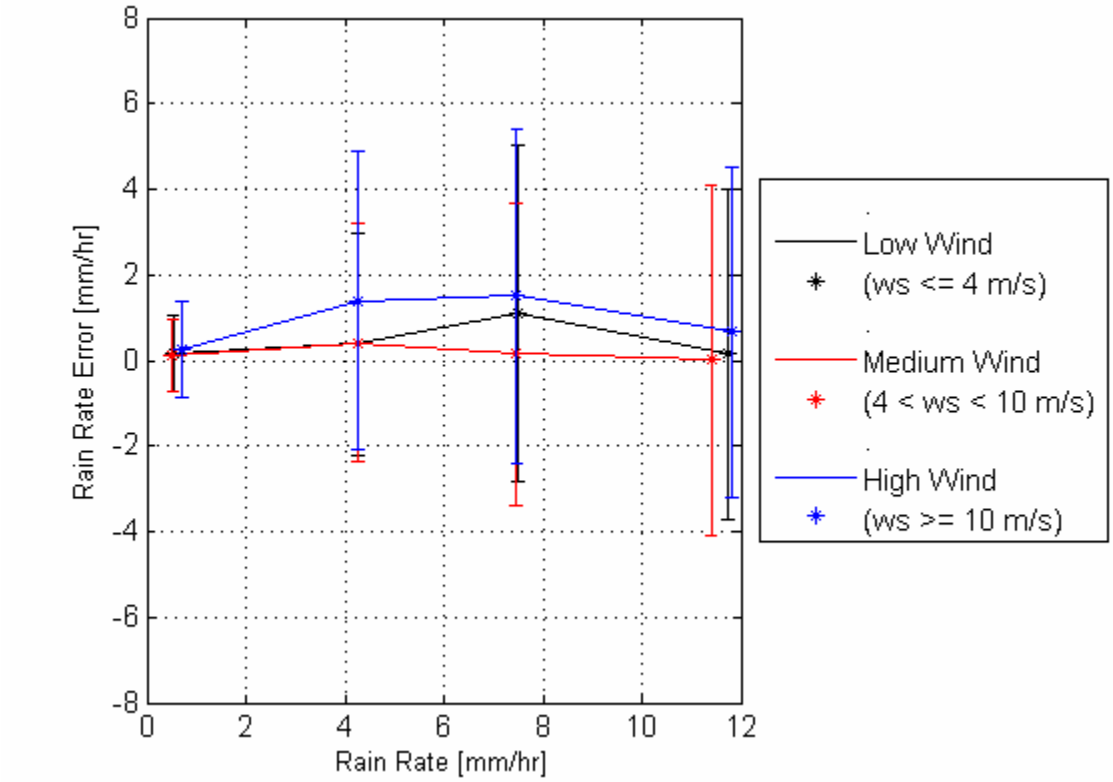

Figure 48: Rain rate error statistics (SeaWinds - TMI) as a function of rain rate for different wind speed regimes.

Next, we examine a typical near-instantaneously collocated SeaWinds / TMI rain event example, as shown in Figure 49. The rain event was observed on April 19 2003, within 15 minutes of the TRMM overpass. The top panel shows the TMI integrated rain rate, and the corresponding SeaWinds rain estimate is given in the lower panel. The pixel resolution is 25 km on a WVC measurement grid. Color scales are identical for both images and proportional to the integrated rain rates in [km*mm/hr]. To reduce the possible occurrence of spurious rainy pixels resulting from the noisy SeaWinds measurements, a threshold of 2 km*mm/hr is applied on both integrated rain values (equivalent to ~0.25 mm/hr). By comparing both rain retrievals given in Figure 49, it is evident that the shape and the relative intensity of the rain event are well captured by SeaWinds. For this particular event, the correlation coefficient is found to be 88%. The average correlation between TMI and SeaWinds rain estimates over the validation data set is 82%.

By applying the rain threshold on the retrieved rain rates, SeaWinds rain estimates can be utilized as a rain flag. An example is shown in the Figure 50. In order to quantify the performance of SeaWinds measurements as a stand alone flag for identifying the rain contaminated WVCs, we produce binary maps that are quantized into four levels to classify the rain pattern for the different collocated rain events. Using the TMI binary rain image as the surface truth, we classify the binary rain image pixels into three categories: the first is agreement percentage, which is the percentage of pixels that are simultaneously identified by both sensors (SeaWinds and TMI) as raining pixels or non raining pixels. The second category is the false alarm percentage, which is the percentage of pixels classified as raining pixels by SeaWinds, while identified as non raining pixels

by TMI. The third category defined as miss-rain percentage is the percentage of pixels classified as raining pixels by TMI, while the SeaWinds sensor identified those pixels as rain free.

The spatial rain pattern classification for the event under consideration is shown in the upper panel of Figure 50. Also, for comparision purposes, the lower panel of the figure presents the binary pattern classification calculated for the TMI vs. the JPL rain flag which is computed by the Impact based multidimensional histogram (IMUDH) algorithm [52]. This algorithm estimates the probability that a WVC is contaminated by rain based on various rain-dependent parameters. To ensure consistancy in our comparisions, we apply a small threshold value on IMUDH which results in flagging the same percentage of WVCs as the 2 km*mm/hr thresholded TMI. The different percentages of the rain pattern classification for the two cases are calculated and given in Table 11. We note that SeaWinds rain flag provides improved metrics compared to IMUDH based rain flag.

The evaluation of the SeaWinds rain flagging performance is extended by calculating the different SeaWinds-based rain pattern classification percentages (agreement, false alarm and miss-rain) against the TMI derived rain flag, for the seventy two collocated validation rain events, as a function of various surface wind speed regimes. The results, given in Table 12, demonstrate that SeaWinds rain flagging capability is nearly invariant regardless of the wind speed regime, with an average overall rain detection capability of about 90%.

Finally, we evaluate the rain detection capability of SeaWinds as a function of rain rate. Figure 51 illustrates that the SeaWinds rain retrieval algorithm can identify

more than 50 % of the WVCs with low rain rate values. However, as the observed rain rate increases and approcahes the vicinity of 2 mm/hr, the SeaWinds algorithm is capable of detecting more than 90% of the rain contaminated WVCs. This emphsize the powerful rain detection capability of SeaWinds rain algorithm, and the utility of SeaWinds based rain measurements as a stand-alone rain flag.

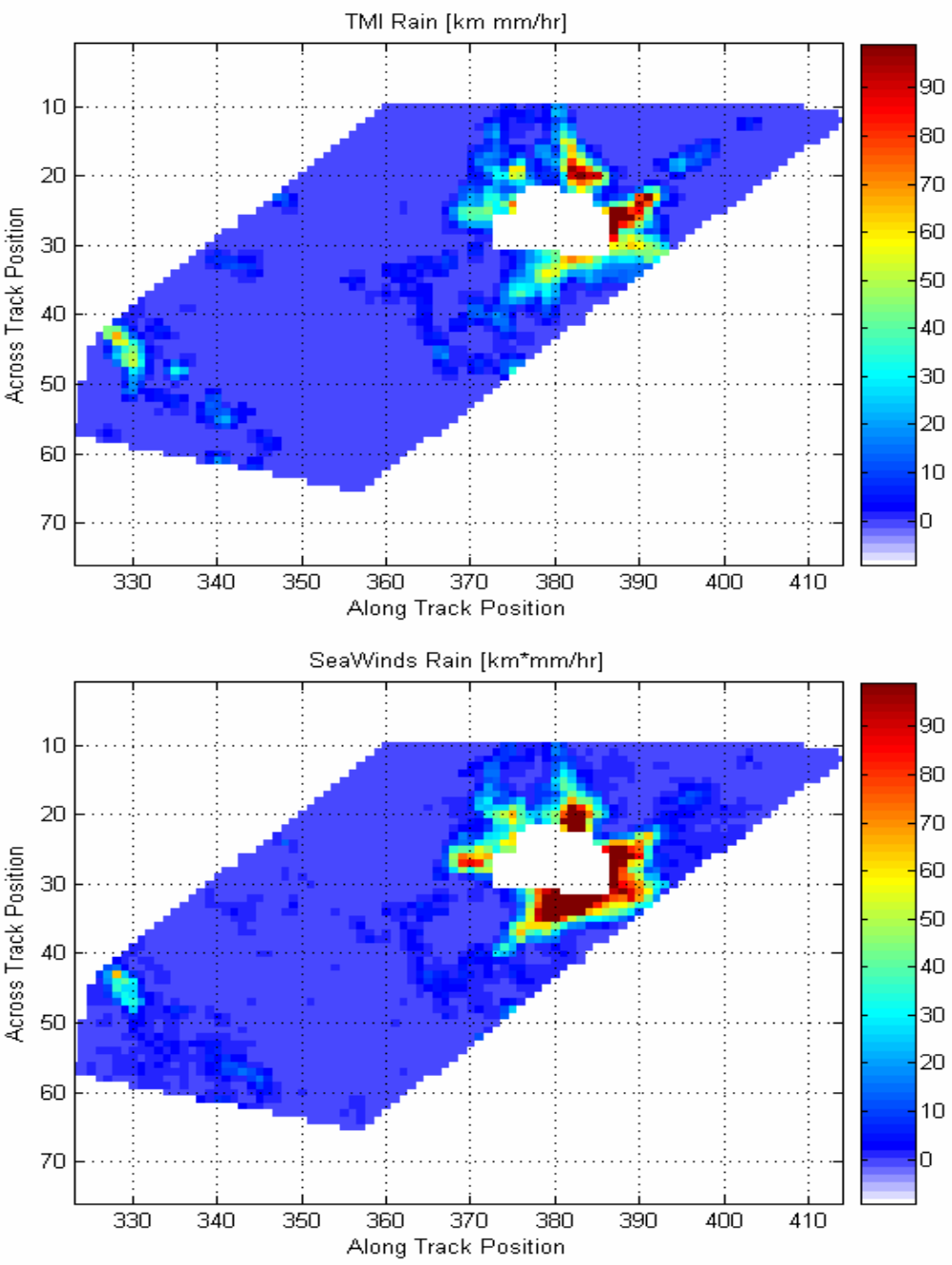

Figure 49: A typical example of rain event measured by TMI 2A12 product (top panel) and SeaWinds (lower panel). Spatial resolution is 25 km (WVC grid). Coincidence time difference ~ 15 minutes.

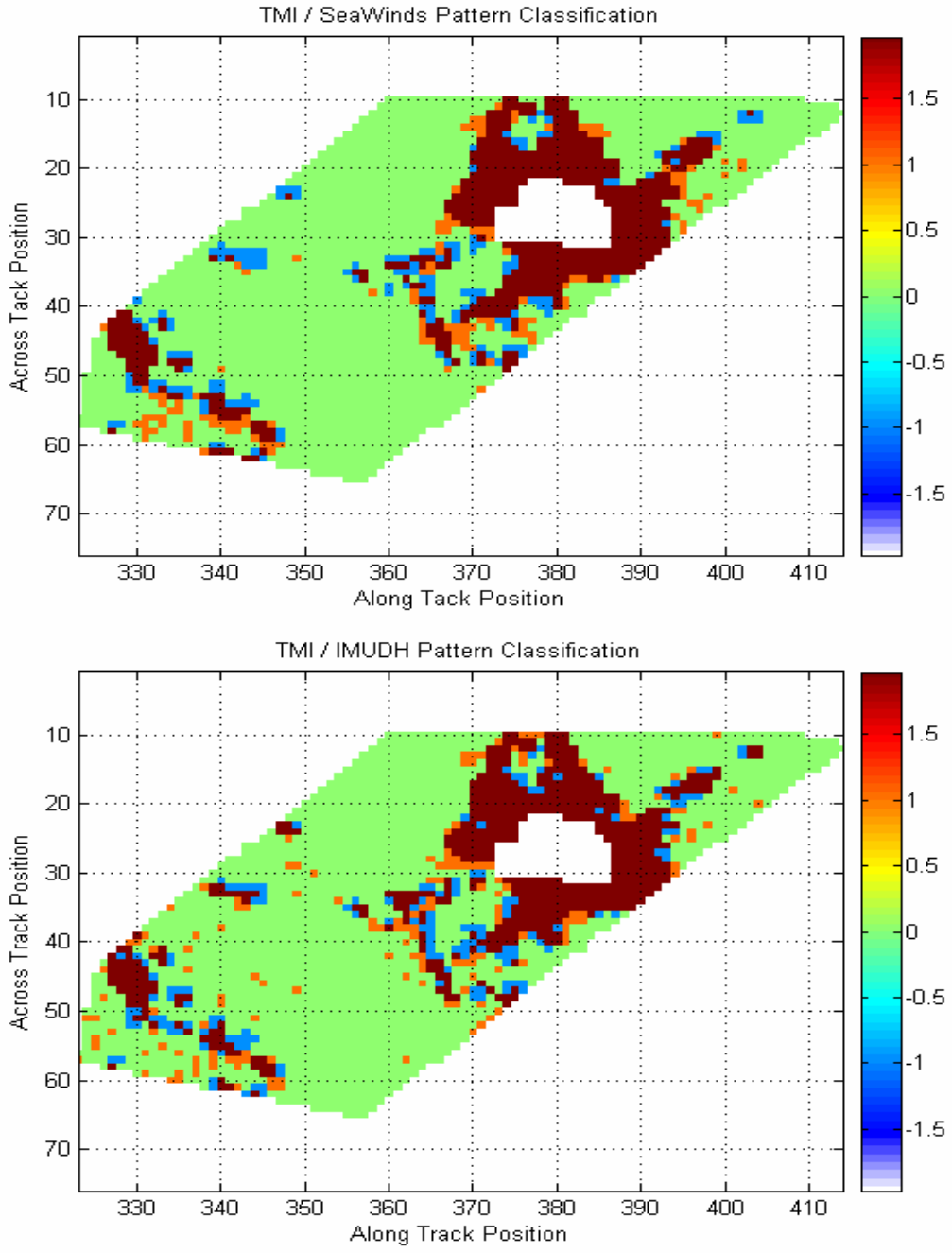

Figure 50: Pattern classification (WVC grid) between TMI vs. SeaWinds (top panel) and TMI vs. IMUDH (lower panel). Classification categories include: agreement (color indices 0 & 2), false alarm (color index 1) and miss rain (color index -1).

Table 11: Binary pattern classification results for rain event shown in Figure 50.

Comparison	Agreement %	False alarm %	Miss-rain %
SeaWinds / TMI	89.03	5.07	5.90
IMUDH / TMI	88.16	6.09	5.75

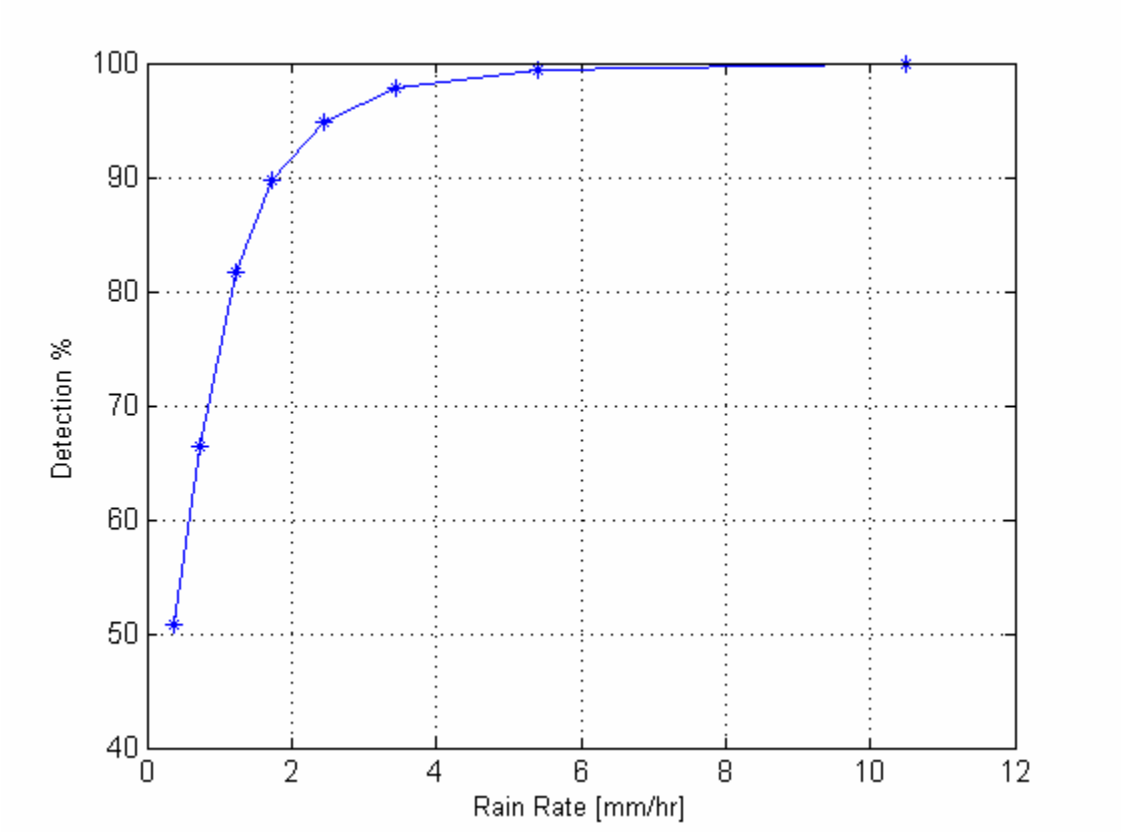

Figure 51: SeaWinds rain detection capability as a function of rain rate.

Table 12: SeaWinds rain pattern classification for various wind speed regimes.

Wind Speed Regime (m/s)	Agreement %	Missed Rain %	False Alarm %
$0 \le w_s < 3$	91.23	2.42	6.35
$3 \le w_s < 7$	90.43	3.44	6.13
$7 \le w_s < 12$	89.58	4.20	6.22
$w_s \ge 12$	85.67	8.33	6.00
All Data	89.78	4.05	6.17

Rain Retrieval Errors

There are several sources of error in the retrieved SeaWinds / QRad rain rates, which are the result of:

1. The random component of the passive QRad brightness temperature measurement error. Because of this larger than normal ΔT, the excess brightness temperature includes a large random, zero-mean, Gaussian noise component that distorts the retrieved rain rate, which is most obvious at low rain rates values. However, by averaging multiple pulses and employing spatial domain filtering techniques, the majority of this noise is canceled, and the effective radiometric sensitivity of the instrument is substantially improved, which results in a reasonable estimate of the true rain rate.

2. Convective and stratiform rain type differences. For the same rain rate, different rain types can produce differences in brightness temperatures / backscatter measurements, which are neglected in the T_{ex}-R / σ^0_{ex}-R relationships. To compensate for this effect, the SeaWinds / TMI training data set was selected over a wide range of geographic locations and seasons to produce an average relationship based upon the convective / stratiform conditions encountered.

3. Beam-fill differences between SeaWinds and TMI due to antenna spatial resolution. The SeaWinds scatterometer antenna was designed to optimize the antenna boresight gain at the expense of the antenna main beam efficiency. As a result, the antenna collects energy over an effective surface area that is approximately twice that of the TMI. To produce the T_{ex}-R / σ^0_{ex}-R relationships, the TMI rain rates were averaged to

match the SeaWinds measurement resolution; but the empirical beam filling corrections applied to TMI do not scale linearly. This will result in an increased variability of SeaWinds / QRad rain rates compared to the TMI measurements.

4. Long term systematic radiometric calibration drift. The QRad calibration stability illustrated in Figure 12 shows an rms variation of 1.4 K. This effect contributes to uncertainty in the empirically derived coefficients used in the retrieval algorithm and to biases in the average retrieved rain rates. Nevertheless, this error source is considered secondary to the error introduced by the large QRad ΔT.

5. Bias in NCEP / QuikSCAT wind speed data due to differing reference heights. Because in the presence of rain (and at low to moderate ocean wind speeds), wind retrievals from SeaWinds are bogus (typically 10 – 15 m/s independent of the true wind speed), we utilize wind data from numerical weather prediction NCEP to correct for the wind induced contribution to the passive and active measurements acquired by SeaWinds. However, it is known that the 1000 mbar NCEP winds are biased high compared to the 10 m neutral stability winds measured by SeaWinds. To compensate for this difference, a bias correction is applied to adjust the NCEP wind data to match SeaWinds derived winds under rain free conditions before use in the rain algorithm. This error source is not considered to be a significant source of rain retrieval error.

6. Inter-annual variability in the ocean (and atmosphere) background from climatology. Because of the low sensitivity of the 13.4 GHz brightness to the atmospheric and oceanic physical variables, this error source is not believed to be dominant. For example, qualitative comparisons with rain patterns from TMI (presented in chapter 5) do not show significant differences in the global rain images. This is

supported by good comparisons between the ocean background and the three-day brightness temperatures used in the QRad external T_B calibration.

7. Error in estimating the integrated rain rate. Because the TMI integrated rain rate value is not available, the IRR is approximated to be the product of the TMI surface rain rate (mm/hr) and the rain path length (km). Since both the surface rain rate from the TMI 2A12 product and the rain height from the TMI 3A11 product have random errors, this introduces increased error in the T_B-R / σ^0-R empirical relationships. However, the excess brightness temperature and the excess backscatter depend upon the integrated rain rate along the propagation path; and because the height of rain varies significantly over latitude, we believe that using this IRR is the best compromise. Further, the TMI training set is distributed over the full latitude range of TRMM, which provides an averaging effect. However, since the SeaWinds / QRad rain algorithms are also applied beyond the latitudinal range of TRMM, caution is advised because of the unknown accuracy in these regions.

CHAPTER EIGHT: SUMMARY AND CONCLUSIONS

The Ku-band satellite microwave remote sensor, SeaWinds, has the simultaneous capability to collect the active radar backscatter (σ^0), and the passive radiometric brightness temperature (T_B) measurements from the Earth's surface and intervening atmosphere. Although the instrument design was originally optimized solely to measure the speed and direction of the near surface oceanic wind vector, the polarized measurements acquired by SeaWinds are also highly sensitive to the presence of rainfall over the ocean. This dissertation expands the utility of the SeaWinds instrument by exploiting the rain sensitivity of the passive / active measurements to provide quantitative estimates of the global oceanic rainfall. The following discussion further illustrates the contributions made by this dissertation.

First, by building a large database of near-simultaneously tri-collocated measurements from SeaWinds, numerical weather prediction NCEP winds, and rain rate estimates produced by TMI microwave radiometer, we analyze the effect of oceanic rain on the polarized passive T_B measurements acquired by SeaWinds Radiomter (QRad). As presented in chapter 4, a simple brightness temperature model is developed to provide an estimate of the rain-induced T_B contribution (known as excess brightness, T_{ex}) to the total radiometric measured T_B, by correcting for the brightness contribution from surface wind speed, as well as, brightness contributions due to ocean surface (atmospheric) geophysical parameters. Because of the transient nature of the ocean surface wind, its brightness contribution is calculated instantaneously (for each satellite revolution) using

numerical NCEP wind fields along with an empirically derived first order brightness correction model. However, the relatively benign radiance, of the remaining ocean (atmosphere) geophysical parameters, justifies the estimation of their brightness contribution correction utilizing priori climatology information.

Using the estimated rain-induced T_{ex} brightness temperatures from QRad along with collocated TMI rain measurements, we empirically derive polarized (T_{ex} – R) transfer functions which are used in the framework of the statistical QRad rain inversion algorithm to infer the instantaneous oceanic rainfall. Validation studies, presented in chapter 5, demonstrate the fact that the passive-only QRad rain retrievals compare reasonably well with collocated rain observations obtained from independent microwave rain measuring instruments. Moreover, the validation studies do also illustrate the superior performance of microwave-based QRad measurements compared to rain rates derived from visible / infrared sources.

Second, by utilizing the same collocation database of SeaWinds / NCEP / TMI near-simultaneous measurements, in chapter 6, we characterize the effects of oceanic rain on the polarized active backscatter (σ^0) measurements collected by SeaWinds scatterometer. With the assumption that the rain effects on measured backscatter are isotropic, a simple first order model for the SeaWinds polarized backscatter signal is developed as a function of the polarized wind induced surface backscatter, and the integrated rain rate. The simple empirical model incorporates the effects of the scatterometer two-way signal attenuation, and the additional excess backscatter (σ^0_{ex}) due to the presence of oceanic rain. The empirical model is validated using actual polarized backscatter measurements from SeaWinds. Results demonstrate the capability of the

model to accurately reproduce the effects of rain on the polarized active backscatter measurements collected by SeaWinds twin beams.

Third, by further exploiting the sensitivity of SeaWinds active backscatter σ^0 measurements to the presence of rain, we develop a combined passive / active mathematical rain retrieval algorithm for SeaWinds. The SeaWinds rain algorithm, presented in chapter 7, utilizes the passive-only QRad rain measurements, the active σ^0 measurements, the NCEP wind fields, in conjunction with the empirically derived rain-induced excess backscatter, and attenuation models to refine the passive-only rain estimation performance. An objective function mathematical model is formulated and minimized to provide global quantitative estimates of the oceanic rainfall.

At the Ku-band (13.4 GHz) operating frequency of SeaWinds sensor, the contributions of the observed rain / wind combinations to both: the passive radiometric T_B and active backscatter σ^0 measurements acquired by the instrument polarized twin beams, are generally non-orthogonal. While the passive T_B measurements are mainly rain dominated under most rain / wind conditions; the collected active backscatter σ^0 is highly dependent on the wind / rain combination, and can be either wind or rain dominant.

Compared to the passive-only QRad rain retrievals, combining the passive and active measurements acquired by SeaWinds in the rain estimation process affords an improved performance, especially over rain dominated regions. The improvement is manifested as an increase in the correlation coefficient, and a decrease in the rms error against the “surface truth” rain rates derived from TMI. However, the improvement in performance is achieved at the expense of a higher computational cost.

By applying a threshold on the retrieved SeaWinds / QRad rain rates, the rain information can be converted to a "stand-alone" rain-flag to identify erroneous rain-contaminated oceanic wind vector retrievals. The performance of SeaWinds rain-flag algorithm is validated through comparisons with JPL IMUDH and TMI-based rain flags. Results demonstrate the robustness and the excellent detection capability of the SeaWinds-based rain-flag, regardless of the underlying wind speed regime.

The major scientific utility of SeaWinds / QRad rain measurements is that they provide additional independent temporal and spatial sampling of the oceanic rain, which complements the coverage provided by TMI and the SSMIs' instruments. Thus, the SeaWinds / QRad rain time series from 1999 to present is a valuable addition to the oceanic precipitation climatology dataset that can be potentially used to improve the diurnal estimation of the global rainfall, which is a goal for NASA's next generation, satellite-based, Global Precipitation Measurement (GPM) mission program. Moreover, the early availability of SeaWinds-based rain data will afford users early access to learn to use less-precise rain measurements that will occur in the future with the use of less-capable constellation satellites. The rainfall retrieval algorithm has been implemented by NASA Jet Propulsion Laboratory (JPL) as part of level 2B (L2B) science data product, which can be obtained from the Physical Oceanography Distributed Data Archive (PO.DAAC), Pasadena, CA.

LIST OF REFERENCES

[1] W. L. Grantham, E. M. Bracalente, W. L. Jones, and J. W. Johnson, "The SeaSat-A satellite scatterometer," *IEEE J. Oceanic Eng.*, vol. OE-2, pp. 200-206, 1977.

[2] F. T. Ulaby, R. K. Moore, and A. K. Fung, *Microwave Remote Sensing Active and Passive, Vol 2, Radar Remote Sensing and Surface Scattering and Emission Theory*, vol. 2: Artech House, 1982.

[3] F. T. Ulaby, R. K. Moore, and A. K. Fung, *Microwave Remote Sensing Active and Passive, Vol 3, From Theory to Applications*, vol. 3: Artech House, 1986.

[4] M. A. Goodberlet, C. T. Swift, and J. C. Wilkerson, "Ocean surface wind speed measurements of the Special Sensor Microwave/Imager (SSM/I)," *IEEE Trans. Geosci. Remote Sensing*, vol. 28, pp. 823-828, 1990.

[5] F. T. Ulaby, R. K. Moore, and A. K. Fung, *Microwave Remote Sensing Active and Passive, Vol. 1, Microwave Remote Sensing Fundamentals and Radiometry*, vol. 1: Artech House, 1981.

[6] W. L. Jones, R. Mehershahi, and J. Zec, "SeaWinds on QuikSCAT Radiometric Measurements and Calibration," presented at IEEE Int. Geosci. Remote Sens. Symp, Honolulu, Hawaii, 2000.

[7] A. Bentamy, E. Autret, P. Queffeulou, and Y. Quilfen, "Intercomparison of ERS-2 and QuikSCAT winds," presented at IEEE International Geoscience and Remote Sensing Symposium, Honolulu, HI 2000.

[8] M. I. Skolnik, *Introduction to Radar Systems.* New York: McGraw-Hill, 2001.

[9] S. M. Alhumaidi, "Development of a geophysical model function for a radar scatterometer using neural networks." Melbourne, FL: Florida Institute of Technology, 1997.

[10] S. J. Shaffer, R. S. Dunbar, S. V. Hsiao, and D. G. Long, "A median filter based ambiguity removal algorithm for NSCAT," *IEEE Trans. Geosci. Rem. Sens*, vol. 29, pp. 167-174, 1991.

[11] R. K. Moore and W. L. Jones, "Satellite scatterometer wind vector measurement – the legacy of the Seasat satellite scatterometer," *IEEE Geosci. Remote Sens. Newsletter*, pp. 18-32, 2004.

[12] E. P. W. Attema, "The Active Microwave Instrument On-Board the ERS-1 Satellite," *IEEE Trans. Geosci. Remote Sens.*, vol. 79, pp. 791-799, 1991.

[13] E. P. W. Attema and P. Lecomte, "The ERS-1 and ERS-2 wind scatterometers, system performance and data products," Seattle, WA.

[14] C. H. Chen, *Frontiers of remote sensing information processing*: World Scientific, 2003.

[15] J. P. HOLLINGER, J. L. PEIRCE, and G. A. POE, "SSM/I Instrument Evaluation," *IEEE Trans. Geosci. Rem. Sens*, vol. 28, pp. 781-790, 1990.

[16] C. Kummerow, W. Barnes, T. Kozu, J. Shiue, and J. Simpson, "The tropical rainfall measuring mission (TRMM) sensor package," *J. Atmos. Ocean. Technol.*, vol. 15, pp. 809–817, 1998.

[17] F. J. Wentz, P. Ashcroft, and C. Gentemann, "Post-Launch Calibration of the TRMM Microwave Imager," *IEEE Trans. Geosci. Rem. Sens*, vol. 39, pp. 415-422, 2001.

[18] K. Imaoka, T. Sezai, T. Takeshima, T. Kawanishi, and A. Shibata, "Instrument characteristics and calibration of AMSR and AMSR-E," presented at IEEE Geoscience and Remote Sensing Symposium, 2002. IGARSS '02. , 2002.

[19] P. W. Gaiser, K. M. S. Germain, E. M. Twarog, G. A. Poe, W. Purdy, D. Richardson, W. Grossman, W. L. Jones, D. Spencer, G. Golba, J. Cleveland, L. Choy, R. M. Bevilacqua, and P. S. Chang, "The WindSat Spaceborne Polarimetric Microwave Radiometer: Sensor Description and Early Orbit Performance," *IEEE Trans. Geosci. Rem. Sens*, vol. 42, pp. 2347-2361, 2004.

[20] M. W. Spencer, C. Wu, and D. G. Long, "Tradeoffs in the design of a spaceborne scanning pencil beam scatterometer: Application to SeaWinds," *IEEE Trans. Geosci. Remote Sens.*, vol. 35, pp. 115-126, 1997.

[21] R. J. Mehershahi, "Ocean Tb Measurements Using the QuikSCAT Radiometer," in *Electrical and Computer Engineering*. Orlando, FL: Univ. of Central Florida, 2000.

[22] M. M. Wisler and J. P. Hollinger, "Estimation of Marine Environmental Parameters using Microwave Radiometric Remote Sensing Systems," Naval Research Laboratory, Wash DC. NRL Memo Rpt 3661, 1977.

[23] W. S. Olson, "Physical retrieval of rainfall rates over the ocean by multispectral radiometry: Application to tropical cyclones," *J. Geophys. Res.*, vol. 94, pp. 2267-2280, 1989.

[24] T. T. Wilheit, A. T. C. Chang, M. S. V. Rao, E. B. Rodgers, and J. S. Theon, "A satellite technique for quantitatively mapping rainfall rates over the ocean," *J. Appl. Meteorol.*, vol. 16, pp. 551-560, 1977.

[25] T. T. Wilheit, A. T. C. Chang, and L. S. Chiu, "Retrieval of Monthly Rainfall Indices from Microwave Radiometric Measurements Using Probability Distribution Functions," *J. Atmos. Oceanic Technol.*, vol. 8, pp. 118–136, 1991.

[26] C. Kidd and E. C. Barrett, "The use of passive microwave imagery in rainfall monitoring," *Remote Sensing Rev*, vol. 4, pp. 415-450, 1990.

[27] P. Bauer and P. Schlnessel, "Rainfall, total water, ice water and water vapor over the sea from polarized microwave simulations and SSM/I data," *J. Geophys. Res.*, vol. 98, pp. 20737-20759, 1993.

[28] C. Kummerow, W. S. Olson, and L. Giglio, "A Simplified Scheme for Obtaining Precipitation and Vertical Hydrometeor Profiles from Passive Microwave Sensors," *IEEE Trans. Geosci. Remote Sens.*, vol. 34, pp. 1213-1232, 1996.

[29] M. H. Freilich and R. S. Dunbar, "Derivation of satellite wind model functions using operational surface wind analyses - an altimeter example," *J. Geophys. Res.*, vol. 98, pp. 14,633–14,649, 1993.

[30] D. W. Draper and D. G. Long, "Evaluating the effect of rain on SeaWinds scatterometer measurements," *Journal of Geophysical Research*, vol. 109, 2004.

[31] B. W. Stiles and S. H. Yueh, "Impact of Rain on Spaceborne Ku-Band Wind Scatteromter Data," *IEEE Transactions on Geoscience and Remote Sensing*, vol. 40, pp. 1973-1983, 2002.

[32] R. K. Moore, A. H. Chaudry, and I. J. Birrer, "Errors in scatterometer-radiometer wind measurement due to rain," *IEEE J. Ocean. Eng.*, vol. OE-8, pp. 37- 49, 1983.

[33] D. E. Weissman, M. A. Bourassa, J. J. O'Brien, and J. Tongue, "Calibrating the QuikSCAT/SeaWinds radar for measuring rainrate over the oceans," *IEEE Trans. Geosci. Rem. Sens*, pp. 2814-2820, 2003.

[34] G. W. Petty and K. B. Katsaros, "Nimbus-7 SMMR Precipitation Observations Calibrated against Surface Radar during TAMEX," *J. Appl. Meteorol.*, vol. 31, pp. 489–505, 1992.

[35] T. L. Bell and N. Reid, "Detecting the Diurnal Cycle of Rainfall Using Satellite Observations," *J. Appl. Meteorol.*, vol. 32, pp. 311–322, 1993.

[36] A. T. C. Chang, L. S. Chiu, and G. Yang, "Diurnal Cycle of Oceanic Precipitation from SSM/I Data," *Monthly Weather Review*, vol. 123, pp. 3371-3380, 1995.

[37] K. Imaoka and R. W. Spencer, "Diurnal Variation of Precipitation over the Tropical Oceans Observed by TRMM/TMI Combined with SSM/I," *Journal of Climate*, vol. 13, pp. 4149–4158, 2000.

[38] E. Smith and e. al, "Optimizing Orbit-Instrument Configuration for Global Precipitation Mission (GPM) Satellite Fleet," presented at IEEE Int. Geosci. Remote Sens. Symp, Sydney, Australia, 2001.

[39] E. A. Smith, "Current Development of Global Precipitation Mission (GPM)," presented at 7th International Conference on Precipitation, Rockport, Maine, 2001.

[40] K. A. Ahmad, W. L. Jones, T. Kasparis, S. W. Vergara, I. S. Adams, and J. D. Park, "Oceanic Rain Rate Estimates from the QuikSCAT Radiometer: A Global Precipitation Mission pathfinder," *J. Geophys. Res.*, vol. 110, 2005.

[41] F. J. Wentz and R. W. Spencer, "SSM/I Rain Retrievals within a Unified All-Weather Ocean Algorithm," *J. of Atmos. Sci.*, vol. 55, 1998.

[42] C. Mears, D. Smith, and e. al., "QuikSCAT brightness temperatures and their Impact on rain flagging," Remote Sensing Systems, Santa Rosa, Calif 031300, 2000.

[43] "QuikSCAT Science data product user's manual," Jet Propulsion Laboratory, Pasadena, Calif 2001.

[44] C. Kummerow, J. Simpson, O. Thiele, W. Barnes, A. T. C. Chang, E. Stocker, R. F. Adler, A. Hou, R. Kakar, F. Wentz, P. Ashcroft, T. Kozu, Y. Hong, K. Okamoto, T. Iguchi, H. Kuroiwa, E. Im, Z. Haddad, G. Huffman, B. Ferrier, W. S. Olson, E. Zipser, E. A. Smith, T. T. Wilheit, G. North, T. Krishnamurti, and K. Nakamura, "The Status of the Tropical Rainfall Measuring Mission (TRMM) after Two Years in Orbit," *J. Appl. Meteorol.*, vol. 39, pp. 1965–1982, 2000.

[45] G. J. Huffman, R. F. Adler, E. F. Stocker, D. T. Bolvin, and E. J. Nelkin, "Analysis of TRMM 3-hourly multi-satellite precipitation estimates computed in both real and post-real time," presented at 12th Conf. on Satellite Meteorology and Oceanology, Long Beach, Calif., 2003.

[46] W. S. Olson, C. D. Kummerow, Y. Hong, and W. K. Tao, "Atmospheric latent heating distributions in the tropics derived from satellite passive microwave radiometer measurements," *J. Appl. Meteor.*, vol. 38, pp. 633-664, 1999.

[47] L. F. Bliven, J. P. Giovanangeli, and G. Norcross, "Scatterometer Directional Response During Rain," in *IEEE International Geosicence and and Remote Sensing Symposium*. Vancouver, B.C., Cananda: IEEE, 1989

[48] R. F. Contreras and W. J. Plant, "Modeling rain effects on microwave backscatter from the ocean," in *Oceans 2003*: IEEE, 2003

[49] R. F. Contreras and W. J. Plant, "The Surface Effect of Rain on Microwave Backscatter from the Ocean," in *International Geoscience and Remote Sensing Symposium, IGARSS '06* IEEE, 2006.

[50] D. E. Weissman, M. A. Bourassa, and J. Tongue, "Effects of rain rate and wind magnitude on SeaWinds scatterometer wind speed errors " *J. Atmos Ocean. Technol.*, vol. 19, pp. 738-746, 2002.

[51] K. A. Ahmad, W. L. Jones, and T. Kasparis, "Oceanic Rainfall Retrievals using passive and active measurements from SeaWinds Remote Sensor," presented at IGARSS 07, Barcelona, Spain, 2007.

[52] "JPL Physical Oceanography Distributed Active Archive Center (PO.DAAC)."

[53] Y. Wang, "A Statistical Algorithm for Inferring Rain Rate from the QuikSCAT Radiometer," in *Electrical and Computer Engineering*. Orlando, FL: Univ. of Central Florida, 2001.